

ADVANCED GEOPHYSICAL ENVIRONMENT ANALYSIS AND SIMULATION TECHNIQUES

S. M. Ayer
J. N. Bass
N. A. Bonito
R. G. Caton
C. U. Cook
J. M. Griffin

C. A. Hein
M. J. Kendra
G. Law
A. G. Ling
A. R. Long
W. J. McNeil

N. I. Miller
C. J. Roth
G. P. Seeley
L. E. Sexton
M. F. Tautz
R. P. Vancour

Radex, Inc.
Three Preston Court
Bedford, MA 01730

August 17, 1998

Final Report
May 1995 to June 1998

Approved for public release; distribution unlimited

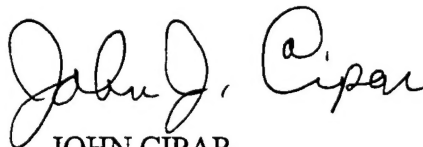
20000821 060



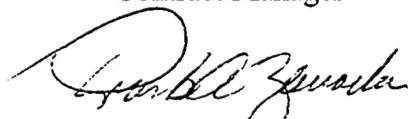
**AIR FORCE RESEARCH LABORATORY
Space Vehicles Directorate
29 Randolph Road
AIR FORCE MATERIEL COMMAND
HANSCOM AIR FORCE BASE, MA 01731-3010**

RECEIVED

This Technical Report has been reviewed and is approved for publication"



JOHN CIPAR
Contract Manager



LT COL FRANK ZAWADA
Branch Chief

This report has been reviewed by the ESC Public Affairs Office (PA) and is releasable to the National Technical Information Service (NTIS).

Qualified requestors may obtain additional copies from the Defense Technical Information Center (DTIC). All others should apply to the National Technical Information Service (NTIS).

If your address has changed, if you wish to be removed from the mailing list, or if the address is no longer employed by your organization, please notify AFRL/VSOS-IMA, 29 Randolph Road, Hanscom AFB, MA 01731-3010. This will assist us in maintaining a current mailing list.

Do not return copies of this report unless contractual obligations or notices on a specific document require that it be returned.

REPORT DOCUMENTATION PAGE			Form Approved OMB No. 0704-0188	
Public reporting burden for this collection of information is estimated to average 1 hour per response, including the time for reviewing instructions, searching existing data sources, gathering and maintaining the data needed, and completing and reviewing the collection of information. Send comments regarding this burden estimate or any other aspect of this collection of information, including suggestions for reducing this burden, to Washington Headquarters Services, Directorate for Information Operations and Reports, 1215 Jefferson Davis Highway, Suite 1204, Arlington, VA 22202-4302, and to the Office of Management and Budget, Paperwork Reduction Project (0704-0188), Washington, DC 20503.				
1. AGENCY USE ONLY (Leave Blank)	2. REPORT DATE August 17, 1998	3. REPORT TYPE AND DATES COVERED Final Report (May 1995 to June 1998)		
4. TITLE AND SUBTITLE Advanced Geophysical Environment Analysis and Simulation Techniques		5. FUNDING NUMBERS F19628-95-C-0106		
6. AUTHORS S. M. Ayer, J. N. Bass, N. A. Bonito, R. G. Caton, C. U. Cook, J. M. Griffin, C. A. Hein, M. J. Kendra, G. Law, A. G. Ling, A. R. Long, W. J. McNeil, N. I. Miller, C. J. Roth, G. P. Seeley, L. E. Sexton, M. F. Tautz, R. P. Vancour		PR 7659 TA GY WU AG		
7. PERFORMING ORGANIZATION NAME(S) AND ADDRESS(ES) Radex, Inc. Three Preston Court Bedford, MA 01730		8. PERFORMING ORGANIZATION REPORT NUMBER RXR-980801		
9. SPONSORING / MONITORING AGENCY NAME(S) AND ADDRESS(ES) Air Force Research Laboratory 29 Randolph Road Hanscom AFB, MA 01731-3010 Contract Manager: John J. Cipar/VSSW		10. SPONSORING / MONITORING AGENCY REPORT NUMBER AFRL-VS-HA-TR-0083		
11. SUPPLEMENTARY NOTES				
12a. DISTRIBUTION / AVAILABILITY STATEMENT Approved for Public Release Distribution Unlimited		12b. DISTRIBUTION CODE		
13. ABSTRACT (Maximum 200 words) This contract supported investigations to analyze geophysical and atmosphere measurements and to develop software systems for the following: analysis of DMSP data for the SSM and SSIES experiments; the GEOSpace code for 3D visualization of the dynamic space environment; the IRTSS software, to support multiple users over the WWW; the CSSM, which renders clouds realistically in near real-time; SCINDA, to provide near real-time warning of communication outages; modeling of the atmospheric effects of meteors and the metals they leave behind; IONCAP, to modify for increased accuracy of area coverage analysis; the SPREE and CHAWS programs for data analysis; and DIDM software, for a web-based data analysis process that is fast and responsive to the user.				
14. SUBJECT TERMS DMSP, SSM, SSIES, Ionosphere, Atmosphere, Magnetosphere, APGA, Electric and magnetic fields, GEOSpace, PRISM, IRTSS, CSSM, Visualization, Scintillation, SCINDA, Ablation, Meteors, Mesospheric metals, IONCAP, SPREE, CHAWS, CHAPS, CHUNKS, DIDM, STEP			15. NUMBER OF PAGES	
			16. PRICE CODE	
17. SECURITY CLASSIFICATION OF REPORT Unclassified	18. SECURITY CLASSIFICATION OF THIS PAGE Unclassified	19. SECURITY CLASSIFICATION OF ABSTRACT Unclassified	20. LIMITATION OF ABSTRACT Unlimited	

TABLE OF CONTENTS

<u>Section</u>	<u>Page</u>
1. DEFENSE METEOROLOGICAL SATELLITE PROGRAM	1
1.1 SPECIAL SENSOR MAGNETOMETERS (SSM)	1
1.1.1 Objectives of the SSM	2
1.1.2 Scientific and Operational Purposes	3
1.1.2.1 Operational Satellites	3
1.1.2.2 In-Flight Calibration and Re-Calibration	3
1.1.2.3 F14 In-Flight Calibration	4
1.1.3 APHB Documentation	4
2. SSIES-3	6
2.1 SSIES-3 SENSOR UPGRADES	8
2.2 INTEGRATION OF THE SIMPLEX LEAST-SQUARES ALGORITHM INTO PROGRAM APGA, FOR SSIES-2	9
2.3 DESCRIPTION OF SOFTWARE	11
2.3.1 SSIES Analysis Program APGA	11
2.3.2 AFRL Analysis Routine RPA	12
2.3.3 Integration of the Simplex Code into Program APGA	13
2.3.4 Definition of an APGA Benchmark	13
2.3.5 APGA-RPA Interface	16
2.3.5.1 APGA-RPAPRC Interface	16
2.3.5.2 Subroutine RPAPRC Logic	16
2.3.5.3 Interface Between Subroutines RPAPRC and RPA ...	17
2.3.6 Other Changes to Subroutine RPA and its Descendants	19
2.4 INSTALLATION, MAINTENANCE, AND OPERATION	20
2.4.1 Installation	20
2.4.2 Maintenance	21
2.4.3 Operation	21
2.5 TESTS	22
2.6 PROGRAM APGA MODIFICATIONS FOR SSIES-3 (APGA VERSION 3)	27
2.6.1 RPA and PP	27
2.6.1.1 Reading and Interpreting the Raw Data	27
2.6.1.2 Acquiring the RPA Sweeps	28
2.6.1.3 Acquiring the PP Sweeps	29
2.6.1.4 Analysis	30
2.6.1.5 RPA Sweeps	30
2.6.1.6 PP Sweeps	30

Table of Contents (Cont'd)

<u>Section</u>	<u>Page</u>
2.6.2 Implementation in APGA Version 3	32
2.6.3 Drift Meter	33
2.6.3.1 New Handling of Offset Due to Electrometer Imbalance	34
2.6.3.2 Modified Scheduling Of Horizontal and Vertical Measurements	35
2.6.3.3 Implementation	35
2.6.4 Scintillation Meter	35
2.6.4.1 Photoelectron Emission Data	35
2.6.4.2 Acquisition	35
2.6.4.3 Analysis	36
2.6.5 Electron Probe	36
2.6.5.1 Data Acquisition	36
2.6.5.2 Analysis of EP Data	37
2.6.5.3 Implementation	37
2.6.6 Notes	37
2.6.7 Output File Format	38
2.6.7.1 IESEDRFILE	38
2.6.7.2 IESMECFEILE	39
2.6.7.3 IESAGDBFXR1	39
2.6.7.4 IESSTATFILE	39
3. CRRES ELECTROMAGNETIC FIELD DATA BASES	40
3.1 DATA ARCHIVAL	40
3.2 RADIAL DIFFUSION COEFFICIENT	41
3.2.1 Electric Field Data Quality Checks	43
3.2.1.1 E•B Quality Check (Test 1)	43
3.2.1.2 Low-altitude Measured Magnetic Field Uncertainty (Test 2)	43
3.2.1.3 Biasing of Cylinder Probes (Test 3)	44
3.2.1.4 Large Amplitude Waves Due to Precession after an Attitude Maneuver (Test 4)	44
3.2.1.5 Single Event Upsets (Test 5)	44
3.2.1.6 Electron Injection Events (Test 6)	44
3.2.1.7 Battery Turnoff (Test 7)	44
3.2.1.8 Electrical Short in the Spherical System (Test 8)	44
3.2.2 Initial Analysis Using Flatfile-based Spin-fit Data Base	44
3.2.3 Spectral Analysis with FFT	47
3.2.4 Analysis with Full Variable-Sorted Data Base	48

Table of Contents (Cont'd)

<u>Section</u>	<u>Page</u>
4. GEOSPACE	56
4.1 DEVELOPMENT WORK ON GEOSPACE	56
4.2 THE PRISM MODULE	58
4.3 THE DMSP-SPECTRA MODULE	61
4.3.1 DMSP-SPECTRA Overview	61
4.3.2 DMSP-SPECTRA Inputs	61
4.3.3 DMSP-SPECTRA Outputs	63
4.4 THE CHIME MODULE	63
4.4.1 The CHIME Science Module	63
4.4.2 The CHIME Application Module	64
4.5 The APEXRAD Module	64
4.6 CONCLUSION	66
5. AIR COMBAT TARGET-ELECTRO OPTICAL SIMULATION (ACT-EOS)	67
5.1 INFRARED TARGET SCENE SIMULATION (IRTSS) DEVELOPMENT	67
5.2 MASTER ENVIRONMENTAL LIBRARY DEVELOPMENT	69
5.3 RADIOMETRIC VALIDATION OF CSSM	70
5.4 VISUALIZATION	76
5.5 CLOUD SPECTRA AND CLOUD VERTICAL STRUCTURE FROM SATELLITES	77
6. SCINTILLATION NETWORK DECISION AID (SCINDA)	80
6.1 SCINTILLATION	80
6.2 DEVELOPMENT OF SCINDA	80
6.3 VERSIONS OF SCINDA	83
6.4 MODEL DEVELOPMENTS	83
6.5 SOFTWARE UTILITIES	84
6.6 THE NOVATEL RECEIVERS	85
6.7 PREDICTION AND CLIMATOLOGICAL STUDIES	86
6.8 DEMONSTRATIONS AND PROMOTIONAL MATERIALS	86
7. THE STUDY OF ATMOSPHERIC METALS	87
7.1 MODELING TECHNIQUES	88
7.2 RELATIVE ABUNDANCES OF MESOSPHERIC METALS	91
7.3 MODELING OF METEOR TRAILS	95
7.4 GLO-I DATA ANALYSIS AND MODELING	99

Table of Contents (Cont'd)

<u>Section</u>	<u>Page</u>
8. ANALYSIS AND VISUALIZATION FOR IONOSPHERIC MODELS	103
8.1 IONOSPHERIC MODELING/ANALYSIS SYSTEM (IMAS)	103
8.1.1 PIM	103
8.1.2 WBMOD	104
8.1.3 Ray Tracing	105
8.1.4 Contouring Data System	106
8.2 ASAP VISUALIZATION SOFTWARE	107
8.2.1 MSIS Atmospheric Density Model	107
8.3 VOACAP	107
8.3.1 Development of Graphical User Interface (GUI) for VOACAP ..	107
8.3.2 PIM Input Files	108
8.3.3 Graphical Results from VOACAP	108
 9. SPREE AND CHAWS DATA ANALYSIS	109
9.1 SPREE DATA ANALYSIS	109
9.1.1 SPREE Post-flight Data Support	109
9.1.2 SPREE Interactive Data Analysis Tool (SIDAT)	110
9.1.3 Spacecraft Particle Correlation Experiment (SPACE)	111
9.1.4 STS-75/TSS-1R RELBET Generation	111
9.2 CHAWS DATA ANALYSIS	112
9.2.1 Real-Time Data Processing	113
9.2.2 Postflight Data Processing	114
9.2.3 CHAPS Data Analysis Processing	115
9.2.4 CHUNKS	122
 10. DIGITAL ION DRIFT METER (DIDM)	123
10.1 DIDM-1 DATA ANALYSIS SUPPORT	123
10.1.1 DIDM Data Base	123
10.2 DIDM-2 ANODE DESIGN SUPPORT	127
10.2.1 Anode Response Simulator Application	127
10.2.2 Graphic Design Application	128
 11. REFERENCES	131

LIST OF FIGURES

<u>Figure</u>	<u>Page</u>
1. The SSM data pathway	5
2. Ion Temperatures determined by the three analysis algorithms applied to SSIES-2 RPA sweep data from satellite F12, orbit 12209, day 10 (1997)	24
3. Ram component of the drift velocity determined from the same SSIES-2 data as for Figure 2	26
4. Quality check results for cylinder data, orbit 700	46
5. Valid electric field vector for orbit 700, derived from cylinder data	46
6. Size distribution of valid data intervals over electric field data base	51
7. Size distribution of valid data intervals over electric field data base, for L=3	51
8. Size distribution of valid data intervals over electric field data base, for L=4	52
9. Size distribution of valid data intervals over electric field data base, for L=5	52
10. Size distribution of valid data intervals over electric field data base, for L=6	53
11. Size distribution of valid data intervals over electric field data base, for L=7	53
12. Radial diffusion coefficients in orbits 900-1000 computed by our program (AFRL-Radex) and the University of Minnesota program (UMinn), for L=3-4, for a particle longitudinal drift frequency of 3.1 mHz	55
13. Similar to Figure 12, except that the AFRL-Radex computation used the same intervals as the UMinn computation, disregarding the quality checks	55
14. The dosage for the APEXRAD and CRRESRAD modules	66
15. IRTSS system concept design	67
16. MEL product generator	69
17. Raw pyronometer data for one diurnal cycle	72
18. Spectral analysis of the cloud forcing signal	72
19. Results of the direct upward (left column) and direct downward (right column) flux for the 25% cloud coverage case with the BLIRB model	75
20. Example from the 128x128x64 cloud case	75
21. RADFASE results for a run at 32 GHz with a zenith angle of 65°. A) [Top] Contour plot of the difference in vertical and horizontal brightness temperatures at various cloud water content levels. B) [Bottom] Vertical brightness temperature contours at various cloud water content levels	79
22. SCINDA system concept	82
23. The inputs and flow of computations in a generic representation of our modeling, with "Mg-II Column Density at Noon" meant to represent one of many possible results derived from the model	89
24. Deposition functions for calcium (solid line), sodium (dots) and magnesium (dashes) as computed from the differential ablation model	92
25. The mesospheric ion and neutral layers at dusk as derived from the model for the three metals considered	95

LIST OF FIGURES (Cont'd)

<u>Figure</u>	<u>Page</u>
26. The computed probability of observing a potassium trail from the 1996 Leonid meteor outburst as a function of altitude for two formulations of the eddy diffusion coefficient	97
27. Relative probability of detection (normalized to the maximum of the probability) vs. duration of a trail (panel a) and size of a meteoroid (panel b)	99
28. Predicted radiances from neutral Na due to solar scattering on the geo-magnetic equator near the dawn side (left) and the dusk side (right) of the terminator	101
29. The dusk equatorial anomaly crest, expressed in terms of Mg^+ radiance, as a function of latitude as measured by GLO-I and as modeled	102
30. PIM foF2 is shown at 00:00 UT on 07/06/91 with the IMAS software in GEOSpace	104
31. 2D Australian ray trace for three selected frequencies shown based on PIM plasma frequency levels	106
32. CHAWS instrument and detector fields of view	113
33. CHAPS command process panel	115
34. CHAWS MCP data display	116
35. The CHAWS Langmuir data display	117
36. Trajectory display	118
37. Attitude display	119
38. Orbiter event detail	120
39. Orbiter event display	120
40. CHAWS System Status display	121
41. CHAWS Data Trending Display	121
42. Schematic of DIDM web-based Data Analysis System	124
43. Sample DIDM anode data display	126
44. Sample DIDM/STEP4 Angle Data display	127
45. DIDM-1 anode design	128
46. Sample graphic anode simulator display	129
47. Sample anode simulator response graphs	130

LIST OF TABLES

<u>Table</u>	<u>Page</u>
1. APGA Version History	12
2. Arguments of Subroutine RPA Correspondence to RPAPRC Variables	17
3. Cases Used in Testing RPA Analysis Algorithms	22
4. Variances and Computation Times	23
5. Dependence of Variances on Magnetic Latitude (Satellite F12, Orbit 12209)	23
6. Parameters Describing Real-time Data Input to PRISM	60
7. Contributing Components and Emitting Elements	74

ACKNOWLEDGMENTS

The work described in this report required the involvement and guidance of a number of individuals at AFRL. Their interest and encouragement is gratefully acknowledged.

John Cipar and Ed Robinson of the Wargaming and Technology Assessment Branch initiated and coordinated the activities as the Contract Monitor, over the span of the Contract. Their contributions are deeply appreciated.

Various investigators were involved throughout the projects, and provided essential support and the opportunity for some challenging studies in their fields:

Bob McInerney and Bob Raistrick	VSSW, Wargaming & Technology Assessment
---------------------------------	---

Dave Hardy	VSB, Battlespace Environment
------------	------------------------------

Dana Madsen and Joel Mozer	VSBE, Tactical Environment Support
----------------------------	------------------------------------

Santimay Basu, Keith Groves, Ed Weber	VSBI, Ionosphere Hazards
---------------------------------------	--------------------------

Ed Murad	VSBM, Background Clutter Mitigation
----------	-------------------------------------

Dave Anderson and Fred Rich	VSBP, Space Physics Models
-----------------------------	----------------------------

Don Brautigam, Dave Cooke, Greg Ginnet, Shu Lai and Sue Gussenhoven	VSBS, Space Hazards
--	---------------------

LIST OF ACRONYMS

ACT-EOS	Air Combat Targeting Electro-Optical Simulation
AFGWC	Air Force Global Weather Central
AFRL	Air Force Research Laboratory
AFSMC	Air Force Space and Missile Systems Center
AFSPC	Air Force Space Command
APEXRAD	Advanced Photovoltaic and Electronics Radiation Dose Model
ARL	Army Research Laboratory
ASCII	American Standard Code Information Interchange
AVHRR	Advanced Very-High-Resolution Radiometer
BLIRB	Boundary Layer Illumination Radiation Balance
BSS	bottom side sinusoidal
CAS	CAS shuttle orbiter
CDF	Common Data Format
CDROM	Compact Disk - Read Only Memory
CGI	Common Gateway Interface
CHAPS	CHAWS Analysis and Postflight Survey
CHAWS	Charging Hazards and Wake Studies
CHIME	CRRES/SPACERAD Heavy Ion Model of the Environment
CHOMP	CHAWS Orbital Monitoring Package
COAMPS	Coupled Oceanographic and Atmospheric Mesoscale Prediction System
CPI	Computational Physics Incorporated
CRRES	Combined Release and Radiation Effects Satellite
CSSM	Cloud Scene Simulation Model
DIDM	Digital Ion Drift Meter
DISS	Digital Ionospheric Sounding System
DM	drift meter
DMSO	Defense Modeling and Simulation Office
DMSP	Defense Meteorological Satellite Program
DoD	Department of Defense
DSBMOD	Discrete bubble Model
DSM	SM/DM electronics package
DSO	Dynamic Shared Object
ECI	Earth Centered Inertial
EP	electron probe
EPROM	auroral electron background probability model
ESA	Electrostatic Analyzer
ESF	equatorial spread F

Acronyms (Cont'd)

FDR	Flight Data Recorder
FES	Flash Evaporator System
FFT	Fast Fourier Transform
GLCM	gray level co-occurrence matrices
GLO-I	experiment
GOES	Geosynchronous Operational Environmental Satellite
GPS	Global Positioning System
GSE	Ground Support Equipment
GUI	Graphical User Interface
HMS	hours:minutes:seconds
HOSC	Huntsville Operations Support Center
HTML	HyperText Markup Language
Http	hypertext transport protocol
IGA	International Association of Geomagnetism and Aeronomy
IDL	Interactive Data Language
IGRF	International Geomagnetic Reference Field
IMAS	Ionospheric Modeling/Analysis System
IMS	Information Management System
IONCAP	Ionospheric Communication Analysis and Prediction
IPC	InterProcess Communication
IRI	International Reference Ionosphere
IRTSS	Infrared Target Scene Simulation
JIS	Joint Integrated Simulation
LIS	local interstellar spectra
LT	Local Time
LUF	Lowest Usable Frequency
MCP	micro-channel plates
MEC	model execution control
MEL	Master Environmental Library ,
MEP	Microelectronics Package
MGSE	modified geocentric solar ecliptic
MLT	Magnetic Local Time
MSFC	Marshall Space Flight Center, AL
MSIS	Mass Spectrometer and Incoherent Scatter
MUF	maximum usable frequency
NGDC	National Geophysical Data Center
NRL	Naval Research Laboratory
NSWP	National Space Weather Program
NWRA	Northwest Research Associates, Inc.

Acronyms (Cont'd)

OD	Orbiter Downlink
ODPB	Orbiter Downlink, PlayBack
ODRT	Orbiter Downlink, Real Time
PB	Playback
PI	principal investigator
PIM	parameterized ionospheric model
PL	Phillips Laboratory
PP	plasma plate
PRISM	Parameterized Real-time Ionospheric Model
PUD	PIM User's Guide Display
RCS	Revision Control System or Reaction Control System
RGB	Red-Green-Blue
RMS	Root Mean Squares
RPA	retarding potential analyzer
RSC	RDT&E Support Complex
RSS	Root sum square
RT	Realtime
SCINDA	Scintillation Network Decision Aid
SDD	Software Design Description
SDF	Software Development Files .
SEP	sensor electronics package or solar energetic particle events
SEU's	Single Event Upsets
SFC	Space Forecast Center
SGI	Silicon Graphics
SHDOM	Spherical Harmonic Discrete Ordinates Method
SIDAT	SPREE Interactive Data Analysis Tool
SM	scintillation meter
SNR	signal to noise ratio
SPACE	Spacecraft Particle Correlation Experiment
SPREE	Shuttle Potential and Return Electron Experiment
SSIES	Special Sensor for Ions, Electrons and Scintillation
SSJ4	Particle Spectrometer
SSM	Special Sensor Magnetometers
SSN	sunspot number
STEP	Space Test Experiment Platform
STS	Space Transportation System
STPD	Solar Terrestrial Physics Division
SWXS	Space Weather Squadron .
TCP/IP	Transmission Control Protocol/Internet Protocol

Acronyms (Cont'd)

TSS	Tethered Satellite System
UHF	Ultra High Frequency
UT	Universal Time
VDH	Vertical-Dipole-Horizon
VOACAP	Voice of America Coverage Analysis Program
WBMOD	wide-band scintillation code
WIDA	Weather Impact Decision Aids
WSF	Wake Shield Facility

1. DEFENSE METEOROLOGICAL SATELLITE PROGRAM

The Defense Meteorological Satellite Program (DMSP) is a Department of Defense (DoD) program run by the Air Force Space and Missile Systems Center (SMC). The DMSP program designs, builds, launches, and maintains several satellites monitoring the meteorological, oceanographic, and solar-terrestrial environments. The United States Air Force maintains an operational constellation of two near-polar orbit, sun-synchronous DMSP satellites.

All spacecraft launched have had a tactical (direct readout) and a strategic (stored data) capacity. The data from these satellites are received and used at operational centers on a continual basis. The data are sent daily to the National Geophysical Data Center (NGDC), Solar Terrestrial Physics Division (STPD) archive. A sun-synchronous orbit is a nearly polar orbit in which the satellite always crosses the earth's equator, or any other latitude reference, at the same local time. Initially begun in 1965, over 35 DMSP satellites have been launched. DMSP satellites orbit at an altitude of approximately 830 km. Each satellite crosses any point on the earth twice a day and has an orbital period of about 101 minutes, thus providing complete global coverage of clouds every 6 hours.

1.1 SPECIAL SENSOR MAGNETOMETERS (SSM)

DMSP satellites F12, F13, and F14 are equipped with Special Sensor Magnetometers (SSM). SSM-006 is aboard F12, SSM-004 is on F13, and SSM-003 is on F14. This sensor consists of three mutually orthogonal magnetometers whose axes are aligned with those of the spacecraft. This comprises a vector magnetometer which measures the strength and direction of the total geomagnetic field at the spacecraft location in the range of $\pm 64,000$ nT with a hardware sensitivity of 2 nT. The raw SSM measurement is a vector sum of the magnetic field created by the Earth's internal magnetic field (geomagnetic field) and a disturbance magnetic field created by electric currents flowing along geomagnetic field lines from the ionosphere to the magnetosphere. The disturbance magnetic field changes on time scales ranging from a few seconds to a few hours. The Earth's internal magnetic field is generated by the mass of the solid earth and extends into space. This internal magnetic field is considered to be a static field as compared to disturbance field changes in the ionosphere.

The parameters measured by the SSM are the three components of the magnetic field vector. The SSM magnetometer samples and reports 12 readings per second for the Y and Z axes. Only 10 readings of the 12 readings per second are reported for the X axis due to telemetry limitations. The SSM's axes are aligned with the spacecraft's axes where X is downward and aligned to local vertical within 0.01 degree, Y is parallel to the

spacecraft velocity vector with ascending node in the afternoon/evening sector, and Z is away from the solar panel and anti-parallel to the orbit normal vector. The range is from +65535 to -65535 nT for each axis, with a one-bit resolution of 2 nT ($1 \text{ nT} = 10^{-5} \text{ gauss} = 10^{-9} \text{ Tesla}$). The sensors are described in more detail in *Cook, et al.* [1998].

1.1.1 Objectives of the SSM

The primary requirement for the SSM is to monitor the magnetic field state of the ionosphere. Auroral activity is the predominant phenomenon associated with the magnetic changes in the ionosphere and magnetosphere. The analysis software program, APHB Version 4, permits detection of coherent non-noise based signals down to 20 nT in the processed output magnetic field measurements. By subtracting modeled values for the Earth's internal magnetic field from the raw SSM data, measurements are obtained for the disturbance magnetic fields. These field-aligned currents are generally confined to the auroral zone. Thus, the SSM acts as an ammeter. The SSM data, together with Special Sensor for Ions, Electrons and Scintillation (SSIES), or Topside Ionospheric Plasma Monitor data and Precipitating Energetic Particle Spectrometer (SSJ4) data can determine the energy input to the auroral ionosphere by measuring the Joule heating. Joule heat is the energy released by an electric current flowing through a finite resistor element. The ionosphere acts like a heating element of an electric stove, the magnetosphere acts like an electric power station, and the geomagnetic field lines act as the transmission wires. The SSM data determine the quantity of electric current flowing between the ionosphere and magnetosphere. The SSIES data determine the electric field perpendicular to the field lines which drives the current through the E-layer, and SSJ4 data help to determine the ionospheric conductivity. From Ohm's law, the electrical energy input to the auroral zones can be determined.

In order to estimate the Earth's internal magnetic field, one calculates a model magnetic field using a spherical harmonic expansion equation. Using satellite ephemeris information, APHB calculates the corresponding Earth's internal magnetic field vector in the time and space of the SSM measured vector. The International Association of Geomagnetism and Aeronomy (IAGA) assembles multiple global measurements and applies mathematical modeling to create an International Geomagnetic Reference Field (IGRF) model which becomes the world standard used to generate a representation of the Earth's internal magnetic field. The latest version of this model is IGRF95. Their models are updated every five years. APHB uses the IGRF to supply the coefficients for the spherical harmonic expansion equation.

The SSM instrument is an integral element of the space weather sensors required by the 55th Space Weather Squadron (55th SWXS), formerly the Space Forecast Center (SFC). SSM data are important inputs to magnetospheric and ionospheric models for the determination of Region1/Region2 field aligned currents. This data can also be used as

a secondary source of electric field information for input to magnetospheric, ionospheric, and thermospheric models, and for determining neutral winds.

1.1.2 Scientific and Operational Purposes

A variety of empirical, statistical, and physics-based models have been developed that supply environmental information that is needed for spacecraft design, mission planning, satellite operations, command intelligence systems, and communication networks. The SSM provides direct measurements of the ionosphere and magnetosphere. The analysis software program, APHB, rapidly processes the raw data into pertinent information for the assessment of space environmental hazards, such as loss of radio communications, loss of radar signals, and increased particle drag effects on a satellite due to particle storms.

The 55th SWXS at Schriever AFB, CO operates an Air Force Space Command (AFSPC) space environment forecasting facility that provides general and tailored products describing the current and forecast state of the space environment. The space environment is described by scientific models and applications code integrated into operational systems that interface with real-time environmental data input and output data bases. The SSM is an integral element of the space weather sensors required by the 55th SWXS.

1.1.2.1 Operational Satellites

As of April 1997, there were three active DMSP satellites, F12, F13, and F14. F14 was launched to replace F12. APHB is equipped to process data from these satellites, which have similar hardware and control systems. The APHB program can be updated for duplicate SSM systems on DMSP satellites because of the modular design, which contains a calibration matrix for each individual magnetometer. However, for hardware design changes in the future, a more complex change will be required, that is, F15 is slated to contain a new SSM hardware configuration.

1.1.2.2 In-Flight Calibration and Re-Calibration

The complete SSM sensor module contains three individual magnetometers which are designed to measure magnetic field fluctuations in a 3 dimensional coordinate system, i.e. orthogonal x, y, z axes. Each magnetometer will slightly detect and distort the other magnetometers and their measurement along an axis because they are not perfectly orthogonal. Further, the physical components of the individual magnetometers cannot be totally isolated within the SSM sensor module. The magnetometers must be calibrated to eliminate cross-talk interference from one another, as well as other objects in the local environment. The initial ground calibrations are done both as the sensor is assembled and as it is attached to the main satellite. There is also a high probability that the

magnetometer calibration will change due to physical movement during launch or from atmospheric stresses. Thus, once in orbit, the SSM sensor must be re-calibrated to compensate for all three possible distortions: internal magnetometer non-orthogonality, change in sensor module orientation with respect to the main satellite axes, and the new environment of space. The sensitivity of the instrumentation and normal aging of the whole satellite mandate that the SSM sensor be re-calibrated at regular intervals or after specific large scale environmental changes to the spacecraft.

Once the F12 and F13 magnetometers were in orbit, comparisons of the measured and modeled fields led to the conclusion that the calibrations of the SSM sensors were not ideal. Thus, the sensors were re-calibrated based on data from late 1994. In 1997, improvements to the SSM data processing code in the areas of calculation of the spacecraft orientation, and of removing equipment-operation-induced "jumps" in the measured magnetic field, allowed for improved magnetometer calibration with Version 4 of APHB.

The DMSP F12/SSM006 and F13/SSM004 were successfully calibrated by determining the coefficients which correct for the error between measured field and geomagnetic field on days where the ionosphere magnetic activity is minimal. Consistent results were obtained for several days of calibration, and in-flight calibration matrices chosen. Sensor drift over a year was determined to induce errors in the range of 10-130 nT per axis. Application of these matrices results in F12 and F13 SSM data with improved appearance.

1.1.2.3 F14 In-Flight Calibration

DMSP F14 was launched on April 7, 1997 with SSM-003 aboard. In-flight calibration was successfully performed by determining the coefficients that correct for the error between measured field and geomagnetic field on days when the ionosphere was magnetically quiet. Consistent results were obtained for several days of calibration, and in-flight calibration matrices were chosen. Application of these matrices resulted in improved data. However, a new noise artifact was detected in the measured field. This noise signal introduces an error in the measured-minus modeled data in the critical Z and Y components. This artifact was detected and removed [Cook, *et al.*, 1998].

1.1.3 APHB Documentation

The Software Design Description (SDD) of APHB outlines the structure and function of the program and its subroutines for Version 4. The main program, APHB, is the SSM Data Processing Program, also known as SSM Telemetry To Parameters Converter. The Design Description is organized by sections that correspond to each of the APHB routines, subroutines, and library files, following the top down design of the whole program. Each section contains applicable subsections from the following scheme: a title, a functional

summary, a data dictionary (input, output, local and common variables), a location in the program hierarchy (call list), a list of subroutines and files used, a description of changes to the code for Version 4, a theory and methods review, a list of reference documents, a flow chart, and a copy of the actual FORTRAN source code.

This Software Design Description supplies the general information needed to understand and maintain the APHB code for someone familiar with the DMSP project and similar FORTRAN code. The design description sections are also available in electronic form associated with the source code in a directory for the Software Development Files (SDF). The SSM data pathway is shown in Figure 1 below.

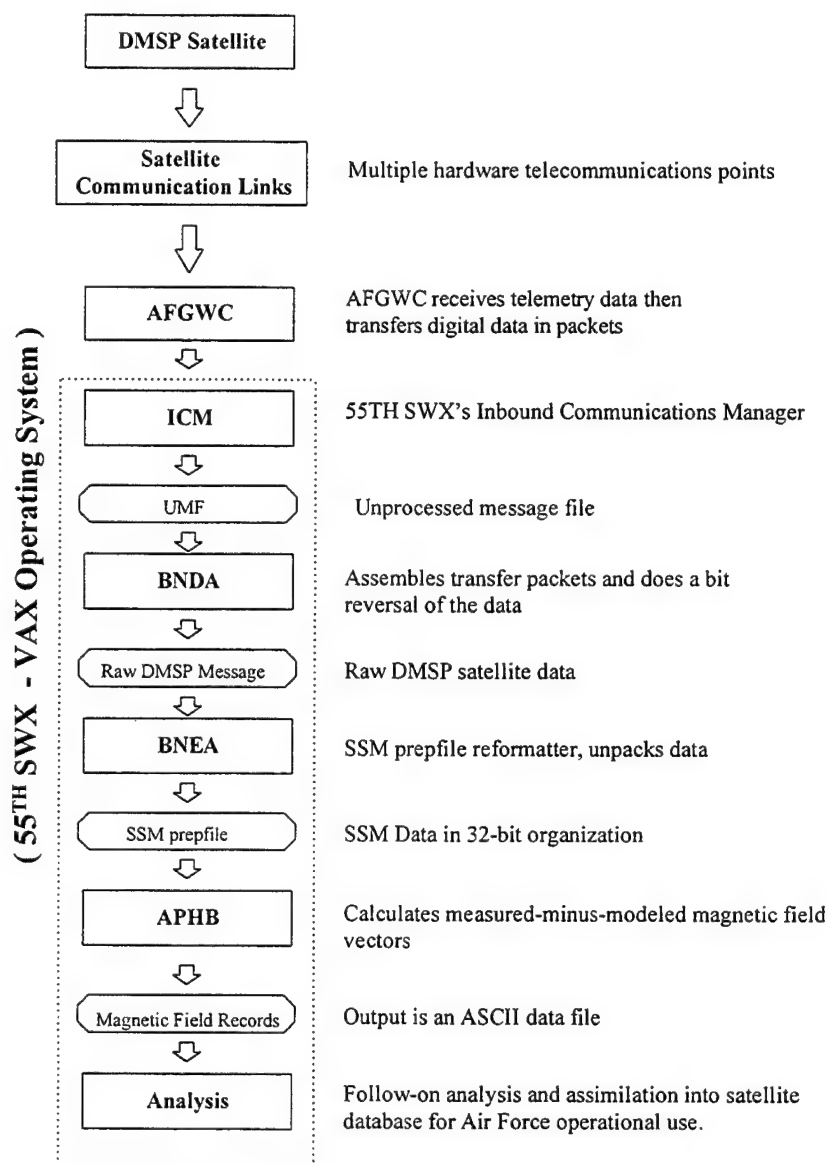


Figure 1. The SSM data pathway.

2. SSIES-3

Measurements by the topside ionospheric plasma monitors (SSIES) aboard satellites of the Defense Meteorological satellite system (DMSP) permit the determination of the state of the topside ionosphere in near-real time. This information is important because the space environment affects ground-based and space-based Air Force systems. Of particular concern are small-scale spatial variations in the plasma density, which cause scintillations interfering with radio frequency communications and early warning systems. The DMSP satellites travel in circular polar orbits at an altitude of 835 km. Software developed at the Air Force Research Laboratory (AFRL) for SCINDA will use plasma density measurements by SSIES near the equator to predict probability of occurrence of equatorial scintillations. At higher latitude, drift velocity measurements by SSIES can be used with other DMSP measurements (see below, in this section) as input to space weather forecast models such as the Magnetospheric Specification Model.

The ionosphere is the ionized region of the earth's atmosphere, extending from 70 km to 1000 km altitude, produced primarily by photoionization of neutral atmospheric constituents, and at high latitudes by ionization by charged energetic particles precipitating down magnetic field lines from the magnetosphere. The upper portion of the ionosphere, above 400 km, is called the topside ionosphere. Here, ion densities range between 10^3 and 10^6 per cm^3 , the main positive ion constituents being singly ionized oxygen, hydrogen and helium atoms. Oxygen is the dominant constituent except in winter mid-latitude. Temperatures generally range between 1000 and 4000 K (0.08 - 0.32 eV), depending on local time and solar cycle, with electrons hotter than ions. Collective plasma motion is characterized by drift velocities 0-1000 km/sec. Below about 60° magnetic latitude the magnetic field lines direct the plasma into the plasmasphere, a region of cold plasma constrained by the crossed perpendicular electric and magnetic fields to move along closed equipotential surfaces. This corotation electric field, directed radially inward toward the earth, due to the rotational motion of the closed magnetic field lines attached to the rotating earth, forces the plasma to follow the earth's rotational motion. The plasmapause, the outer boundary of the plasmasphere, lies along the magnetic field lines traced from the ionosphere at 60° magnetic latitude to their intersection with the magnetic equator at about four earth radii from the center of the earth.

In the magnetosphere, the region outside the plasmasphere and ionosphere, the electric field is dominated by a dawn to dusk electric field due to interaction of the magnetospheric fields and plasma with the interplanetary fields and plasma outside the magnetosphere. Immediately outside the plasmapause, ionospheric ions are convected sunward through the magnetopause, the outer boundary of the magnetosphere. Consequentially an ion trough is found, where the densities are a factor of $10 - 10^3$ lower than in the lower latitude ionosphere. Poleward of the trough, ion densities can be replenished by precipitating particles directed down the magnetic field lines from the magnetosphere. These particles, forming the auroral oval, are sufficiently energetic to ionize the neutral atmospheric gases.

Although on the day side the trough in total ion density disappears or moves to higher latitude, a light ion (H^+ , He^+) trough is found near 60° magnetic latitude. A satellite passing into the light ion trough will see a rapid transition between H^+ and O^+ as the dominant ion.

Analysis of SSIES data provides the following results: O^+ , H^+ , and He^+ densities; the electron density; high-time resolution total ion densities; the ion and electron temperatures; the ion drift velocity; and the spacecraft electrostatic potential with respect to the ionospheric plasma. The drift velocities, combined with the magnetic field measurements by the magnetometer (SSM), permit a determination of the electric field. Knowledge of the electric field, magnetospheric-ionospheric electric currents, also inferred from SSM measurements, and/or ionospheric conductivities inferred from measurements by the precipitating particle sensor (SSJ4), then permits the determination of energy transfer rates from the magnetosphere to the ionosphere.

Ground-based software processes the sensor data telemetered to the ground to yield plasma densities, temperatures and drift velocities in the appropriate geophysical units. The software contains two basic steps [Cornelius and Mazzella, 1994]. In step one, program BNBA unpacks and reformats the raw telemetry data. In step two, program APGA analyzes the reformatted data on the intermediate file produced by BNBA. APGA also uses a control file which is built and maintained by program LDCON02. This file contains sensor constants, control switches, and ionospheric irregularity parameters. An upgraded sensor package, SSIES-3, is expected to be flown beginning in the year 2000. This document describes the detailed software design of program APGA, Version 3, which:

- will perform the analysis for the SSIES-3 sensors, while maintaining functional compatibility with the current APGA Version 2 for the SSIES-2 sensors.

- incorporates the simplex least-squares method [Press, et al., 1992] in the analysis of ion data, for both SSIES-2 and -3. Although the least-squares method promises improved accuracy, it has not been used operationally due to prohibitive computational expense. Improved computational speeds available at present make this approach more feasible. For SSIES-2, the current operational SSIES-2 method is retained as an option. An additional option will allow the initial guess, required for the initialization of the simplex method, to be used as the final analysis result, without further refinement. The initial guess is generated by a method similar in speed and accuracy to that currently used operationally.

- is year 2000 compliant. Version 2 retains only the last two digits of the year, relying on an assumption that all SSIES data will occur in the interval 1985-2084. Use of all 4 digits in dating, including file formats, will remove ambiguity for subsequent processing steps which use APGA output as part or all of their inputs.

2.1 SSIES-3 SENSOR UPGRADES

Previous SSIES packages have included a spherical electron probe (EP) to measure electron density and temperature; a retarding potential analyzer (RPA) to measure ion composition, density, temperature, and the ion drift component in the ram direction (anti-parallel to the satellite velocity); a drift meter (DM) to measure the ion drift velocity components normal to the satellite velocity; and an ion scintillation meter (SM) to measure total ion density, in particular short-time-scale variations, or scintillations.

SSIES-3 will contain a new instrument, the plasma plate (PP), which will work in concert with the RPA to improve the determination of the ion parameters when only O⁺ is significantly present. The parameters that have to be measured are the ion densities, the ion temperature, and the drift velocity component in the ram direction. On previous SSIES sensors, these have been determined by analysis of an RPA voltage sweep in which the data consists of measured current vs. voltage of the RPA's retarding grid relative to the ion sensor aperture. The theory describing this process contains these parameters, plus the electric potential difference between RPA aperture plane and the ambient plasma. For a single ion species, the theory supplies three equations with which to determine four parameters. To overcome this problem, an estimate has been used for either the drift velocity or the potential difference. On SSIES-3 the plasma plate will supply additional data, from its own voltage sweep, to determine this potential difference.

The following paragraphs list the other SSIES-3 modifications that are expected to impact software [Rich, 1994].

The logarithmic RPA electrometer, which measures the current received by the RPA's collector, will be replaced by a multi-range linear electrometer. This should provide better sensitivity at low densities.

The on-board microprocessor will select only a subset of the RPA voltage sweep data for telemetry to the ground. This is intended to be the interesting part of the sweep for the analysis.

The main output of the drift meter is the difference between the logarithms of the currents received by the two members of a collector pair. Two pairs of collectors are present, one for each component of the ion drift normal to the satellite velocity. Over time an imbalance develops between the electrometers connected to a given pair, adding an offset to the output signal. On previous SSIES packages this imbalance was cleared by a "re-zero and offset" technique. However, the associated electronic switching added considerable noise to the output signal. Instead, on SSIES-3, the electrometers connected to a given collector pair will be inverted between successive readings. This will permit a determination of the offset by comparison of signals before and after the inversion: for zero offset the signals should be equal and opposite.

Also, to reduce noise, the drift meter will switch between horizontal and vertical drift measurements only once per second when the scintillation meter indicates that the ion density is low. Normally the instrument alternates between successive measurements, of which there are 12 per second. This will be automatic (SSIES-2 had this feature, except it was activated only by ground command).

The drift meter detection range will be increased to ± 4 km/sec, consequently lowering resolution to 16 m/sec.

The drift meter FIBA and H^+ modes will be eliminated. The FIBA mode consisted of filter banks providing bandpass measurements. The H^+ mode was designed to measure the drift of the light ions, by subtracting the signal of the heavy ions. No software processing has been defined or performed for the data unique to the H^+ mode.

For two seconds of every 512, the scintillation meter will measure photoelectron emission of its collector instead of incoming ions. This will be accomplished by setting one of the bias grids positive, to prevent ions from reaching the collector and emitted photoelectrons from returning. This information may be used to assess the photoelectron contribution to the signals of the various collectors.

Only one electron probe sweep mode will be employed, simplifying the software. This will consist of a 2 second sweep, followed by 2 seconds at constant voltage, then a 2-second sweep in the opposite direction, and finally another 2-second dwell at constant voltage. 96 samples out of each 2-second sweep will be telemetered to the ground over 4 seconds. They will be uniformly spaced in voltage, unlike before, when of the 25 samples generated each second, only the first 24 samples were telemetered. However, the voltages in oppositely directed sweeps will be slightly offset from one another.

Before describing the upgrades to APGA for SSIES-3, we discuss integration of the simplex method software, developed at Air Force Research Laboratory (AFRL) for the analysis of the data of the retarding potential analyzer (RPA) [Rich, 1997, private communication], into the current APGA Version 2.

2.2 INTEGRATION OF THE SIMPLEX LEAST-SQUARES ALGORITHM INTO PROGRAM APGA, FOR SSIES-2

In the retarding potential analyzer (RPA), ions passing through a retarding grid reach a collector, where the current is measured by a calibrated electrometer whose output varies linearly with the log of the current. In SSIES and SSIES-2, the voltage of the retarding grid with respect to the ion instrument aperture plane is swept over 4 seconds between -3 V and +12 V. The sweeps alternate in direction between up (voltage increasing linearly with time) and down (voltage decreasing). Electrons passing through the retarding grid are blocked from the collector by a negatively charged suppressor grid. In SSIES-2, a shield grid has been added, which protects the collector from an additional displacement current

caused by the time-varying potential of the retarding grid.

The goal of the data analysis is to determine the ion densities, temperature and the ram drift velocity component (antiparallel to the vehicle velocity). These plasma parameters can in principle be extracted from the current vs. voltage curve by inverting the theory of *Langmuir and Mott-Smith* [1926]. The difficulty with the least-squares method, which is commonly used to perform such inversions, is that the theory is nonlinear in some of the parameters. As a result the least-squares equations are nonlinear in the unknown parameters for which they must be solved. Therefore an iterative process must be performed whereby an initial estimate of the solution is successively refined until sufficient convergence between successive iterations is obtained. The potentially large computation time has made this approach unattractive for operational use at USAF 55th SWXS, formerly the Space Forecast Center (SFC).

For this reason a simpler method was adapted which identifies key points in the current vs. voltage curve [*Cornelius and Mazzella* 1994]. The theory, adapted by *Smiddy et al* [1978] for a Maxwellian plasma, shows that the contribution of each ion specie to the slope of the current-voltage curve possesses a single minimum at the point where the electrostatic potential energy barrier created by the retarding grid exactly balances the kinetic energy of the ion motion relative to the spacecraft:

$$q\Phi = \frac{1}{2} m_i V^2 \quad (1)$$

where q is the magnitude of the electron charge, ϕ is the potential of the retarding grid relative to the plasma, m_i is the mass of the ion specie considered, and V is the incoming ion speed relative to the spacecraft. The potential ϕ is the sum of two terms, the potential of the grid with respect to the aperture plane, which is known for each point in the sweep, and the potential of the aperture plane with respect to the plasma, which becomes an additional unknown that must be determined. The topside ionospheric plasma consists of O^+ as the main component, with light ions H^+ and/or He^+ sometimes present. When light ions are present one ideally sees two slope minima; the one at higher voltage can be linked with O^+ , while the lower minimum is associated with one of the two light ion species, or a mixture which cannot be resolved. At negative voltages the current achieves a maximum or saturated level. In the operational algorithm the saturated current and the properties of the current at the two minima are used to solve directly for the parameters. The light ions are first assumed to be 100 % H^+ . If the solution shows that the ions begin to be retarded at significantly large negative grid-plasma potential, it is rejected, and the He solution is tried. If it also shows retardation beginning at a negative potential, the sweep is rejected. When only one minimum is found, it is assumed to be O^+ . In this case a completely definitive solution for all the unknowns, density, temperature, ram drift velocity, and aperture potential with respect to plasma, cannot be obtained from this information alone. Therefore at low magnetic latitude the drift velocity is assumed to be zero, and at high latitude, the aperture potential is assumed to be last value obtained from the electron

probe, if valid, or a default value given by the APGA input file IESCNTRLFILE.

The principal problem in applying this method is that noise in the data makes slopes difficult to determine accurately. Therefore, many spurious minima can be found, introducing considerable ambiguity. The slope at each point is determined by a least-squares fit of neighboring points to a straight line. If too many minima are found, the number of points in the fit is increased in an attempt to reduce the number of minima. Even if this is successful in reducing the number of minima to 2, there is still the possibility of a spurious light ion minimum. To guard against this, the algorithm requires, for acceptance of the light ion minimum, that the total current drops, between zero and 3.5 V, to 70% of its low voltage maximum. Despite these precautions, confidence in the results is often limited by the appearance of unsatisfactorily large point-to-point scatters in their time dependencies.

Concurrently with operational analysis at 55th SWXS, a least-squares method has been developed and operated at Air Force Research Laboratory (AFRL), formerly Phillips Laboratory (PL), at Hanscom AFB [Rich 1994]. The procedure consists of three steps: preprocessing, formation of an initial guess, and solution by the simplex method [Press *et al* 1986]. Improved computation speeds have made plausible the belief that the least-squares method could be employed operationally at 55th SWXS as well. Therefore, integration and testing of the least-squares software into the SSIES analysis software has been performed.

2.3 DESCRIPTION OF SOFTWARE

2.3.1 SSIES Analysis Program APGA

Program APGA performs the analysis of the SSIES sensor data at 55th SWXS [Cornelius and Mazzella, 1994]. The data are input from a preprocessor file created by program BNBA, which unpacks and reformats the raw data. Program APGA is responsible for all conversions into science units as well as analysis. The main loop consists of passing around a one-second data frame to the various sensor-specific modules. At the end of each minute, the results of that minute's analysis are written to an environmental data record.

The analysis routine for the RPA is subroutine RPAPRC. Since an RPA sweep requires 4 seconds, analysis can occur at most once per 4 calls. If a sweep has not been completed, RPAPRC stores the data for later usage when the sweep is complete.

APGA Version History

The initial version of APGA, delivered 01 September 1987, was developed by Northwest Research Associates, Inc. (NwRA), for USAF Systems Command Space Division, DMSP Program. The upgrade for SSIES-2 was developed and delivered by RDP Incorporated, 07 March, 1991. Subsequently, RDP delivered an upgrade for use on a VAX platform, on

03 Oct, 1991. Various algorithmic adjustments were engineered by Fred Rich (USAF Research Laboratory) in 1993. Additions for messaging capabilities, use of a model execution control (MEC) velocity file, and file naming revisions, were completed in 1993 and 1994. These were for use at USAF Space Forecasting Center (SFC). Other miscellaneous revisions were applied at various times through 1997, which are described in Section 2.3.4. Table 1 categorizes these developments in terms of version number:

TABLE 1. APGA Version History		
Version	Description	Date Completed
1	Initial Code (SSIES), NWRA, Inc.	01 September 1987
2	SSIES-2 Upgrade, RDP, Inc.	07 March 1991
2.1	VAX Upgrade, RDP, Inc.	03 October 1991
2.1.1	Algorithmic Modifications	1993
2.2	Enhancements for SFC Messaging	03 September 1993
2.3	Enhancements for use of MEC file	11 February 1994
2.4	File naming revisions	12 October 1994
2.4.1	Miscellaneous Adjustments	12 May 1997
2.4.2	Benchmark for this development	31 October 1997
2.5	RPA analysis upgrade (This delivery by Radex, Inc.)	01 January 1998

A planned upgrade for SSIES-3 will have version number 3.0.

2.3.2 AFRL Analysis Routine RPA

The lead module in the AFRL RPA analysis is subroutine RPA. As with RPAPRC, this routine is called once per second, storing the data in memory until a sweep is complete. At completion of the sweep, RPA preprocesses the data. First the 25th sample of each second is filled in by linear interpolation of the neighboring samples. This is done because only the first 24 of the 25 samples generated by the RPA each second are telemetered to the ground. Next the down sweep data are reversed in memory order so that all data henceforth are stored in monotonically increasing voltage order. Then the data are windowed, eliminating samples at negative voltages and setting the high voltage limit at the first sample with zero or negative calibrated, corrected current (down sweeps), or at the first sample with zero raw count (up sweeps). The down sweep criterion is in fact ineffective in SSIES-2, since the correction, due to the displacement current mentioned previously, was eliminated by improved design. The zero or negative currents could occur only as a result of the subtraction of the displacement current from the uncorrected currents. Finally the data are filtered by removing high (raw count ≥ 509) and low (raw count ≤ 100) data samples. Then, if at least 5 points survive the filter, RPA calls subroutine RPADRW to perform the initial guess and the least-squares analysis. Otherwise, the sweep is rejected.

The initial guess is formed by means similar, but not identical, to the operational method used by 55th SWXS. The presence of light ions is determined by whether or not the fractional decrease in current from zero to 3.5 V exceeds a latitude-dependent threshold: 20% for low latitude, 44% for high latitude. An absolute current threshold of 3.2×10^{-11} A at 3.5 V is required to conclude that heavy ions are present. Note that the operational method does not even consider that heavy ions may not be present. If both heavy and light ions are present, one next finds the middle voltage region where nearly all heavy ions contribute to the total current, and all light ions are retarded. This is a region where the slope of the current-voltage curve is approximately zero, while the current is significantly smaller than the current at 0 V. This heavy ion current is subtracted from the total current at lower voltages to obtain the purely light ion contribution, which saturates near 0 V. The currents and voltages where the respective heavy and light ion currents are half their saturation values are used to determine the plasma properties and aperture-plasma potential. When light or heavy ions only are present, the procedure is similar except that no separation into light and heavy ion contributions is needed. As with the procedure used at 55th SWXS, a guess of either the drift velocity or aperture-plasma potential is made to generate the solution. When light ions are present, two guesses of the H⁺ fraction are made: one with 85% H⁺ and the other with 15% H⁺. The solution with the lower sum of squared residuals is accepted.

If the user selects the "fast" method, the estimate just derived serves as the final answer, skipping the least-squares algorithm. If the "slow" method has been selected, the estimate serves as the initial guess for the simplex functional minimization algorithm [Press *et al* 1986]. Note that if light ions were found to be present in the initial guess, the fraction of H⁺ is allowed to vary continuously. Thus, in contrast to the operational method used at 55th SWXS, the light ion composition is unrestricted.

2.3.3 Integration of the Simplex Code into Program APGA

Initial runs of various copies of the APGA code showed that independent modifications had been implemented which resulted in discrepancies in some output results. Thus it was necessary to resolve these differences to produce a reliable benchmark to which the AFRL RPA analysis software could be merged.

2.3.4 Definition of an APGA Benchmark

Two versions of APGA source code were obtained, which we will refer to as versions X and Y. For orbit 2152, satellite flight ID F14, the following differences were found between results generated by these versions

-version Y rejected all RPA down sweeps; version X did not

In subroutine SWPCOL, which is called by RPAPRC to collect the sweep samples, the statement $IBEG = IEND + 2 \cdot INCR$ in the version X appears in version Y as $IBEG = IEND + INCR$. Subroutine SWPCOL is responsible for collecting the 1-second telemetry segment. IBEG points to the location, in a sweep array where the first point of the second is to be stored. IEND points to the last location, and INCR is the increment between successive locations. For voltage up sweeps, INCR is positive, for down sweeps it is negative. This is so that the data will always be stored, lowest voltage in lowest locations, although it is received highest voltage first from the down sweeps. IBEG and IEND differ by 23, showing that 24 samples would be stored each second. In each second, the RPA generates 25 samples, of which only the first 24 (in time) are telemetered to the ground. Thus the 25th point must be left open, to be filled later by interpolation. The statement in question updates the beginning location for the data to be received in the next second. Thus version Y does not leave the 25th point open, whereas the version X does. The result is that version Y does not define the three lowest voltage points in down sweeps. These points are therefore left at their initialized value of zero, which is interpreted as the log of the current, therefore making the current appear to be 1 A for the subsequent filter that is run in subroutine CHKSWP. This filter rejects data differing significantly from the previously accepted data in lower memory locations. The filter accepts the three bad values at the low voltage end of the array, because it has nothing to compare them with; then it rejects all the remaining points; with only three "valid" points remaining, the whole sweep is rejected. For voltage up sweeps the three points at the high-voltage end of the array are undefined; when the filter encounters them it has already typically accepted a sufficient number of previous points to continue the analysis. This discrepancy was resolved in favor of version X.

-In RPA sweeps for which both light and heavy ions are found, the results often differed noticeably;

These were traced to a call, in subroutine RPAALG, which processes a completed 4-second sweep, to subroutine COMPAR, which compares the data with the results obtained from theory for a proposed solution; for two-ion cases, version X passes a variable called CURMIN, which is a density but not a current, while version Y passes a current, FC(9), which is 1/10th of the maximum (saturation) current. The results returned by subroutine COMPAR determine what steps are subsequently taken in the algorithm. The conclusion was that version Y was more correct; therefore, subroutine RPAALG in version Y replaced the routine of the same name in version X.

-The results for some single-ion RPA sweeps differed, near the boundary between the low and high latitude regions, for which the algorithm differs;

In subroutine RPAPRC a table lookup is used to determine the magnetic latitude at any given time; the code for this differs in the two versions; after some examination, it was found that version X would always select the first or second time in the table, whereas version Y would select the closest time to the time of interest; therefore, the apparently more accurate version Y of RPAPRC was substituted into version X.

-After these modifications, including using the "incorrect" version (Y) of subroutine SWPCOL in place of the original in version X, the resulting modified version X still disagreed with version Y in about 1% of the sweeps; most of the differences were not serious.

Up to this point version X had been operated on the SUN workstation (Sparc 20), located at Radex, Inc., while version Y ran on the VMS DEC Alpha (GPSALF) at AFRL. When the version X was migrated to the GPSALF, division by the product of two very small numbers caused floating point overflows in subroutine PLASMA, which is called by subroutine RPAALG to determine the environmental parameters. Version Y had overcome this by the use of a system library function QEXT to convert the numbers to quadruple (16 byte) precision, thereby increasing their range. When version Y of PLASMA was substituted into version X of APGA, the overflow problem was eliminated. Furthermore, agreement was obtained between the two versions for all sweeps. However, incorporation of this change in the Sun implementation of the version X still leaves discrepancies in 22 of the 1500 sweeps. These are generally not serious, and are attributed to roundoff error differences between the SUN and the DEC Alpha workstations.

-Version X was not producing drift meter results:

Version Y was overriding the data value of the LLA/LLB current for flight F14. Implementation of this override in version X cleared that discrepancy.

-The CKL parameter results differed.

This was traced to a table lookup procedure for the magnetic latitude in subroutine CKLPRC, similar to the one noted before in subroutine RPAPRC. Substitution of the version Y form of CKLPRC into the version X of APGA cleared the problem. As with the other table lookup case, version Y of CKLPRC was concluded to be more accurate and has therefore replaced version X.

Summary

From inspection of the source code, it was concluded that version X is 2.1.1 of Table 1, and version Y is 2.4.1. The differences discussed in this section constitute the "miscellaneous" adjustments from version 2.4 to version 2.4.1.

When the version Y forms of the disputed subroutines were inserted into version X in all cases mentioned above, all analysis results obtained on GPSALF agreed with those obtained by version Y on the same hardware. In all but the first case, the version Y form was concluded to be the better of the two, and thus was chosen for use in the benchmark version. In the first case mentioned above, the version X form of subroutine SWPCOL is used in the benchmark version. This therefore is equivalent to version 2.4.1, minus the first miscellaneous adjustment, and the enhancements for SFC messaging (2.2), MEC file

handling (2.3) and file naming revisions (2.4). Subsequently, the MEC file capability has been restored.

The benchmark version of APGA in addition incorporates the following changes:

- An error in subroutine TIMCON, caused by the erroneous assumption that the year 2000 is not a leap year, has been corrected.

- SUN-compatible versions of subroutines ADATE (for measuring wall time) and TIMES (for measuring CP time) have been implemented for operation on that hardware. A main program call to the VMS CP time initializer is deleted from the SUN-operating version.

- The PREPFILE (main input file) I/O software, subroutines OPNPRP and RDPRP, can read ASCII versions of the file; this was found necessary for SUN operation, due to difficulty in producing SUN-compatible binary versions of the file.

2.3.5 APGA-RPA Interface

The modifications were designed to be concentrated almost entirely within subroutine RPAPRC, which is program APGA's a main module for RPA analysis. Therefore there would be little impact on other parts of the program.

2.3.5.1 APGA-RPAPRC Interface

Algorithm Selection: Subroutine INIT has been modified to prompt the user to select the desired algorithm: 0 for the original operational algorithm, 1 for the fast method, and 2 for the slow method, which runs the simplex least-squares method, initialized by the guess provided by the fast method. This algorithm number is passed to subroutine RPAPRC through the common block /RPALGR/.

Raw RPA Data: Subroutine RPA wants the raw RPA data, not the calibrated currents. Therefore the common block /RAWRPA/ has been added, to pass the raw data from subroutine DECODE to subroutine RPAPRC. The data are available in subroutine DECODE, in the INOLS array when they are being converted to calibrated log currents.

2.3.5.2 Subroutine RPAPRC Logic

The method used in the integrated version of RPAPRC is similar to that used in the operational version with the following exceptions:

If either the fast or the slow method is used, the one-second sweep data are loaded by subroutine RPA, which detects whether a complete sweep has been loaded. If that is the case RPA will trigger the analysis, returning a flag to indicate that new results are available,

causing RPAPRC to store them in the in the same locations as subroutine RPAALG for the operational version.

For the fast and slow methods, a new subroutine, SWPSTA, is called instead of subroutine SWPCOL, to generate the sweep status flag, since SWPCOL also collects the data, a function that in this case must be performed by subroutine RPA. The sweep status flag is needed by RPAPRC, regardless of which analysis algorithm is used.

2.3.5.3 Interface Between Subroutines RPAPRC and RPA

Table 2 shows the input and output arguments of subroutine RPA, and the correspondence to APGA variables accessible to subroutine RPAPRC. RPA has been given four new arguments, RPAC, IRPTIML, IRPTIM, and NUMP. RPAC has been introduced because in APGA, the calibrated log currents have already been generated by subroutine DECODE. Since subroutine RPA wants raw currents instead, these have been passed from DECODE through a new common block /RAWRPA/. Passing the calibrated currents also spares RPA the task of regenerating them. IRPTIML is the local frame time in seconds UT. This is passed to RPA so that on return after a sweep analysis it will be able to return the proper sweep time IRPTIM. NUMP, the number of valid points in the sweep analysis, has been introduced for inclusion in the special test output file discussed later.

TABLE 2. Arguments of Subroutine RPA Correspondence to RPAPRC Variables		
Argument (data type given only when different from the default FORTRAN convention)	In/ Out	RPAPRC Correspondence
If analysis fails, the value -999999.0 is returned for those outputs indicated by *		
RPADATA: 1 second of <u>raw</u> RPA INTEGER	In	/RAWRPA/RPADATA
RPAC: 1 second of calibrated RPA data, log ₁₀ currents (A)	In	/DFRAME/RPAC
IONTEMP*: ion temperature, K <u>REAL</u>	Out	/RPAANL/RPITMP
IONDRIF*: ion drift velocity, m/sec <u>REAL</u>	Out	/RPAANL/RPAUR
IONDENS(I), I=1-3*: H ⁺ , He ⁺ , O ⁺ densities, /cm ³ <u>REAL</u>	Out	/RPAANL/RPHDEN, RPODEN, IRPLIF: RPHDEN = total light ion density (H ⁺ , He ⁺) RPODEN = heavy ion density (O ⁺) IRPLIF = 0 (no light ions), 1 (H ⁺), or 2 (He ⁺), -9 if no result If the both H ⁺ and He ⁺ are present, APGA will store the total light ion density as RPHDEN and represent the fraction of light ions that are H ⁺ by setting IRPLIF to 3 + 10000* FRACTION

IONMASS(I), I=1,3: always 1, 4, 16	Out	No correspondence
NM: number of ion species; always 3	Out	No correspondence
SCPOT: Spacecraft potential with respect to plasma (V)	Out	/RPAANL/RPV POT
ERR: RMS of log (measured currents) - log (fit); If ERR > 0.45, IONTEMP, IONDRIFT, and SCPOT are returned as -999999.0; however densities will be returned.	Out	/VARIANCE/SUML, computed in subroutine COMPAR; this common block interface was added only for diagnostic purposes, and may be removed later.
RPAFLAG: Indicates presence of RPA output (once per 4 seconds) <u>LOGICAL</u>	Out	No correspondence
SWPMON: An ion sweep monitor voltage reading; <u>SSIES</u> <u>only</u> <u>INTEGER</u>	In	No correspondence except for SSIES
VAP: Measured ion aperture potential with respect to spacecraft ground (V)	In	/DFRAME/VAPER
VIP: Commanded difference between EP and RPA potentials (V); Actually not used in present version of RPA. <u>INTEGER</u>	In	/DFRAME/VAPER - /DFRAME/VBIAS
CYCOUNT: cycle counter <u>INTEGER</u>	In	/DFRAME/ICCNTR
MAGLAT: geomagnetic latitude (deg) <u>REAL</u>	In	GMLAT
TOLER: Tolerance around nominal sweep voltage values when compared to actual TM values; <u>SSIES only</u>	In	No correspondence except for SSIES
SCVEL: spacecraft velocity (km/sec)	In	0.001*(/SATEPH/VSC)
SUBR: Subroutine to call: 'RPADWF' for fast method, 'RPADWS' for slow method <u>CHARACTER*6</u>	In	/RPALGR/IALGFL = 1 for fast method, 2 for slow method
PRINTCD: Debug printing if zero; no debug printing if 1 <u>INTEGER</u>	In	MOD(IRPDGP+1,2), i. e., the opposite of IRPDGP
OLDAPOT: A previous RPA potential (V)	In/ Out	Initially set = to SPIN; then updated by subroutine RPA;
VIUP(K), K=1-100: Sweep voltages for the 100 up sweep measurements	In	/SWPVLT/SVOLTS(I,1,L) , I = MOD(K,25)+1 L = 10-13 for seconds 1-4 of the sweep
VIDOWN(K), K=1-100: Sweep voltages for the 100 down sweep measurements	In	/SWPVLT/SVOLTS(I,2,L), I and L same as for up sweeps
IMONUP(J), J=1-4: Ion sweep monitor voltage array for checking actual sweep voltages - 4 sec. upward sweeps; <u>SSIES only</u> <u>REAL</u>	In	No correspondence except for SSIES

IMONDN(J), J=1,4: Same as IMONUP, except for downward sweeps; <u>SSIES only</u> <u>REAL</u>	In	No correspondence except for SSIES
TGAP: True if data gap has just occurred, else false	In	ISTAT = KILLED after return from subroutine SWPCOL
DENSRPA: Ion density calculated from average RPA current in saturated region (cm ⁻³)	Out	No correspondence
DRPASDV: Standard deviation of average ion density	Out	No correspondence
IENTYP: 1 for F8, F9, or F10 (SSIES), otherwise 2; only use is test on whether IENTYP is 1 to determine if SSIES-only sweep monitor test is taken	In	/DFRAME/IENTYP
SCIDENT: Flight identifier as 'F##', where ## is the 2-digit identifier, i. e., 09, 09, 10, 11, 12, etc., zero-filled to left <u>CHARACTER*3</u>	In	'F'/(PROCON/IFLT, I2.2)
IRPTIML: Input data frame time of day (seconds UT)	In	/DFRAME/IDTIME
IRPTIM: Sweep time of day (seconds UT); the value of IRPTIML in the 4th second of the sweep	Out	/RPAANL/IRPTIM
NUMP: Number of points used in the sweep analysis	Out	NUMP

Three constants available to RPAPRC through the common block/RPACON/ have replaced hardwired values in subroutine RPA. These are the sensor area, the sensor transparency factor, and the displacement current correction.

The proton mass used by RPAPRC, 1.66035×10^{-27} kg has been replaced by subroutine RPA's value, 1.6726×10^{-27} kg.

2.3.6 Other Changes to Subroutine RPA and its Descendants

Function ERF has been changed from double precision to single precision, because it was being invoked as single precision, leading to erroneous results. Its name has been changed to ERFJV to avoid conflict with a similar function already present in APGA. It was decided to retain both routines, at least temporarily.

For the O⁺ only case, the lower voltage window boundary is set by subroutine RPA to 1.9 V.

Subroutine RPADRW was failing to generate a He-dominated guess when both light and heavy ions were present and a valid 1/2 saturation level was found for heavy ions (as indicated by OFLAG = .TRUE.). Subsequently this guess is compared to the H-dominated guess; therefore it must be defined. This has been corrected by a computation employing the same algorithm as that used for the H-dominated guess, when OFLAG is TRUE, taking account of the dependence on the light ion mass. The already present algorithm for OFLAG = FALSE has been corrected by replacing a reference to an undefined variable HEPOT, and replacing the H⁺ fraction, coded as 0.1, with 0.15, its intended value.

In the light ion only case, the RPADRW code fragment for generating the He-dominated guess contained two typographical errors that have been corrected: the H-dominated average mass, AMASS, was being used instead of the He-dominated mass AMASSHE; and the code was defining X(2), the H-dominated sensor potential, instead of XHE(2), the HE-dominated sensor potential.

Other Modifications to APGA

Binary output of sweep data and results has been added for off-line analysis, in subroutines RPAPRC and RPADRW. The sweep result's file is named RPATEST_XX_YYYYYY_Z where XX is the flight ID (ex: 12 for F12). YYYYYY is the orbit number and Z is the algorithm number. The sweep data file (current vs. voltage) is named VC-BINARY. The details of the contents of these files are given below in section 2.4.3 (operation). A subroutine OPNRPT has been added for opening these files.

2.4 INSTALLATION, MAINTENANCE, AND OPERATION

The VMS delivery package consists of the following:

- The source code for each of the modules, in separate files; the source code file for the main program module is APGA.FOR, while the others are called APGA_x.FOR, where x is one or more characters designating the subroutine or function name.
- Command files MAKEAPGA.COM, FORAPGA1.COM and FORAPGA2.COM. These are used to build the object files, library, and executable from the source code.
- Binary input files IESCNTRLFILE.DAT and IESAPEXTABLE.DAT.

2.4.1 Installation

Although the delivery is set up to read an ASCII prefile, this can be easily switched to read a binary by setting the variable L ASCII PREP to .FALSE. This variable is in a common block, PREP_FLAG, and is defined in a data statement in the main program.

To create object files, a library, APGASUBS.OLB, of the subroutine object files, and the executable, invoke the script MAKEAPGA.COM. This command script calls FORAPGA1 and FORAPGA2 to perform the compilations of the source files; then it creates a library file from the subroutine object files, and performs the linkage to create the executable APGA.EXE.

2.4.2 Maintenance

Although we have no general script for performing updates, they can usually be done by compilation of the changed modules, use of the LIBRARY/REPLACE option to update the library, and invocation of the link command, as in MAKEAPGA.COM:

LINK APGA, APGASUBS/LIB, APGA_DSSIES.OBJ

APGA_DSSIES is a block data definition module, which must be linked directly to force proper initialization of the data variables that it defines.

2.4.3 Operation

The program prompts the user interactively for the RPA analysis algorithm and the name of the prefile. For the algorithm, the user must enter 0 if the present operational algorithm is desired, 1 if the fast method of subroutine RPA is desired, or 2 if the slow method (least-squares) of subroutine RPA is desired.

The output is the same as in the baseline version, except for the interpretation of the light ion flag, and two additional files, mentioned previously, which may be used for subsequent analysis and interpretation.

The interpretation of the light ion flag, which in the baseline version indicates absence of light ions (0), presence of H⁺ ions (1), or presence of He⁺ (2), has been expanded to accommodate the variable H⁺ fraction possible in the outputs of subroutine RPA. The value 0 indicates no light ions, as in the baseline, while 1 and 2 indicate 100% H⁺ and 100% He⁺, respectively. For an arbitrary mixture the light ion "flag" is set to $3 + 10000 \times (\text{H}^+ \text{ fraction})$.

The binary (unformatted) test file RPATEST_XX_YYYYYY_Z, where XX is the flight id, YYYYYY is the orbit number and Z is the algorithm number, has the following contents:

Header record (all INT*4):

Flight id
Orbit number
Nodal year, month, day, packed as YYYYMMDD
Day number in year of the first data readout record
UT (sec) of first data readout record
Algorithm number

Data Records, one per sweep (REAL*4 unless exception noted)

Sweep time, UT seconds (INT*4)
O⁺ density, /cm³
Total (H⁺ + He⁺) light ion density, /cm³

Light ion flag, with new meaning as discussed above (INT*4)
 Drift velocity, ram component, m/sec
 Ion temperature, K
 Sensor potential with respect to the ambient plasma, V
 Number of data points in the sweep (INT*4)
 Variance in log current, measured - fit
 Sweep direction, 1=down, 2=up (INT*4)
 Number of sweeps analyzed so far (INT*4)
 Number of successful analyses so far (INT*4)
 Geomagnetic (APEX) latitude, deg.
 Geomagnetic (APEX) local time, hours
 CP time used (preset sweep analysis), seconds

The binary (unformatted) sweep data file VC_BINARY contains records of uniform length, 2 REAL*4 values. For each sweep there are a header record, a series of data records and a trailer record. The header record contains the sweep time in seconds UT, and the constant 0.0. Each data record contains the voltage (V) and the current (I) of one data sample. The trailer record contains the constants (-999999.0, 0.0) to indicate the end of data for the sweep.

2.5 TESTS

Table 3 indicates the 5 test cases studied, the geomagnetic activity characterizations (active or quiet), and the equatorial crossing local times. Table 4 compares, for the three algorithms, the measured - fit variances in the logs (base 10) of the currents, and the computation times in seconds for the full APGA runs. Here "operational" refers to the algorithm used in the previous versions of APGA, "fast" refers to the algorithm used to generate the initial guess for the simplex least-squares method, and "slow" refers to the simplex least-squares' method, including the initial guess generation.

TABLE 3. Cases Used in Testing RPA Analysis Algorithms				
Satellite	Orbit #	Date	Activity	Local times at Equator Crossings (hr)
F12	12209	1/10/1997	Active	9, 21
F12	15676	9/12/1997	Quiet	9, 21
F13	9288	1/10/1997	Active	6, 18
F13	12753	9/12/1997	Quiet	6, 18
F14	2152	9/04/1997	Quiet	9, 21

TABLE 4. Variances and Computation Times							
Satellite	Orbit #	Variance (log currents)			Computation Times (sec) on VMS DEC Alpha		
		Operational	Fast	Slow	Operational	Fast	Slow
F12	12209	0.226	0.094	0.031	136	141	385
F12	15676	0.096	0.076	0.026	122	125	339
F13	9288	0.099	0.084	0.026	113	116	315
F13	12753	0.178	0.070	0.022	111	120	362
F14	2152	0.052	0.077	0.023	111	114	313

We find that the slow algorithm produces the best fits to the data in all cases. The fast and slow variances are more stable (30 % from minimum to maximum) than the original algorithm (more than 300%). The CP time for the slow method is 5-7 minutes per orbit, compared to 14 minutes that would be required for operational feasibility.

For more detail, we look at Orbit 12209, satellite F12. Table 5 shows the variances for each algorithm within 10° magnetic latitude bins. The slow method is noticeably better than the others in all bins but the highest shown here. This case is not fully typical of the latitude behavior of the variances: for the other cases the operational method produces the best fits at low latitude, but deteriorates significantly at high latitude.

TABLE 5. Dependence of Variances on Magnetic Latitude (Satellite F12, Orbit 12209)			
Magnetic Latitude Bin (degrees)	Operational	Fast	Slow
0 – 10	0.494	0.051	0.022
10 – 20	0.347	0.060	0.021
20 – 30	0.182	0.206	0.052
30 – 40	0.227	0.094	0.030
40 – 50	0.485	0.069	0.020
50 – 60	0.141	0.089	0.027
60 – 70	0.053	0.123	0.052
70 – 80	0.034	0.106	0.045

Figures 2 and 3 show time variations within this orbit. In Figure 2, the top two panels show the geomagnetic latitude and electron temperature, the latter of which was derived by on-board analysis of the data collected by the electron probe, rather than by the software derived here. The periods of lowest electron temperatures (800-1500 K) are in the evening (21 hr MLT), at low to middle latitudes. As the satellite ascends into the north (winter) auroral and polar regions (34000-34500 sec UT), considerable scatter is found in the temperature. As the satellite then descends into the morning (9 hr MLT, 35000 sec UT), the temperature settles into a fairly stable level (3500-4000 K). This level is considerably higher than the evening temperature seen earlier, but it steadily decreases until an increase to almost 5000 K is seen as the vehicle enters the south (summer) auroral region (36500-37000 sec UT). Over the summer polar cap there is again high scatter in the temperature, after which it falls in the interval 38300-38500 sec UT to its evening level.

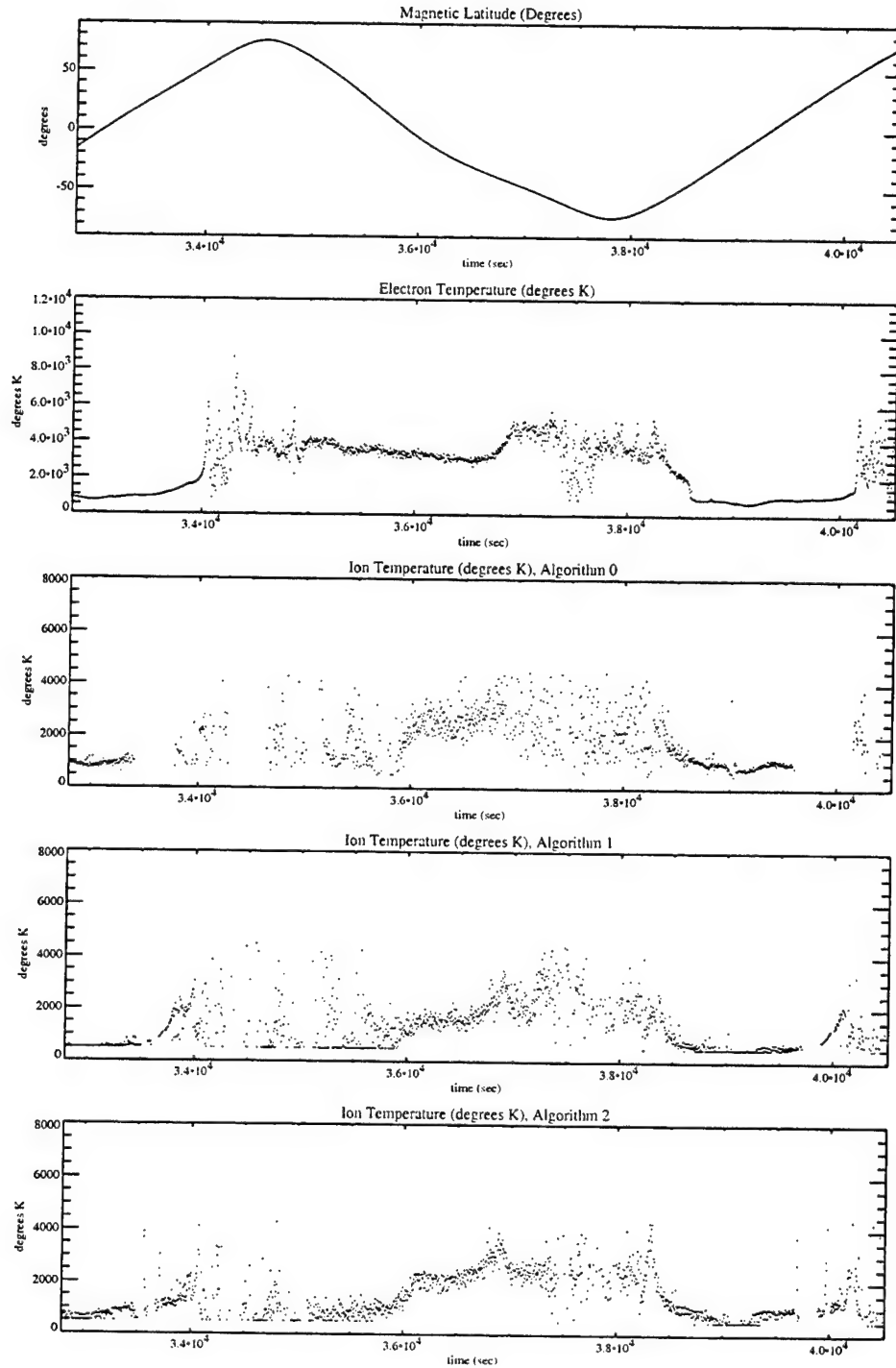


Figure 2. Ion Temperatures determined by the three analysis algorithms applied to SSIES-2 RPA sweep data from satellite F12, orbit 12209, day 10 (1997). The top panel provides the magnetic latitude for reference. The second panel shows, also for reference, the electron temperatures that were determined by onboard microprocessor analysis of electron probe data. The bottom 3 panels show the ion temperatures determined by the operational (algorithm 0), fast (algorithm 1), and slow (algorithm 2) methods.

The remaining three panels of Figure 2 show the ion temperature obtained by the operational (0), fast (1), and slow (2) algorithms. The initial evening temperature is ~1000K, according to the operational algorithm, close to 500 K according to the fast algorithm, and 700 -1000 K by the slow algorithm. Between 33500 and 34000, the algorithms are unable to generate meaningful results, as indicated by the lack of data in this interval. Then as the satellite moves over the winter auroral and polar regions, a few results are obtained, more by the fast and slow algorithms than the operational method. The operational and fast results are very scattered, until the satellite reaches morning MLT equator crossing at 36000 sec UT. During this period, the temperature obtained by the slow method, is more settled, between 500 and 100 K. As the equator is crossed into the summer hemisphere, The temperatures by all three algorithms rise to 1500-2500 K, with the most scatter in the operational algorithm results, and the least scatter in the slow algorithm results, in which distinct structure is seen. The temperature, by all three algorithms, falls back to evening levels at around the same time as the electron temperature falls. Much of the scatter in the auroral and polar regions is thought to be due to exposure to the magnetosphere-ionosphere interactions present there. Small-scale spatial structures might appear as rapid time variations of scales much shorter the time needed, four seconds, to perform the sweep analysis. Low signal to noise in the low density regions poleward of the plasmasphere also contribute to uncertainty in the analysis.

In Figure 3, the top panel again shows the magnetic latitude, for reference when viewing the other panels, which show the ram component of the drift velocity obtained by the three algorithms. Except near the equator, the operational algorithm is able to generate only a few, highly scattered results. The fast and slow methods do better, but the fast method displays two levels of results near the equator. The bunches are believed to be related to the selection of one or the other of the two alternatives for the $H^+/(H^+ + He^+)$ ratio, which may be dependent on sweep direction. The slow method, which can adjust this parameter, reduces the bunching.

Further refinement of the algorithms may reduce the scatter seen in these results. Suggested improvements include refinement of possibly incorrect sweep voltages, expansion of the analysis window into the negative voltage region, to ensure accurate determination of the saturation current, and a smoothing of the current vs. voltage data.

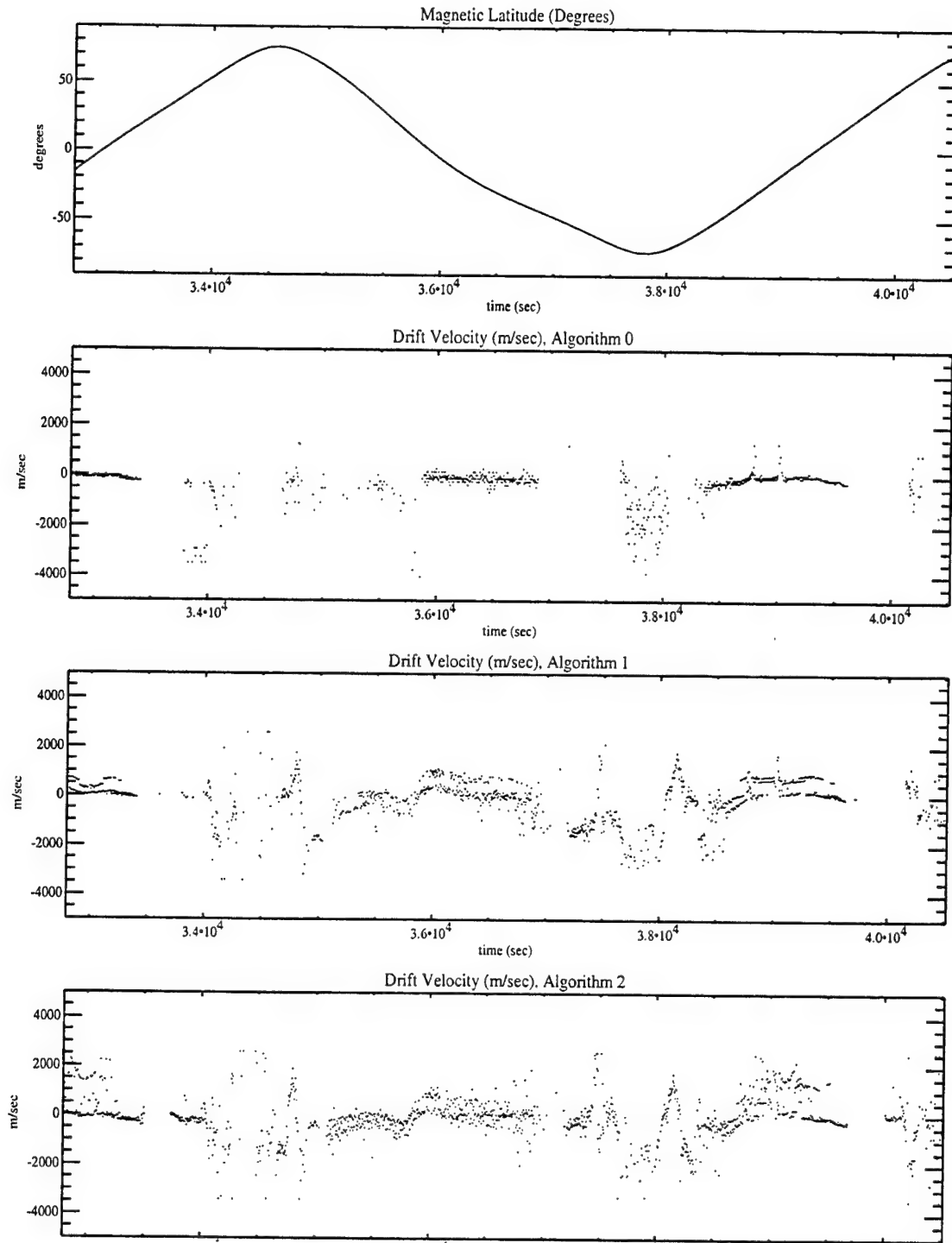


Figure 3. Ram component of the drift velocity determined from the same SSIES-2 data as for Figure 2. The top panel shows magnetic latitude, for reference, and the bottom 3 show the results determined by the three algorithms.

2.6 PROGRAM APGA MODIFICATIONS FOR SSIES-3 (APGA VERSION 3)

In the introduction, we outlined the SSIES sensor upgrades that will be embodied in the new, SSIES-3 sensor types to be flown beginning in the year 2000. Here we define in more detail these changes and the algorithms that have been developed for processing the data. In addition to SSIES-3 processing, APGA Version 3 retains the functionality of SSIES-2 processing, through that described in the previous section for the RPA analysis: the inclusion of new RPA processing algorithms, the fast and slow simplex methods. The SSIES-2 processing function has been validated through comparison of test results with Version 2.5, discussed above. The SSIES-3 processing function is at this point untested. Initially, BNBA will construct the RIR and ephemeris records in the PREPFILE in the same format as currently used. Thus, APGA upgrades for the time being are concerned only with the revised sensor data format in the PREPFILE. Ultimately, if resources are available, appropriate upgrades to APGA will be made to permit use of the improved RIR and ephemeris data that will exist at SWXS once the new DMSP Data Ingest, Processing and Storage (DIPS) upgrade comes on line.

2.6.1 RPA and PP

In SSIES-3, the analysis of the data from the ion retarding potential analyzer will be enhanced by the presence of a new instrument, the plasma plate (PP). The RPA retarding grid voltage is swept relative to the fixed ion aperture voltage. In the basic analysis, one finds minima in the slope of the current vs. voltage curve. There should be one such minimum for each ion species significantly present. Usually at most, two such minima are found, one corresponding to H^+ and He^+ , which cannot be resolved, and one for O^+ . Most of the time only one minimum is present, which is assumed to be due to O^+ , since that is always present in the ionosphere. If two minima are found, all the required parameters can be solved for. However, if only one is present, we have only three pieces of information with which to determine the four required parameters: the ion number density, temperature, and ram velocity, and the ion aperture potential relative to the plasma. In previous SSIES's, this problem handled by assuming that the ion ram velocity is zero between + 50 and -50 deg. geomagnetic latitude, or that the ion aperture potential is either 0, or equal to the value found by last successful RPA analysis, or by the electron probe analysis. The plasma plate provides an opportunity to better estimate the aperture-plasma potential difference by recording net (ion + electron) currents on the ion sensor array aperture plane, in contrast to the main electron probe, which is located at the end of a boom at some distance from the ion aperture plane.

2.6.1.1 Reading and Interpreting the Raw Data

For each 2-second period, the RPA will execute one long sweep (RPALU, RPALD) in each direction, up and down, at the voltage range sufficient to detect both heavy and light ions. There will also be one short sweep, RPASS, at approximately one third the long sweep voltage range, in order to concentrate on detecting light ions, if they are present. The

plasma plate will execute 2 sweeps, only one of which will be telemetered. Both RPA and PP currents will be measured with linear ranging electrometers, in contrast to the sensors flown previously, which worked with logarithmic electrometers. Each will have 8 ranges selectable by the microprocessor, which will also select the samples of each sweep to be telemetered to the ground.

2.6.1.2 Acquiring the RPA Sweeps

In the RPAL sweeps SSIES-3 will generate 36 raw samples, with voltages given as follows:

$$V(1) = V_{ap};$$

$$V(k) = V_{ap} + 1.875 + 0.375 \cdot (k-2), \quad k > 1$$

where V_{ap} is the aperture voltage, given in TM word 6, cycle 1, and in IESPREPFILE, tentatively in word 9, both cycles.

The telemetry will receive the first two samples, and 13 consecutive additional samples, beginning with sample # KMAX (subset location parameter), selected by the microprocessor. KMAX is given in TM word 65, cycle 1, bits 1-5 (RPALU) and word 25, cycle 2, bits 4-8 (RPALD). In IESPREPFILE, KMAX is tentatively assigned to word 89, cycle 1 for RPALU, and word 89, cycle 2 for RPALD. The voltage for the j th telemetered sample is then

$$V_t(1) = V(1)$$

$$V_t(2) = V(2)$$

$$V_t(j) = V(KMAX+j-3), \quad j > 2$$

Currents: Telemetry will receive one RPALU (long upward) and one RPALD (long downward) sweep per 2 seconds, as unsigned 11-bit words, $LSB = 0.0025$ V. There will be 15 values per sweep. In IESPREPFILE, these are tentatively assigned to words 58-72, RPALU in odd seconds, RPALD in even seconds. Calibration constants will be required to convert from V to amps. These will depend on the range parameter, which is given in TM word 66, cycle 2, bits 3-5, and is tentatively assigned in the IESPREPFILE to word 125, cycle 2. Calibration constants will be required on the IESCNTRLFILE for each of 8 the RPA ranges.

In the RPASS sweeps SSIES-3 will generate 36 samples with voltages:

$$V(l) = V_{ap} + (l-1) \cdot 0.125$$

The telemetry will receive the first sample and 10 other consecutive samples beginning at sample # IMAX, where IMAX is given in TM word 12, cycle 1, bits 0-4, and tentatively in IESPREPFILE word 84, cycle 1. Then the j th telemetered sample voltage is

$$V_t(1) = V_{ap}$$

$$V_t(j) = V(IMAX+j-2), j > 1$$

Currents: TM will receive the currents as unsigned 11-bit values, negative set to 0, LSB = 0.0025 V (the same as for RPAL sweeps). There will be 11 values per sweep, which in IESPREFILE are tentatively assigned to words 73-83, cycle 1 (only 1 such sweep per 2 sec.). The cal constants should be the same as for the RPAL sweeps.

Software: The 36 sample voltages of each sweep may be computed by subroutine VSWEAP. It will be left to subroutine SWPCOL to collect the selected voltages to be telemetered. Subroutine DECODE must be modified to perform the conversion from raw TM to engineering units subject to the linear ranging (presently a logarithmic electrometer is assumed). The calibration constants for each of the 8 ranges must be on the IESCNTLFILE, which is accessed by subroutine INIT.

2.6.1.3 Acquiring the PP Sweeps

SSIES-3 will generate 20 raw samples at voltages given by:

$$V(1) = V_{ap} + PPRNGV$$

$$V(k) = V_{ap} + V_{start} + (k-2)*DV,$$

where PPRNGV is one of 4 possible values at which the PP range is determined, set by command, and given in TM word 3, cycle 2, "second" 3, bits 2-3, via table lookup. Vstart is given by combining TM word 65, cycle 1, bits 6-8 with TM word 66, cycle 1, bits 0-8, and DV is given by combining TM word 12, cycle 2, bits 5-8 with word 13, cycle 2, bits 0-3. Telemetry will receive sample #1 plus 9 other consecutive samples beginning with # KC, where KC is given by combining TM word 10, cycle 2, bit 8, with word 11, cycle 2, bits 0-3. Then the voltage of jth telemetered sample is given by:

$$V_t(1) = V(1)$$

$$V_t(j) = V(KC+j-2)$$

The tentative IESPREFILE assignments are:

Vap: word 9, all both cycles

PPRNGV: word 90, cycle 1: a table lookup, 00 = -3.001 V, 01 = -3.998 V, 10 = -5.998 V, 11 = -8.002 V

Vstart: word 83, cycle 2: signed 2's comp., 12 bits, LSB = 0.00464 V

DV: word 87, cycle 2: unsigned 8-bit 2's comp. LSB = 0.00464 V

KC: word 88, cycle 2

Currents: TM will receive the 10 samples as unsigned 11-bit numbers, LSB = 0.025 V (magnitude portion of 2's complement). The measured current can be positive or negative during the sweep. If KC Mode is Auto, the parameter KPP is the first sample where the sign is opposite the sign of the sign of sample #1, which nominally will be positive. Otherwise,

KPP is KC+4. KPP is in TM word 11, cycle 2, bits 4-8 and tentatively in IESPREPFILE word 85, cycle 2. The KC Mode is in word 3, cycle 2, "second" 5, bit 3, of the TM, and is tentatively assigned to word 148, cycle 1, in the IESPREPFILE. Thus, when the KC Mode is Auto, beginning with sample KPP, the remaining values are negative, and the negative sign should be tacked on as bit 11, to form a proper 2's complement number. Calibration constants are needed to convert to amps, one set for each of 8 ranges. As for the RPA, the PP calibration constants are expected to be stored off-line on the IESCNTLFILE, to be read in during initialization.

Software: The software subroutines impacted are the same as for the RPA.

2.6.1.4 Analysis

The objective will be to determine the same set of ion parameters as done previously with just the RPA. One complete data set for these instruments is available per 2 seconds. This includes two RPA long sweeps, 1 short sweep, and one PP sweep.

2.6.1.5 RPA Sweeps

The analysis is similar to the RPA analysis of previous SSIES missions, with the exception that, in the presence of just one ion species, the option will exist to use the PP sweep data, rather than assumptions used previously to reduce the number of unknowns. Software impacted includes subroutine RPAPRC and the routines it calls.

2.6.1.6 PP Sweeps

The plasma plate will measure total ion + electron current. The first point (lowest voltage) is $V_{ap} - 4$ volts, which nominally will exclude electrons and provide, therefore, a measure of the total saturated ion current. We assume, in the region where the ions are attracted and the electrons are retarded, that the ion current is fixed, as for the RPA:

$$I_i = ANqV_p \quad (2)$$

Where

A = PP surface area

N = ion number density

q = ion charge

v_p = ion flow speed into the satellite

$= v_s + v_d$

v_s = satellite speed

v_d = ram component of the plasma bulk velocity

Subtracting the ion current, as given by the measurement at the first point in the sweep, from the total ion + electron measured current at subsequent points, we obtain the electron current, as a function of sweep voltage. In the electron-retarding region, this is given by:

$$I_e = ANe \left[\frac{kT_e}{(2\pi m_e)} \right]^{1/2} \exp \left[\frac{-e\phi}{(kT_e - e)} \right] \quad (3)$$

where

e = electron charge

k = Boltzmann's constant

T_e = electron temperature

m_e = electron mass

ϕ = PP potential with respect to the plasma

$= \phi_p + \phi_s$

ϕ_p = PP potential with respect to the aperture

ϕ_s = aperture potential with respect to the plasma

The term ϕ_s is unknown and assumed constant through the sweep, while ϕ_p is known and varying during the sweep. From the logarithmic slope of the electron current magnitude vs. ϕ_p , we can obtain the electron temperature T_e . Then if we define ϕ_{p0} as the value of ϕ_p at which the total measured current (ion + electron) is zero, we get the relation, given that the electrons and ions are equally but oppositely charged:

$$\phi_s = -\frac{kT_e}{e} \ln \left[v_p \left(\frac{2\pi m_e}{kT_e} \right)^{1/2} \right] - \phi_{p0} \quad (4)$$

This provides a relation between the unknown potential ϕ_s and the total plasma bulk flow into the vehicle, v_p . A second relation between these quantities is obtainable from the energy balance, Eq. (1), between the kinetic energy of the drift motion and the electrostatic potential energy at the voltage where the slope in the RPA current-voltage characteristic minimizes, corresponding to depletion of half of the ions:

$$v_p = \left[\frac{2q(\phi_{RO} + \phi_s)}{m_o} \right]^{1/2} \quad (5)$$

where m_o is the ion mass, and ϕ_{RO} is the retarding potential, with respect to the aperture plane, at which the slope of the RPA ion current vs voltage curve minimizes.

Using these two relations we can solve for the two unknowns v_p and ϕ_s . Substituting this expression for v_p into the previous equation we obtain:

$$\phi_s + \phi_{p0} = \frac{kT_e}{2q} \ln \left[\frac{2q(\phi_{RO} + \phi_s)}{m_o} \frac{2\pi m_e}{kT_e} \right] \quad (6)$$

If we define normalized potentials $\theta_i = \phi_i / [(kT_e)/(2q)]$ we can simplify this to:

$$x - \ln x = \theta_{RO} - \theta_{p0} + \ln \left(\frac{2\pi m_e}{m_o} \right) \quad (7)$$

where the unknown to be solved for is $x = \theta_{RO} + \theta_s$, with the two terms on the right being the normalized potential for the minimum in the RPA sweep and the normalized aperture potential with respect to the plasma. Since the left hand side has a minimum of 1 at $x=1$, the equation can be solved only if the right hand side is at least 1.

If this condition is satisfied there are two solutions, one of which is greater than unity, and the other of which is less than unity. The solution less than unity requires that $q(\phi_{RO} + \phi_s)$, the kinetic energy of the ions due to their motion relative to the spacecraft, be less than $kT_e/2$. For $T_e = 9000$ K, an extreme case, the net ion velocity relative to the spacecraft would have to be less than 2.2 km/sec. Given the spacecraft velocity, 7.44 km/sec, an ion "tailwind" of over 5 km/sec, for O^+ ions, would be required. Barring such extreme conditions, we should therefore select the solution greater than unity. The Newton-Raphson method is appropriate for solving the equation, given that the left hand side of the equation and its derivative with respect to x can be obtained analytically. Once we obtain the solution, the plate potential and ion ram velocity are easily obtained, and the rest of the parameters can be found by the same methods as for the previous SSIES missions.

Failure of the right hand side of Eq. (7) to be greater than unity indicates that one or more of the parameters Φ_{RO} , Φ_{p0} , or T_e are incorrect. In this case we could fall back on methods used in previous SSIES missions. Alternatively, we could use some or all of the parameters obtained by the on-board analysis, performing a partial ground analysis, or no analysis, respectively.

2.6.2 Implementation in APGA Version 3

Subroutine RPAALG3 is called by RPAPRC to collect the data from the 3 sweeps and perform the analysis at the end of even seconds when data from all three RPA sweeps (long up, long down, and short sweep) have been stored internally. The number of points available is 41, 15 each from the two long sweeps, and 11 from the short sweep. High and low points (raw values > 2056 or < 1000) are eliminated. The remaining data are converted to currents and merged into a single super-sweep. In this processing, pairs of points, that came from different sweeps, and are too close in voltage, are combined into one by averaging their logarithms. If at least 5 points remain, subroutine RPADRW is called to continue the processing. Otherwise RPAALG3 returns with null result.

The output files for SSIES-2 accommodated only one output set per 4 seconds. Since this limitation must be maintained for SSIES-3, the results of two consecutive 2-second data sets are averaged to produce a single 4-second output set.

Subroutine RPADRW follows the same procedure as in APGA Version 2, except that if only light or only heavy ions are found to be present, RPADRW invokes subroutine SOLVE to

obtain the drift velocity ram component, temperature, and the aperture potential with respect to the plasma. SOLVE, in turns, calls subroutine PPALG to perform the plasma plate analysis algorithm described above, in an attempt to obtain a solution for the velocity and potential without guessing. If PPALG is successful, then its solution is used to obtain the temperature. Otherwise the guessing procedure used for SSIES-2 is employed

PPALG collects the raw values, detecting the change of polarity at the point where the raw value exceeds 1024, in accordance with the 2's complement format, and converts them to real currents. Before proceeding with the analysis several tests are conducted to weed out conditions for which valid results cannot be obtained. If any of the following are true, PPALG returns an error flag equal to TRUE to indicate failure:

- a) The first occurrence of large negative current is not within the telemetered samples.
- b) The first sampled current is negative.
- c) The last sampled current is positive.
- d) The first current is not the highest

Otherwise, the electron temperature TE is computed from $TE = Q/(K*SLOPE)$, where Q is the magnitude of the electron charge, K is the Boltzmann constant, and SLOPE is the derivative of the log of the electron current magnitude with respect to the sweep voltage. Then Equation (7) is solved for x by the Newton-Raphson method, initializing at x=2, and limiting the number of iterations to 10. The analysis stops, and error flag TRUE is returned if any of the following occurs:

- e) The electron current slope cannot be found, or is negative,
- f) The right hand side of Equation (7) is less than 1.
- h) The Newton-Raphson procedure fails to converge in 10, or fewer, iterations.

If the analysis succeeds the error flag is set to FALSE, to indicate success, and the resulting potential and velocity are returned.

2.6.3 Drift Meter

The collector in the drift meter consists of 4 quadrants arranged such that the total current to each adjacent pair is measured by a logarithmic electrometer. The difference between the readouts of the electrometers connected to opposite pairs of collector quadrants determines the ratio of the component of drift velocity along one of the two axes normal to the spacecraft velocity, to the ram component speed of the ions relative to the spacecraft. By rotating the electrometer connections among the various collector quadrant pairs, one can obtain positive and negative drift velocity component measurements in both horizontal and vertical directions. The measurement of both positive and negative components is new in SSIES-3. It is being done to improve estimation of the zero offset that develops between the two electrometers, since, for truly zero offset, the oppositely directed readouts would in

principle be equal in magnitude, but opposite in sign. The zero offset must be subtracted from the raw electrometer difference measurement to obtain the drift velocity.

The drift meter in SSIES-3 will run in two modes: normal and slow. The FIBA and H⁺ modes used in SSIES-2 will not be used in SSIES-3. The normal mode in SSIES-3 will differ from that used in SSIES-2: measurements will be rotated between the negative vertical component of the drift velocity (V1), the negative horizontal component (H1), the positive vertical component (V2), and the positive horizontal component (H2). Four such cycles (12 measurements) will be completed per second. In DM coordinates, vertical is positive in the upward direction, and horizontal is positive to the right, as viewed by the incoming plasma. The first measurement in a second will always be V1, and the measurements will cycle in the order V1, H1, V2, H2. The switching will be implemented by rotating connections of the electrometer pair among the collector quadrants. In the slow mode, which will be implemented either by ground command, or automatically when the scintillation meter is in range 1, the switching of electrometer connections will be done only once per second. Thus, when the slow mode comes on the first second will be a V1 measurement, followed H1 in the second, etc.

2.6.3.1 New Handling of Offset Due to Electrometer Imbalance

The formula for the drift velocity component is [Rich, 1994]

$$V_{H \text{ or } V} = (V_s + V_D) (0.01 \times \text{Counts} - V_{\text{zero}}) \times C_D$$

where V_s is the spacecraft speed, V_D is the component of the plasma drift in the spacecraft velocity direction (set to zero, or measured by the RPA), V_{zero} is the zero offset voltage, and C_D is a calibration constant. In SSIES and SSIES-2, V_{zero} is given by preflight calibrations, or supplied directly in the telemetry, or post-flight analysis of previous flights (most recently the constant 2.56 V, from analysis of F8-F10 data). In SSIES-3, one may in principle estimate V_{zero} by adding the results of oppositely directed pairs of measurement (i. e., $(V1+V2)/2$, $(H1+H2)/2$, etc.). However, this method may be compromised at high latitudes, where a significant variation of the drift velocity between successive positive and negative horizontal or vertical measurements could masquerade as a zero offset. Therefore, it is recommended that the zero offset be obtained by averaging over previously collected low-latitude data, on the assumption that the true zero offset should remain stable over an orbit. Initially, at the beginning of the orbit, one may use the results at the end of the previous orbit. Rather than a straight average, in which the old data will overwhelm the new, one may apply some deweighting factor to the old data, so that previous measurements become "forgotten" over time. Thus, an updated estimate could be computed as:

$$V_{\text{zero}}(\text{updated}) = a V_{\text{zero}}(\text{old}) + (1 - a) V_{\text{zero}}(\text{current}), \quad (8)$$

where $V_{\text{zero}}(\text{old})$ is the previous best estimate of the zero offset, $V_{\text{zero}}(\text{current})$ is the zero offset implied by the current set of measurements, and a is a weighting factor. The setting in the software that has been developed is presently 0.1, but is subject to change.

2.6.3.2 Modified Scheduling Of Horizontal and Vertical Measurements

Bit 0 (LSB) of the mux flags (TM word 61) indicates whether the DM is in slow (0) or normal (1) mode. This flag has been tentatively assigned to word 132 (both even and odd cycles) of the IESPREPFILE data base. In the slow mode, only one component will be analyzed in any given second. This will use the last sample in the second, as recommended by *Holt*, [1995]. For the zero offset voltage, v_{zero} , the most recent estimate obtained from the normal mode will be used. In slow mode, the processing should therefore output just one measurement per second as opposed to 6 for each component in the fast mode. The output must include a flag to identify the mode (normal or slow) and, when in slow mode, a second flag to identify the component as either horizontal or vertical.

2.6.3.3 Implementation

The SSIES-2 module DMPRC has been renamed DMPRC2, and is called for SSIES-2 data. For SSIES-3, a new module, DMPRC3 has been written. Subroutines DMINFO and DMCMD have been recast in similar fashion to reflect differences in status flags and command formats that take effect in SSIES-3..

2.6.4 Scintillation Meter

The scintillation meter measures total ion density at high time resolution. It outputs a DC signal at 24 samples/second, and the density fluctuations within 6 filter bandpasses once per second. Changes of instrument measurement range are signaled by control flags embedded in the data. The main change in SSIES-3 is that in 2 seconds out of 512, when the cycle counter, given in word 1 of each frame, is 3 or 4, the scintillation meter will measure photoelectron emissions by its collector, instead of ions received by the collector.

2.6.4.1 Photoelectron Emission Data

During the photoelectron (PE) mode, the collector potential will be set to -27 V, relative to the aperture plane, to exclude incoming thermal electrons and low energy atmospheric photoelectrons. The suppressor grid will be set to +20 V to exclude ions. The shield grid will be stepped from -25 V to -40 V (+2 V to -13 V with respect to the collector). The current as a function of shield voltage will be measured at 48 evenly spaced steps over the 15-volt range, 15/47 volts per step.

2.6.4.2 Acquisition

A new software routine will be required which will be entered whenever the cycle counter is 3 or 4. Its job will be to collect up to 24 samples in each second of the current vs. voltage data acquired during the shield grid voltage sweep. Electrometer range changes will be flagged as in normal mode, by insertions into the data stream which would overwrite the

data samples, reducing the number of valid data samples from the maximum of 24 per second.

2.6.4.3 Analysis

Analysis of the photoelectron mode has not been defined. Therefore, if the SM is in the PE mode the subroutine returns without processing or producing output.

2.6.5 Electron Probe

The electron probe will operate in one mode only, in contrast to previous SSIES sensor packages, in which up to 9 modes were present. In this mode, the EP (electron probe) will perform an upward or downward voltage sweep for 2 seconds, followed by a constant voltage dwell, also for 2 seconds.

2.6.5.1 Data Acquisition

In each 2-second upward or downward sweep, the electron probe will generate 192 samples of current, half of which (96 samples) will be telemetered to the ground. Twenty-four samples per second will be transmitted during the 2 seconds of the sweep, and 24 samples per second will be transmitted during the following 2 seconds when the probe is at constant voltage. Odd-numbered samples will be sent during upward sweeps, even-numbered samples during downward sweeps, where sample 1 is at the highest voltage, and sample 192 at the lowest voltage, regardless of sweep direction. Only the currents will be sent; the voltages, relative to spacecraft ground, corresponding to the 192 sensor-generated sweep samples are given by:

$$\begin{aligned}V(I) &= V(1) + [V(192) - V(1)](I-1)/191; \\V(1) &= V_{ap} + 1.8 \text{ volts} + V_{offset} + d_1; \\V(192) &= V_{ap} - 6.2 \text{ volts} + V_{offset} + d_{192};\end{aligned}$$

where V_{ap} is the ion aperture voltage, given in TM word 6, cycle 1, as a signed 2's complement 9-bit quantity, with the LSB (least significant bit) = 0.16 volt. V_{offset} is an offset voltage added to the nominal sweep range to prevent large positive excursions. It is set by ground command and is given in TM word 3, cycle 2, "second" 7, bits 0-3; V_{offset} is one of 11 uniformly spaced values, such that 0 = -3.5 volts, 10 = +7.5 volts. In the IESPREPFILE, the tentative assignments are:

V_{ap} : word 9, both cycles
 V_{offset} : word 127, cycle 2

The quantities d_1 and d_{192} are offsets of the sample 1 and sample 192 voltages from the extreme top and bottom limits of the sweep, respectively. Their values are expected to be constants, but at present are TBD.

If we number the samples telemetered with index j , running from 1 to 96 (1 for highest voltage, 96 for lowest), and the j 'th telemetered sample voltage is $V_t(j)$, then

$$V_t(j) = V(2*j-1) + V' ;$$

where

$V' = 0$ when the odd-numbered raw samples are telemetered;

$V' = V(2) - V(1)$ when even-numbered samples are telemetered.

The samples telemetered within a single sweep will be uniformly spaced in voltage. There will be no missing 25th sample to recover in each second, as there was for the SSIES electron probe and the SSIES and SSIES-2 RPA's.

Currents: As for previous SSIES packages, the EP current is measured by a logarithmic electrometer, which, for each sample, generates a signal, in volts, that varies linearly with the logarithm of the current. TM will provide these signals, 24 per second, as unsigned 9-bit integers, negative values set to zero, LSB = 0.01 volts. In IESPREPFILE, these values will be in words 94-117 in both cycles, as was the case with SSIES-2. The raw signal in volts will be converted to log current in amps, using available calibration constants. This procedure is the same as for the previous SSIES's, except that the calibration constants will likely differ, and it is conceivable that they will be temperature dependent. In the present software, the conversion is performed in subroutine DECODE, using calibration constants read from the file IESCNTLFILE by subroutine INIT during the initialization process.

2.6.5.2 Analysis of EP Data

The analysis of the EP sweeps should be similar to what was done previously. Therefore, no modification of the EP analysis modules is anticipated at this time, with one exception. The sweep voltages will not necessarily be referenced to V_{bias} as was done previously. Therefore, this parameter, presently an input argument to the analysis module EPSWP, should be replaced by whatever reference voltage is used.

2.6.5.3 Implementation

A new driver routine, EPPRC3, has been written for SSIES-3, while the pre-existing SSIES-2 routine has been renamed EPPRC2. Each routine collects its sweeps according to the specifications given, then uses the same routine, EPSWP for the analysis.

2.6.6 Notes

The plasma density source designation ISWCKL, which is an input parameter to subroutine CKLPRC, should never be 3 in SSIES-3 processing, since the electron sensor will not be operating in the DC modes. This parameter is input to the program from the

IESCNTRLFILE, as the 12th processing control parameter. High time resolution plasma density data are used by subroutine CKLPRC to estimate the power density spectrum of irregularities in the ionospheric plasma. The other two options (1 for SM EL/AMP data, 2 for SM EL/AMP and filters) remain viable for SSIES-3.

2.6.7 Output File Format

Currently four output files are generated by APGA: IESEDRFILE, a file of one-minute environmental data records; IESMECFILE, a file containing velocities; IESAGDBXFR1, a file of one minute summary records; and IESSTAFILE, a file containing processing statistics from an APGA run. In addition, options exist to generate diagnostic output files for individual portions of the analysis, for example the files IESRPAPRT (ASCII) and IESRPADIAG (binary) may be created for diagnostics of the RPA data analysis.

2.6.7.1 IESEDRFILE

This file contains the environmental data records, the principal outputs of program APGA. Currently each EDR logical record is 595 words long (4 bytes per word) and contains the results of one minute of data. Three logical EDR records are contained in one binary direct access record of 1791 words, where the first six words are remnants of the Sperry database system that are no longer used.

Since the basic output products of APGA are not expected to change significantly, little change is anticipated in IESEDRFILE. As mentioned in the RPA discussion above, the SSIES-2 file size is retained by averaging consecutive 2-second results to obtain one 4-second result. The light ion flag has been generalized by encoding the $H^+/(H^+ + He^+)$ fraction.

Engineering data near the end of each EDR logical record has been modified to reflect SSIES-3:

- (Unused)
- MEP temperature
- Electronics (SEP) temperature
- DM offset voltage
- DM mode
- EP mode
- V_{IP}

This basically preserves the format for the previous SSIES's, as nearly as possible, while accommodating SSIES-3-specific data. In particular, the current format contains two MEP temperatures, whereas, beginning with SSIES-2, only one has actually been used. In SSIES-3 the sensor electronics package (SEP) replaces, and expands on, the SM/DM electronics package (DSM) used previously. The DM offset, DM mode, and EP mode

remain in SSIES-3, although their definition or derivations will be different. The DM offset will be determined by ground processing of the data; the DM mode should have only 3 values: slow, normal, or auto; and there should be only one EP mode. If desired, up to 7 additional parameters may be included without expanding the data record, by using the "filler words" at the end of the record. Candidates include sensor temperatures (EP, RPA, SM, DM), the SM bias, and the 12 volt monitor.

Dates, currently output using 2-digit years have been modified to include 4-digit years. This occurs in word 2 of each EDR logical record [*Cornelius and Mazzella*, 1994, Vol. III, p. 236] and in words 2 and 6 of the header record [*Cornelius and Mazzella*, 1994, Vol. II, p. 70].

Subroutine LDEDR, which builds the EDR's, is the only subroutine affected, unless there is a change in the record size, or there exists software which uses the EDR, as stored in memory, for other purposes.

2.6.7.2 IESMECFILE

This file contains the horizontal and vertical components of velocity normal to the spacecraft motion, derived from the analysis of the driftmeter data. The only change in the format is the inclusion of all 4 digits of the year in the date given in word 2 of each record.

2.6.7.3 IESAGDBFXR1

This file contains one-minute summaries derived from the EDR records. No changes are anticipated except for expressing the dates with 4-digit years. These occur in word 2 of the header and word 1 of the data records (see above reference, Vol. III, pp. 240-241).

2.6.7.4 IESSTATFILE

These contain statistics of runs: averages of geophysical parameters and instrument temperatures, processing statistics, such as number of successful analyses of each type, and error/status flags. See *Cornelius and Mazzella*, 1994, Vol. III, p. 238. No changes are contemplated for SSIES-3, except some instrument temperature parameters differing from those occurring in previous SSIES packages. No dates are included in these files.

3. CRRES ELECTROMAGNETIC FIELD DATA BASES

CRRES was launched on July 25, 1990, and traveled in a 360 km x 34000 km altitude orbit, at 18° inclination for most of its mission, which terminated on October 11, 1991. Its purpose was to make comprehensive measurements of particles and fields in the radiation belts and their effects on satellites in that environment. The radiation belts consist of energetic particles (100 keV-25 MeV electrons and 100 keV - 1 GeV protons) trapped by the earth's steady state magnetic field. Although, in a static environment, the electric field influences particles at these energies negligibly compared to the magnetic field, in a dynamic environment the fluctuations in both electric and magnetic fields strongly affect the time behavior of the trapped particle distributions. Electric and magnetic field variations at frequencies coincident with oscillation frequencies in a particle's motions resonantly alter one or more of its adiabatic invariants, the approximate constants of motion. Stochastic application of these forces results in diffusion of the particles in adiabatic invariant space.

To measure the fields, CRRES carried three instruments: a flux gate magnetometer [Singer, *et al.*, 1992], an electric field/Langmuir probe instrument [Wygant, *et al.*, 1992], and a plasma wave experiment [Anderson, *et al.*, 1992]. The electric field instrument measured the electric potential across each of two pairs of orthogonally aligned sensors, mounted in the spin plane. One pair of sensors was spherical, and the other cylindrical. The measurements of each pair were analyzed separately, producing spin plane field values at a resolution of 30 seconds, the CRRES spin period. The flux gate magnetometer contained three approximately orthogonal sensors, enabling 2-second resolution of the full magnetic field vector. The plasma wave experiment contained a search coil magnetometer, a long-wire antenna (actually the cylindrical sensor pair used by the electric field instrument), and two receivers that spectrally analyzed the data in 5.6 Hz - 10 kHz, and 100 Hz - 400 kHz, respectively.

3.1 DATA ARCHIVE

The CRRES electric and magnetic field data sets, resulting from analysis by AFRL and contractor personnel, were originally stored on a Sun workstation hard disk or on optical disks readable only on a VAX platform. These data consist of

- 30-second spin-fits of both electric and magnetic field data provided by the electric field/Langmuir probe and flux gate magnetometer, respectively. Two data sets were prepared:
 - a. A flatfile format, prepared by AFRL personnel, in which the data are sorted by orbit number, and time; all the data for one orbit were written to a single file containing time-tagged records
 - b. A variable-sorted format, in which all the data values for a particular variable,

for the entire data set, are in one file. Within each file, these were sorted by orbit number; within each orbit the data are time-ordered.

- 2 second magnetic field averages of data provided by the flux gate magnetometer, in time-ordered, flatfile format, sorted by orbit
- 8-second averages of plasma wave spectral densities at 142 frequencies over the range 0.0056 kHz - 399 kHz, from the data provided by the Plasma Wave Experiment, sorted by orbit, in time-ordered, flatfile format.

To preserve these data sets, it was necessary that they be transferred to a more stable medium, which was compatible with a multitude of hardware platforms. Therefore, the data have been written to CDROM disks in ASCII format. With the exception of the plasma wave data, which requires three disks, each data set for the entire CRRES mission can be fit, with compression, onto one 600 MB disk. The archive preserves the content organization of the data. The data are compressed and decompressed with the GNU GZIP utility, a freeware program provided by Free Software Foundation, which is available over the internet for a variety of computers and operating systems. The CDROMs contain copies of GZIP for Linux, Sun, and SGI-based UNIX systems, and for MSDOS-based computers. The compressed files are about 20% the size of the original files. A README file describes the formats of the data files and provides instructions for their decompression.

The 30 second spin-fit electric and magnetic field vectors are given in a vehicle-based non-rotating coordinate system, modified geocentric solar ecliptic (MGSE), in which: the x axis points in the spin direction, which is within 9° of the sun; the y axis is the intersection of the ecliptic and spin planes, and points toward dusk; the z axis completes the right-handed rectangular coordinate system. The MGSE x (spin axis) component of the electric field cannot be determined from the data, which includes measurements only in the spin plane. In the flatfile data base, a value is provided, based on the assumption that the electric and magnetic fields are perpendicular. The source code of a small FORTRAN program, in both DOS and UNIX versions, has been provided on the disk derived from the flatfile data set for transformation of the electric and magnetic field vectors from the MGSE coordinate system to the ECI coordinate system.

Similarly, the 2 second averaged magnetic field vectors, given on the disk in the ECI coordinate system, can be transformed to the VDH system using a program provided on the disk. In the VDH system: the z axis points along the dipole, positive North; the y axis points toward magnetic east; the x axis lies on the dipole equator, pointing vertically outward.

3.2 RADIAL DIFFUSION COEFFICIENT

Fluctuations of the electric field diffuse the distribution of charged particles in the Earth's radiation belts, a region of trapped charged particles of sufficiently high energy to degrade the performance of insufficiently shielded electronic components of earth-orbiting spacecraft. If the time varying azimuthal component of the electric field can be expressed as:

$$E_{\phi}(r_0, \phi, t) = \sum_{n=1}^N E_{\phi n}(r_0, t) \cos(n\phi + \alpha_n) \quad (9)$$

where r_0 is the radial distance, ϕ is the azimuth, measured from local midnight, and the α_n are constants, then, from the work of *Falthammar* [1965], it follows that the radial diffusion coefficient of particles trapped on the geomagnetic equator, due to time variations of the curl-free electric field (that not induced by magnetic field), is given by:

$$D_{LL}^E = \frac{1}{8 B_0^2} \sum_{n=1}^N G_n(r_0, n\Omega) \quad (10)$$

where Ω is the angular velocity in the longitudinal drift motion of the particles, B_0 is the dipole magnetic field magnitude at r_0 , the initial drift orbit radius, and G_n is the power spectral density of $E_{\phi n}$. Protons and electrons with energies 1-10 MeV in the outer radiation belt typically drift at frequencies $\Omega / 2\pi = .3 - 30$ mHz.

What *Falthammar* actually derived was an expression for the time rate of change of the mean squared radial displacement of the diffusing particles about r_0 , over times much larger than the longitudinal drift period, which he showed was equal to twice the right-hand side of Eq. (10). The diffusion coefficient is 1/2 the time rate of change of the mean square displacement, as seen, for example, from *Schulz and Lanzerotti* [1974].

A potential weakness in *Falthammar's* derivation is that he assumed the phases α_n in Eq. (9) are constant over time. *Holzworth and Mozer* [1979] assume complete randomness in the phases, expressing each term in Eq. (9) as the sum of a sin and cosine term. Then the amplitudes are independent, and they derive an expression analogous to *Falthammar's*, with the summation including the power spectra of the sin and cosine amplitudes.

Note that the radial diffusion coefficient depends on the power spectral density of fluctuations of the nodal coefficient's $E_{\phi n}$ of the azimuthal component of the electric field. Determination of the time dependence of these nodal coefficients requires simultaneous measurements of the electric field at several azimuths. A single satellite can measure only at its instantaneous location. To handle this situation, an approximation is often made, that the electric field is a pure dawn-to-dusk field, given by:

$$E_{\phi} = E_y \sin \phi \quad (11)$$

Then the summation includes only an $n=1$ term, containing the power spectral density, $P(E_y)$, of $E_{\phi 1} = E_y$. Then, from Eq. (10), we get:

$$D = \frac{P(E_y)}{8B_0^2} \quad (12)$$

3.2.1 Electric Field Data Quality Checks

There can exist conditions in which data cannot be used, due to malfunction or conditions that render the instrument temporarily inoperable, or its data not meaningful. The principal investigator of the electric field instrument [Wygant, 1996] has suggested several conditions that should be tested before using the data:

3.2.1.1 E•B Quality Check (Test 1)

Since only the spin plane components of E can be measured by the instrument, we need to estimate the spin axis component. This is commonly done by assuming that the electric field is normal to the magnetic field. Then, given the two measured components of E and the three components of B , as measured by the magnetometer, we can solve for the third component of E . Unfortunately, this requires division by the spin axis component of the magnetic field, B_x . When this is zero, we get a singularity. More generally, small values of B_x results in large uncertainty in E_x . It was recommended that the criterion to accept the data be:

$$\sqrt{(B_y/B_x)^2 + (B_z/B_x)^2} < 4 \quad (13)$$

where B_x is the spin-axis component of the magnetic field, and B_y and B_z are the components in the spin plane.

3.2.1.2 Low-altitude Measured Magnetic Field Uncertainty (Test 2)

This affects the determination of $v \times B$, which must be subtracted from the electric field in the moving spacecraft reference frame to obtain the electric field in the stationary reference frame. The uncertainty has two components. One, due to the 1-2 degree attitude uncertainty, scales as $v \times B$ and is of order 1 mV/m at $L=2$. The other component is a magnetic field measurement error of about 1% compared to the models. Assuming these errors are independent, the total error was evaluated as the square root of the sum of the squares. Data is rejected if this error exceeds the electric field magnitude in the stationary reference frame.

3.2.1.3 Biasing of Cylinder Probes (Test 3)

During most of 1990, the cylindrical probes were not properly biased. A bias parameter is included in the variable-sorted data base, mentioned above in the section on data archival.

3.2.1.4 Large Amplitude Waves Due to Precession after an Attitude Maneuver (Test 4)

Some of these are at frequencies near the drift frequencies at the particle energies of interest, 1-100 MeV.

3.2.1.5 Single Event Upsets (Test 5)

These affected the spheres, mainly in 1990, causing them to cycle between the Langmuir probe and electric field modes. In 1991, a procedure was in place to continuously monitor for SEU's, and presumably place the instrument back in the electric field mode. There is nothing we can check for here, except to note missing data. For the purpose of this test, data gaps were defined as intervals of more than 45 seconds without data in the spin-fit data base (normally the data interval is 30 seconds). It is important to note these when doing spectral analysis by the FFT method, which requires uniform spacing of data, without gaps.

3.2.1.6 Electron Injection Events (Test 6)

Energetic electron injections were capable of charging the spacecraft beyond saturation, +/- 30 V for the cylinders, +/- 100 V for the spheres. These events affected the spacecraft primarily in 1990, when its apogee was in the post midnight LT sector where these events usually occur. The charge on each sensor pair is obtained from the variable-sorted data base.

3.2.1.7 Battery Turnoff (Test 7)

This forces shut down of the instruments, resulting in large data gaps.

3.2.1.8 Electrical Short in the Spherical System (Test 8)

This causes the E-field measured by the spheres to depend slightly on plasma density and/or spacecraft potential.

3.2.2 Initial Analysis Using Flatfile-based Spin-fit Data Base

Tests 1-7 were applied to orbits 700-709, to get an idea of whether sufficiently long, uninterrupted time spans of good valid data could be found. Application of the FFT to derive the power spectrum needs at least 15 minutes of uninterrupted data to provide

~0.1 mHz of frequency resolution. The procedure is outlined in the following steps.

- 1) Extract the electric and magnetic field vectors from the archival (program BERTOBIN).
- 2) Apply test 1 to the data (program MAGCHK), appending a 32-bit flag word to each data record, with its lowest significant bit (bit 0) set to 1 if the data fail the test.
- 3) Apply test 2 to the data (program LOLERR), setting bit 1 of the flag word to 1 if the sphere data fail the test, and setting bit 2 to 1 if the cylinder data fail. The tests are slightly different for the two sensors because the results are based on comparisons of the estimate of absolute error with the magnitude of the electric field derived from the measurements of the specific sensors.
- 4) Apply test 3 to the data (program TESTBIAS), using the variable-sorted data base. All the data in this limited period passed.
- 5) With no attitude adjusts during this period, test 4 was passed by all the data.
- 6) Apply test 6, using the variable-sorted data base. All the data in this period (orbits 700-709) passed.

Tests 5 and 7 could not be carried out precisely, since the only indicators were gaps in the data base. Large gaps occurred near the end of each orbit, signifying battery turnoff. Test 8 has not been attempted, since it requires knowledge of the plasma density. This test is necessary only if the sphere data are used.

Figure 4 shows orbit 700 cylinder data that passed all tests or failed tests 1 or 2. Gaps, indicating failure of tests 5 or 7, are shown. The magnetic field is often close to the spin plane so that the energetic particle detectors whose only field of view is in the spin plane, can cover low pitch angles. The other nine orbits showed similar results. Each orbit contained at least two hours uninterrupted data passing the quality checks. Figure 5 shows the electric field components in the valid data regions. Vertical lines indicate boundaries between regions of valid and invalid data. Some very narrow regions cannot be seen since the distances between their boundaries is less than the thickness of the lines. The x-axis shows relevant magnetic coordinates along with universal time.

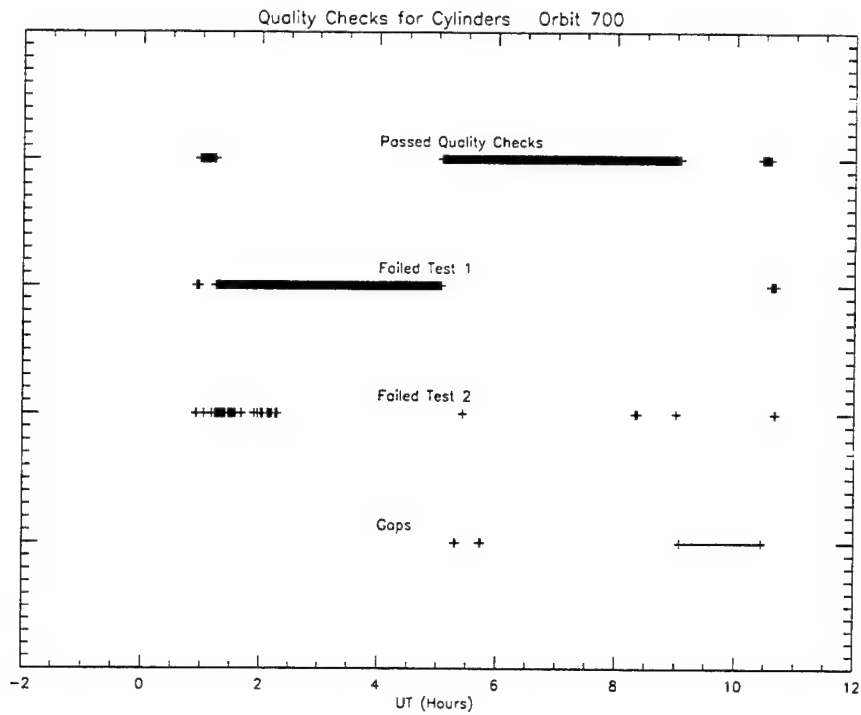


Figure 4. Quality check results for cylinder data, orbit 700.

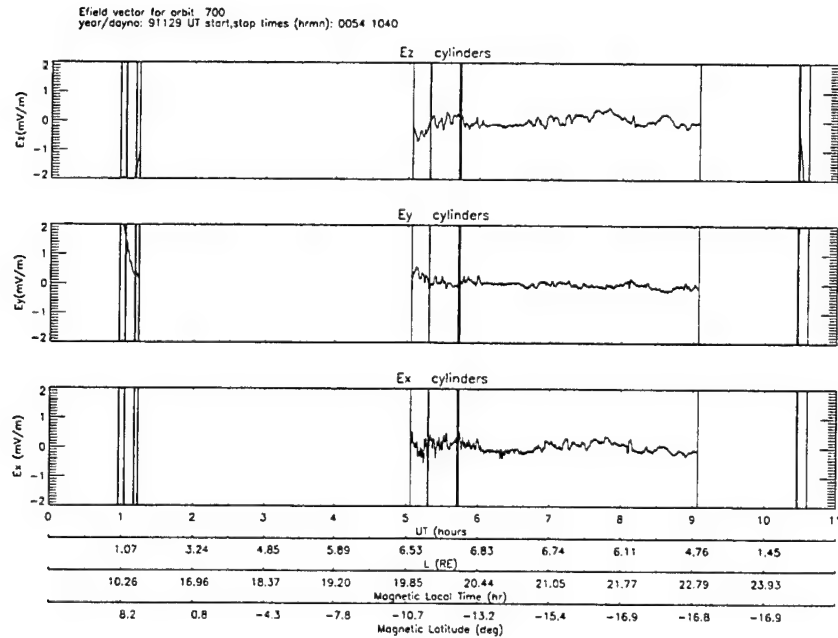


Figure 5. Valid electric field vector for orbit 700, derived from cylinder data.

3.2.3 Spectral Analysis with FFT

Software has been built that obtains power spectra using the FFT for segments of valid data on the 30-second data bases. The program searches a data file for valid data segments at least 8 points (4 minutes) long. For each such segment, the exponent n is found, such that 2^n is the highest power of 2 that does not exceed the number of points in the segment. Then a sub-segment of $N=2^n$ points is laid out, centered on the original segment. Let us call this the central sub-segment. To the left (earlier times) of the central sub-segment, additional sub-segments are laid out, the first of which, immediately adjacent to the central sub-segment, has length equal to the highest power of 2 less than or equal to the number of remaining data points to the left. We then continue successively to the left, each time creating a segment whose length is the highest power of 2 within the number of remaining data points, until the number remaining is less than the minimum (8) that we wish to consider. A similar procedure is followed to the right of the central sub-segment. Thus, we obtain a symmetrical layout in which the largest sub-segment is at the center of the original segment, and successively smaller sub-segments are found as we move away from the center. The length of each sub-segment is a power of 2. Each of these can be further subdivided into lower powers of 2 by halving, quartering, etc. Thus for each sub-segment we compute the FFT for all powers of 2 between the desired minimum (8 points ~ 4 minutes) and maximum (128 points ~ 64 minutes) that do not exceed the size of the sub-segment. For each FFT we save:

The start and end times (UT, sec.);

The frequency resolution;

The minimum maximum and average L ;

The minimum, maximum, and average magnetic local time;

The bin number, and power spectral periodogram estimates for the MGSE electric field components.

The frequency pertaining to each bin is the product of the bin number times the frequency resolution. Bin numbers run from 0 to $N/2$, where N is the number of data points. The FFT's were computed after windowing the original data with the Welch window to reduce leakage, as described by *Press, et al. [1992]*. The periodograms (FFT estimates of the power spectrum) were computed from *Press, et al. [1992]*:

$$\begin{aligned}
D_k &= \sum_{j=0}^{N-1} c_j w_j e^{2\pi i j k / N} \\
P(0) &= \frac{1}{W_{ss}} |D_0|^2 \\
P(f_k) &= \frac{1}{W_{ss}} [|D_k|^2 + |D_{N-k}|^2] \quad k = 1, 2, \dots, \left(\frac{N}{2} - 1\right) \\
P(f_c) &= \frac{1}{W_{ss}} |D_{N/2}|^2
\end{aligned} \tag{14}$$

where

$$W_{ss} = N \sum_{k=0}^{N_1} w_k^2 \tag{15}$$

To get power law spectral densities (mv²/sec²/mHz) from the periodogram estimates, we divide by the frequency resolution.

3.2.4 Analysis with Full Variable-Sorted Data Base

Recently the PI and his staff at the University of Minnesota completed a quality check of all the data in the Variable-Sorted Data Base [Rowland, 1998]. They marked each 30-second data point with a flag equal to 1 if the data point passed, 0 if it failed. Their tests included #'s 3, 4, 6, and 7, mentioned above, and an additional test that the data not be within a chemical release. Furthermore all data within 1990 automatically failed because of the frequent occurrence of undesirable conditions including lack of proper biasing of the cylinders, and a large number of electron injection events, causing saturation of the probes. The tests were applied to the cylinder data only.

We have additionally implemented test# 1, both for the original criterion and a more stringent one:

$$\sqrt{(B_y/B_x)^2 + (B_z/B_x)^2} < 2 \tag{16}$$

For this IDL-suited data base, these tests were easily implemented. For each test, new files were created containing pass/fail flags for each data point.

The original test # 2 has been replaced by requiring that L (the shell parameter) be greater than 2.75, avoiding the low-latitude region that is vulnerable to uncertainties in the magnetic field.

The original test for attitude adjusts (# 4) required that the data be at least 4 hours after the last attitude adjust. Since it takes up to one orbit for the resulting 15-20 minute unmodeled oscillations of the spacecraft to dampen down to 3° , we have extended the time wait to 10 hours after the adjust. To implement the attitude adjust tests, a file was constructed containing the attitude start and end times in days elapsed since the beginning of 1990, using program ATTADJTIMES. Then an IDL program compared the time of each data point with the times in the attitude adjust file, producing an attitude flag set to zero to indicate failure, 1 to indicate passage.

Sphere-specific tests 5 and 8 were not implemented.

We now redefine the test numbers as follows:

Test 1. Pass the Minnesota quality checks plus $L > 2.75$

Test 2. Test 1 plus original magnetic field test, Eq. (13)

Test 3. Test 1 plus the stricter magnetic field test, Eq. (15)

Test 4. Test 1 plus at least 10 hours after latest attitude adjust.

Test 5. Test 2 plus at least 10 hours after latest attitude adjust.

Test 6. Test 3 plus at least 10 hours after latest attitude adjust.

The following list shows some statistics concerning the data base size and the size of the subsets passing these tests:

Total size of data base	1074605
Number in 1991.	732665
Number accepted by Minnesota quality flags	632136
Accepted by Test 1	547731
Accepted by Test 2	364232
Accepted by Test 3	230742
Accepted by Test 4	517147
Accepted by Test 5	343509
Accepted by Test 6.	217826

Almost half the data fail test 1; 60 % of these are in 1990. Of those passing test 1, the magnetic field test is responsible for most subsequent failures.

The set of non-overlapping uninterrupted intervals was compiled for the data passing each test. Each interval is separated from adjacent intervals by at least one point of missing or invalid data (data not passing the test in question). Figures 6-11 show the frequency distribution in interval sizes, as the number of occurrences of intervals in various size bins. Each size bin is labeled by the maximum power of two contained within in the interval. Thus, bin 256, for example, encompasses those intervals of size ≥ 256 and < 512 . Each interval is tagged by its average L value. Figure 6 shows the distribution for all L , for all 6 tests, while figures 7-11 show the distributions for $L=3, 4, 5, 6$, and 7 , respectively, where each L bin is one R_E wide and centered about the given L value.

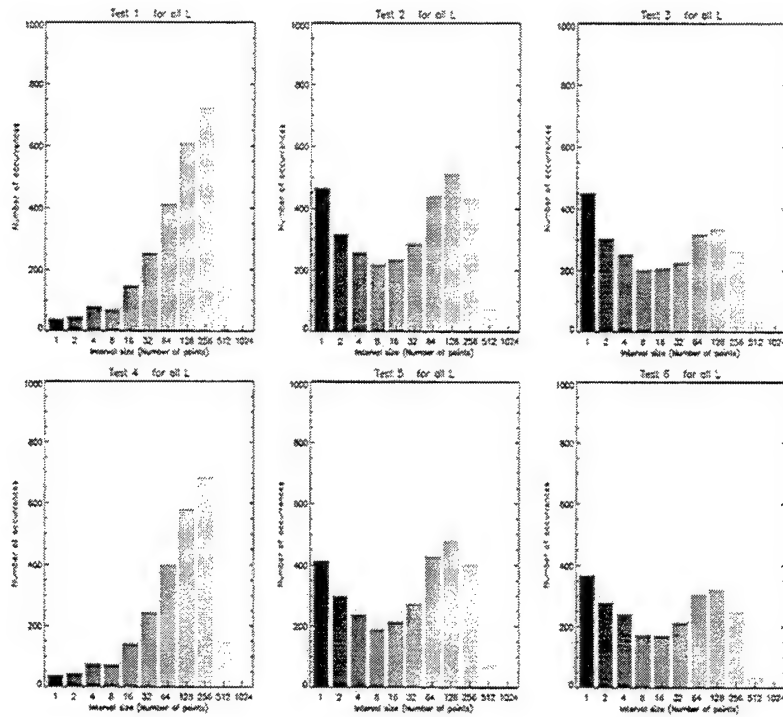


Figure 6. Size distribution of valid data intervals over electric field data base.

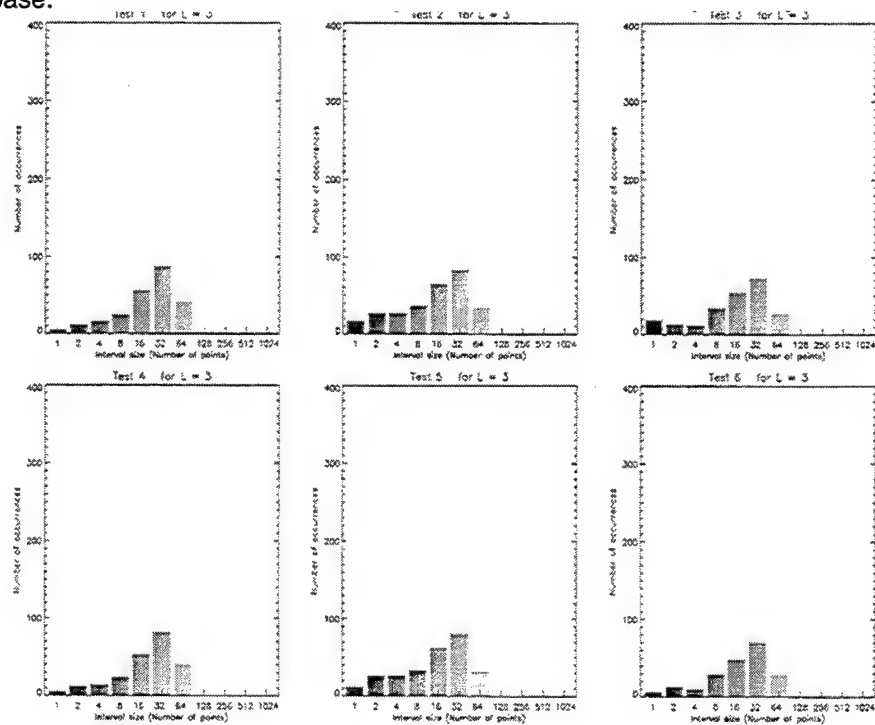


Figure 7. Size distribution of valid data intervals over electric field data base, for $L=3$.

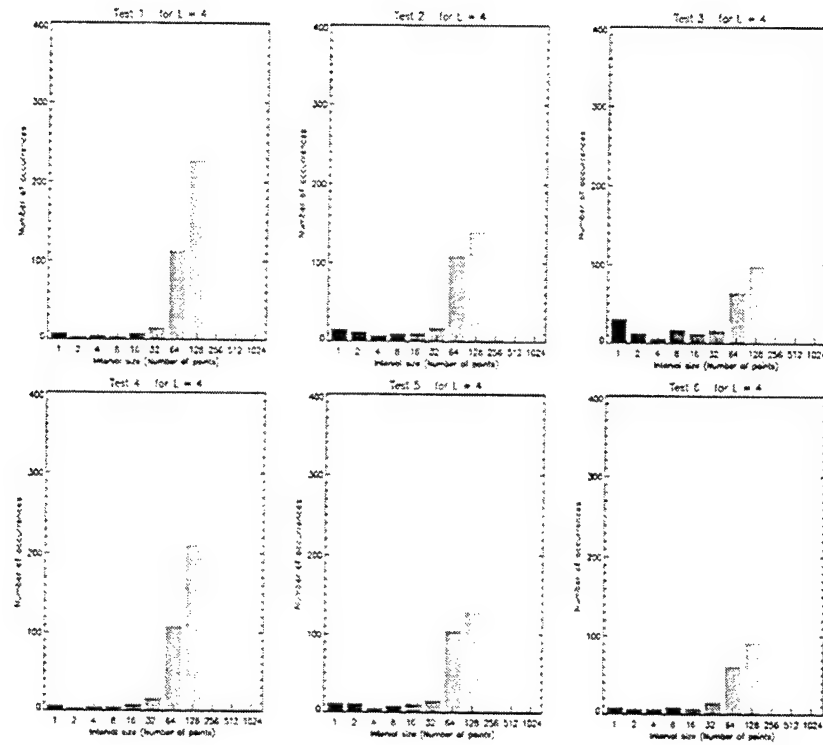


Figure 8. Size distribution of valid data intervals over electric field data base, for $L=4$.

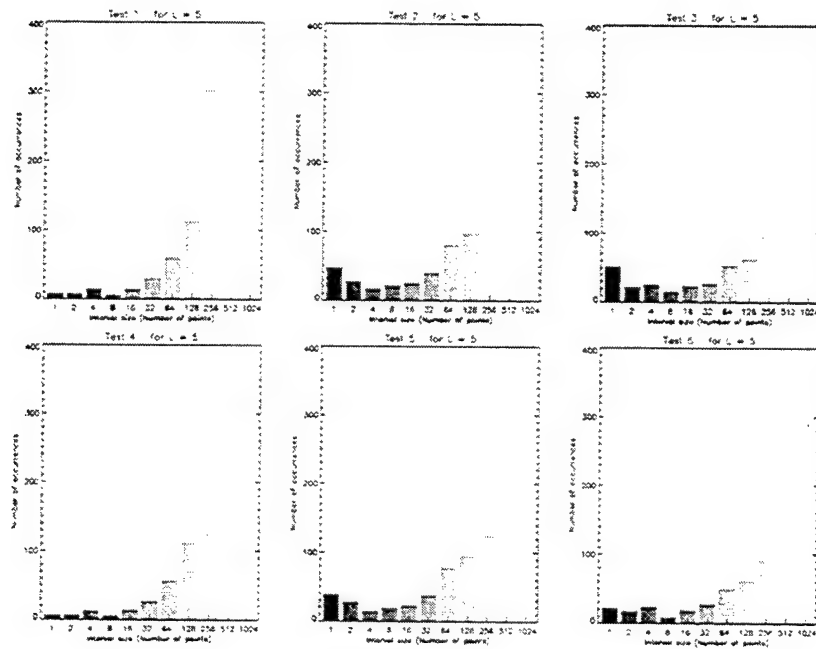


Figure 9. Size distribution of valid data intervals over electric field data base, for $L=5$.

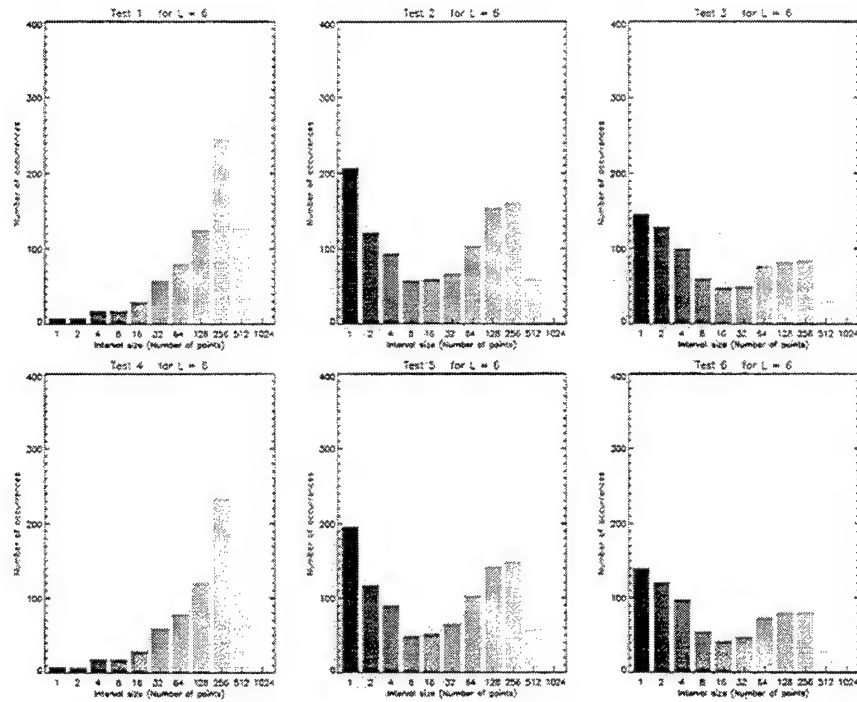


Figure 10. Size distribution of valid data intervals over electric field data base, for $L=6$.

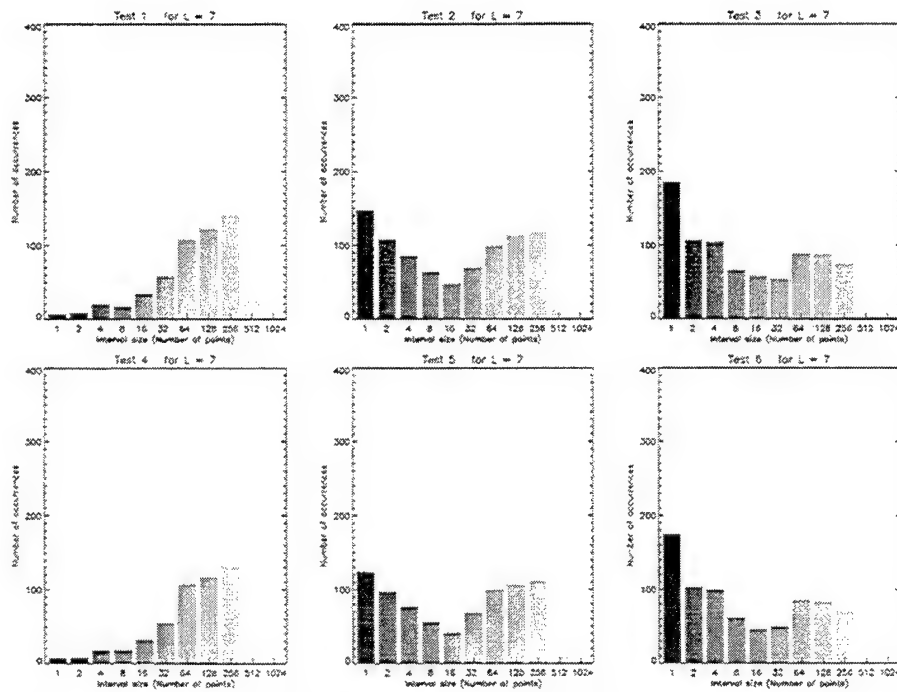


Figure 11. Size distribution of valid data intervals over electric field data base, for $L=7$.

The diffusion coefficient was computed for orbits 900-1000 in the interval $L=3-4$, for test comparison with early quick-look results generated by the principal investigator (PI) [Wygant, 1997], prior to performing the quality checks. For this test the factor $1/8$ was dropped, in conformance with the PI's definition of a "heuristic" diffusion coefficient. Note that E_y refers to the magnetic dawn to dusk component of the electric field. If we accept the argument that MGSE y direction is approximately equal to the magnetic y direction, then we can substitute the MGSE y component for magnetic y component. We then do not need to determine the full 3-component vector, allowing us to dispense with the magnetic field tests. Therefore, we selected the intervals passing the redefined test 4 given in this section, namely that each point had passed the recent quality checks imposed by the PI, was at an L value greater than 2.75, and was at least 10 hours after the most recent attitude adjust. Gap-free intervals of at least 8 consecutive valid data points were input into the FFT. For each interval the average L and B^2 were obtained, the L being used to determine whether or not the interval was in the requested L bin. Only cylinder data were used. The result at each FFT frequency was placed in a 1 mHz wide bin, which was averaged at the end of the computation.

Figure 12 shows our results for the 2.5-3.5 mHz bin, in comparison with PI's (University of Minnesota) quick-look results that had been obtained without quality checking. Considerable disparity exists, which was found to originate from the use of unqualified 64-point up-leg intervals in the PI's algorithm, compared to our use of quality-checked data, while mixing up-leg and down-leg intervals, and intervals of varying size. When we forced our intervals to be the same as Minnesota's we obtained almost matching agreement (Figure 13) in the diffusion coefficients for a given set of inputs. Some differences arise from our allowing the FFT frequencies to vary with varying spin period (25-35 sec).

The code and data base can now be applied to investigate diffusion coefficient dependencies on relevant parameters such as L and K_p . Time variations should also be examined for correlation with particle flux variations.

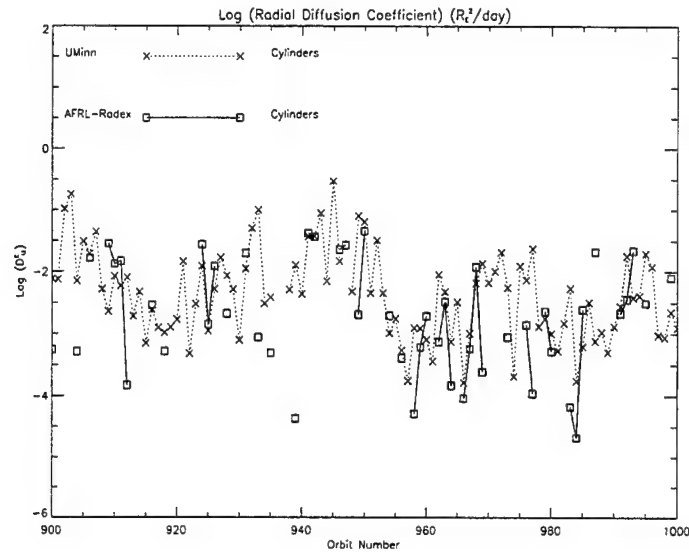


Figure 12. Radial diffusion coefficients in orbits 900-1000 computed by our program (AFRL-Radex) and the University of Minnesota program (UMinn), for $L=3-4$, for a particle longitudinal drift frequency of 3.1 mHz. The UMinn computation used 64-point intervals, in the ascending legs of the orbits, without quality checking the data. The AFRL-Radex computation used only intervals of quality-checked data, but included intervals of varying lengths, in both ascending and descending legs of the orbits. Symbols for consecutive orbits are joined.

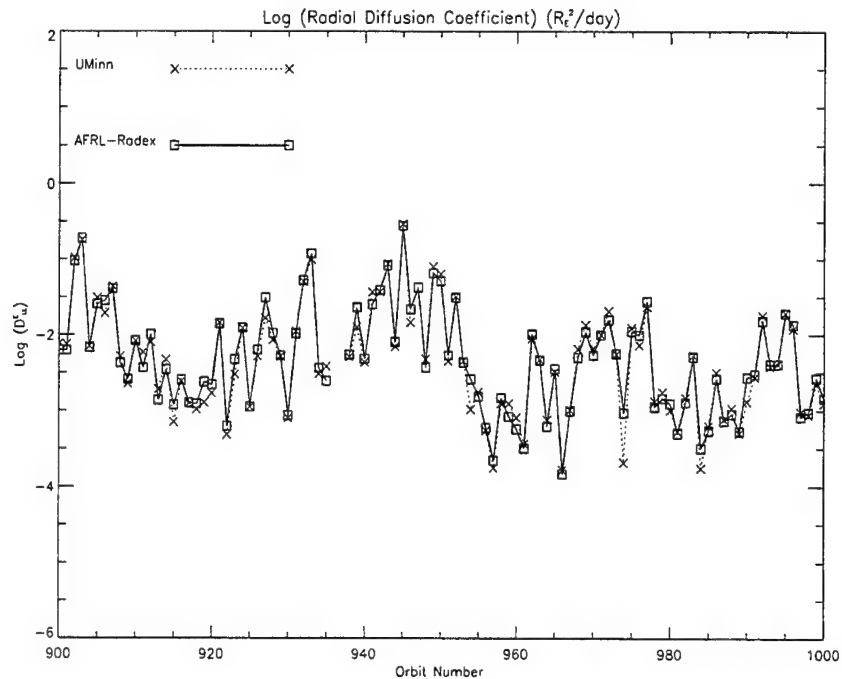


Figure 13. Similar to Figure 12, except that the AFRL-Radex computation used the same intervals as the UMinn computation, disregarding the quality checks.

4. GEOSPACE

The GEOSpace code [Ginet, *et al.*, 1999] for three-dimensional visualization of the dynamic space environment has been developed as one aspect of support for Space Weather for the Air Force. The program imports a variety of models of the near-Earth space environment, including the ionosphere, aurora, and magnetosphere, for both operational and scientific use. The code facilitates the assessment of space environmental hazards by bringing many environmental models together in a user-friendly graphics intensive program. With its 3D visualization capability and its variety of models, the code provides an effective tool for magnetostatic and ionospheric research and education. The GEOSpace program has been implemented on Silicon Graphics (SGI) workstations under UNIX operating systems (IRIX 5.x, 6.x). It uses an X/Motif widget interface and OpenGL is employed for graphics rendering. The executive system is written mainly in C++ using object-oriented concepts, while the lower level coding can be in FORTRAN or C. The program is divided into science, application, data, graphics, and worksheets modules. The current science objects are the radiation belt models (CRRESELE, CRRESPRO, CRRESRAD) [Kerns and Gussenhoven, 1992; Meffert and Gussenhoven, 1994; Gussenhoven, *et al.*, 1993; Brautigam, *et al.*, 1992], the Auroral Precipitation model [Hardy, *et al.*, 1985; 1989] with 3D extensions, the parameterized ionospheric model (PIM) [Daniell and Anderson, 1995], and the ionospheric wide-band scintillation code WBMOD [Secan and Bussey, 1994]. The application modules include orbit propagation using either LOKANGLE [Bass, *et al.*, 1976] or SPACETRACK [Hoots and Roehrich, 1980], orbit integration of the CRRES data, magnetic field models (dipole, IGRF, Olson and Pfitzer [1974], Hilmer and Voigt [1995], Tsyganenko [1989]) and specialized PIM graphics and ray tracing codes. The data module reads several Air Force Research Laboratory (AFRL) specific data formats, including electron and ion distributions from DMSP measurements [Mullen, 1996]. The graphics modules can display 1D line plots, 2D/3D coordinate slices, 2D/3D orbit plane slices, 3D isocontours, 2D/3D field line traces, and 2D/3D orbits along with satellite detector, earth and star background, and axes depictions. Graphics options, such as clipping, transparency, and various lighting modes, can be utilized to enhance the views, as well as the standard translate, rotate, and zoom manipulations. The worksheets module is provided for support calculations, such as calendar dates and various coordinate transformations.

4.1 DEVELOPMENT WORK ON GEOSPACE

As code development and system manager duties frequently overlap, many system manager duties have been done in the course of development and testing of GEOSpace. The management of the GEOSpace program on an SGI workstation entails creating, maintaining, and bringing to operation several versions of the system in a UNIX environment. The code is partitioned into a models section and a main section. The models section includes data and codes that have been imported from other sources.

These files can be compiled and run outside of GEOSpace, but in normal operation, are invoked from within the program by means of system calls. The main GEOSpace section is divided into hierarchal directories classified by function type. New coding that is written or received from outside modelers is incorporated into the code efficiently by a system of UNIX make files. The make files are also used to systematically back up the complete program, using UNIX Revision Control System (RCS) utilities. Each GEOSpace directory has a subdirectory containing RCS files that log any changes to the source files, and standard RCS commands can be used to view and update the logs or revert to old versions of the files. For run operations, UNIX scripts are provided to select the version requested, do the appropriate setup file submissions, and then submit an SGI Dynamic Shared Object (DSO) file for execution. When a version is complete and error free and is ready to be released to users, a "distribution" can be made. To create a distribution, one makes archives of all the needed GEOSpace files. This is done selectively, using UNIX scripts that pick out the required executables, data, and object libraries to be accumulated into the UNIX archiver (tar) files of the distribution package. To produce a CDROM from the tar files, we use acquired GEAR software, which reads them and writes to the PINNACLE 5040 CD-R unit. A further UNIX script is provided for reading back from the CDROM and selectively extracting the program files.

Extensive programming work has been done to develop and verify the GEOSpace program. An outline of previous efforts is given in *Ayer, et al.* [1997]. Further coding development, done during the period of this contract, is summarized below:

Development of a module representing an auroral electron background probability model (EPRM). In the EPRM module, plots of probability and average distributions for background electrons can be displayed on a 2D spherical coordinate system centered at the magnetic pole. The range of energy flux, number flux, or average energy, can be set by widgets, along with a selection of kp domains for the plots.

Development of a module representing the Parameterized Real-time Ionospheric Model (PRISM) [Daniell and Brown, 1995]. The code allows input of Digital Ionospheric Sounding System (DISS) data in either of two different formats. The GUI interface in GEOSpace written for PRISM allows user selection of Ionospheric Monitoring System (IMS) data files, as well as SSIES and SSJ4 data from the DMSP program.

Development of a module to read and depict DMSP high energy electron and proton spectra measured by the DMSP SSJ4 sensors as a function of time (DMSP-SPECTRA). The spectra can be marked to show onset and end of equatorward boundary crossings and a plot of the boundaries may be displayed.

Porting of the CRRES/SPACERAD Heavy Ion model of the environment (CHIME) [Chenette, et al., 1995] from the PC to an SGI, and development of two GEOSpace modules: a science module for viewing the source cosmic ray and solar fluxes, and

an application module, for calculating the linear energy transfer (LET) spectra and single event upset (SEU) rates for a microelectronic device.

Development of a graphics module for drawing communications links between satellites and arbitrary points on the Earth's surface. This graphics module, named COMM-LINKS, uses the results of running the orbit application module as input to its graphic drawing routines.

Development of an application module for providing additional satellite information that can be passed along to a graphics module for display purposes. The application module, SATEL-APP, makes use of a new one-dimensional gridded data set of satellite data. The new data set contains, in addition to the orbit information of the satellite, the latitude, longitude, and altitude of up to 10 stations on the Earth's surface or above, as well as the pitch, azimuth, and field-of-view angles of up to 5 detectors on the satellite.

Development of science and application modules representing the Advanced Photovoltaic and Electronics Radiation Dose Model (APEXRAD) [Bell and Gussenhoven, 1997]. The application module calculates the dosage received in a user-defined orbit. The science module reads the dose files and bins them according to user-specified conditions for display via existing PL-GEOSpace graphics modules.

The next sections will describe the PL-GEOSpace modules for PRISM, DMSP-SPECTRA, CHIME, and APEXRAD in more detail.

4.2 THE PRISM MODULE

The science module PRISM was developed to provide an interface for running PRISM Version 1.7b, the source code of which was obtained from Computational Physics Incorporated (CPI). Because PRISM has many similarities to its static cousin PIM, some changes to the PIM science module were necessary to prevent conflicts between the common input files read by the two modules. Specifically, the file PATH_NAM.TXT is common to both PIM and PRISM. This file contains pointers to various model coefficient databases used by both PIM and PRISM and additionally, for PRISM, the pointers to real-time data. Although the model coefficient databases are common to both programs, the addition of the real-time pointers makes the file unusable by PIM. To circumvent this problem, intermediate files are created which are then used to overwrite PATH_NAM.TXT, depending upon which program is selected.

Activation of the PRISM science module produces a display of options for running PRISM. A set of two toggle buttons for selecting the type of output from station sites provides the option of specifying profile parameters and/or electron density profiles, or no output at all. Another set of toggles allows the user to specify the source of effective sunspot number

(SSN). The value for this number can either be taken from DISS and IMS input or specified numerically. Effective sunspot number is ignored when the f0F2 normalization is turned off. One must choose to normalize f0F2 to the URSI-88 coefficients for the effective SSN to be meaningful. Consequently, the widgets for selecting effective SSN are inactive when effective SSN has no significance in PRISM running conditions.

An option menu for selecting the F10.7/SSN relationship provides three choices: 1) SSN is to be computed from F10.7; 2) F10.7 is to be computed from SSN; 3) SSN and F10.7 are unrelated. It should be noted that the decoupled relationship is strongly recommended by CPI. Three text field widgets enable the user to input values for the y and z components of the interplanetary magnetic field, as well as the 90 day mean F10.7 value, as used by the MSIS model. The results of the PRISM run will be saved into the file named in the output file text widget.

The real-time data input option is controlled by three sets of widgets for the DISS, DMSP, and IMS data. Each widget set contains a pushbutton and a text widget. The text widget contains the name of the file that will be used as input to PRISM for the type of data signified by the name on the adjacent pushbutton. Pressing the pushbutton allows the user to modify the contents of the data or create a new data file. Activating the pushbutton causes a new window to be displayed showing the real-time data files available for the selected category. For DISS data, the files listed are either in a format specified by the University of Massachusetts at Lowell or in a format used by NGDC. For DMSP data, both SSIES and SSJ4 data can be chosen. Data files listed can be filtered on day/year, station, satellite, and parameter values, for whatever is relevant to the type of data. Activating the double "greater than" button causes all selected files in the available data files list to appear in the selected data files list. Activating the double "less than" button removes files from the selected list. Once the desired data files have been chosen, the user clicks the "OK" button, which causes a single data file to be created containing data from all of the files in the selected data files list. The created file is in a format that PRISM is able to read, and named according to the text shown in the output file text widget.

Selecting the "View Data" button allows the user to see the actual data contained in the files. The data is displayed for the day specified by the value of the scale widget labeled "Day" and for the year specified by the year shown in the text widget labeled "Year". Table 6 lists the key data elements displayed when the user clicks on the "View Data" button.

TABLE 6. Parameters Describing Real-time Data Input to PRISM			
DATA TYPE	PARAM.	UNITS	DESCRIPTION
DISS	F0F2	MHz	Observed critical frequency of the F2 layer
	HMF2	km	Observed height of the F2 layer
	F0F1	MHz	Observed critical frequency of the F1 layer
	HMF1	km	Observed height of the F1 layer
	F0E	MHz	Observed critical frequency of the E layer
	HME	km	Observed height of the E layer
IMS	GLON	degrees	Geographic longitude of ionospheric penetration point (IPP)
	GLAT	degrees	Geographic latitude of IPP
	TEC	TEC	Vertical equivalent TEC obtained from slant TEC and assigned to IPP
DMSP (SSIES)	ALT	km	Altitude of spacecraft
	ETEMP	K	In situ electron temperature
	EDEN	/cm**3	In situ electron density
	ITEMP	K	In situ ion temperature
	VV	m/s	Vertical ion drift velocity in instrument coordinates
	VH	m/s	Horizontal ion drift velocity in instrument coordinates
	O_frac	N/A	Fraction of ions that are O+
	He_frac	N/A	Fraction of ions that are He+
DMSP (SSJ4)	H_frac	N/A	Fraction of ions that are H+
	GLAT	degrees	Geographic latitude of spacecraft field line at 110 km
	GLON	degrees	Geographic longitude of spacecraft field line at 110 km
	EAVG-ELE	keV	Mean electron energy
	EFLUX-ELE	erg/s-cm**2	Energy flux of electrons
	EAVG-ION	keV	Mean ion energy
	EFLUX-ION	erg/s-cm**2	Energy flux of protons

After coding of the PRISM/GEOSpace interface was completed, a test was made to verify the DISS component of the PRISM module. Using data from the NGDC website, an attempt was made to duplicate data obtained from CPI by feeding the NGDC data to the new code. Although there were some differences in the resulting output, most likely attributable to differences in the processing of the raw data by the two organizations, the CPI data was reproduced to within probable uncertainties of the measurements. More work in the area of validating PRISM remains to be done which will no doubt require some modifications of the PRISM/GEOSpace interface.

4.3 THE DMSP-SPECTRA MODULE

A DMSP-SPECTRA module has been formed and is installed in GEOSpace. The information below, based on the code on-line help documentation, summarizes its capabilities.

4.3.1 DMSP-SPECTRA Overview

The DMSP-SPECTRA data module provides the capability to display electron and ion energy spectra measured by the DMSP SSJ4 sensors as a function of time. The current version allows the user to choose a DMSP "case" file which contains a data source file created for a specific DMSP satellite orbit, and information on estimated equatorward boundaries for event onsets and endings observed during the orbit. There is also an automatic mode which checks the source directory for recent data and, if found, updates the plots.

4.3.2 DMSP-SPECTRA Inputs

To initiate the DMSP-SPECTRA module from the DMSP-SPECTRA Options Window, the user must click on the Run Model button at the bottom of the window. A new window will appear giving a file selection widget for choosing an input data file. The default directory should list the available case files which are automatically written to the GEOSpace directories after each DMSP pass data transmission.

The case files have names of the form: case_YY_DDD_TTTTT_NNNN, where

YY= Year DDD= Day of year (1 = 1 Jan, 365 = 31 Dec)

TTTTT= UT start time of the orbit in seconds

NNNN= DMSP satellite ID

To generate a spectra plot and associated listing of events, pick a case file and press the OK button. The DMSP-SPECTRA module will execute and create both a Special Plot window displaying the energy spectra, and a text window displaying information on equatorward boundary crossings observed during the orbit.

The user can select the following plotting options by clicking on the Plot Options button in the DMSP-SPECTRA Options window:

Data Type: The user selects as either raw counts or flux.

Species: The user selects either ions or electrons.

Scale is: This toggle converts between a linear and log (base 10) representation of the data. The "AUTO" button sets the min and max from the measured data. Data at or above the upper limit is colored white. Data at or below the lower limit is colored gray. No data is colored black. For the log scale, zeros are converted to the lower limit and negative numbers are treated as no data.

Input file: The source file name message may be toggled on or off. The name is of the form avej4_NNNN_RRRRRR.cnts where NNNN is the DMSP satellite ID and RRRRRR is the Readout orbit number (the higher the orbit number, the more recent the data).

Counts Min, Max, Tics: The data limits and the number of tics can be set here. There are separate limit scales for counts and flux, due to the wide differences in range. The AUTO button shows the maximum range from the data file.

X axis: This widget may be used to set the displayed X axis variable to one of the button parameters, i.e. universal time (UT) in seconds, latitude (Lat), longitude (Lon), universal time in hours:minutes:seconds (HMS), or data record numbers. The basic variable is the data record number from which all the other variables are determined. The Marks button toggles on and off the event markers on the plot.

X UT Min, Max, Tics: The range of universal time (UT) and number of tics to plot are set here. The ALL button shows the maximum range obtained from the data file. A UT range of 6400 seconds (~106 min) is plotted by default.

Y axis: This widget may be used to set the displayed Y axis variable to either the energy channel number or the energy value (in keV) corresponding to the channel. The energy channel number is the basic variable. The ALL button resets to the widest range.

Y Bins Min, Max: This parameter may be used to select the channel limits for the plot.

Plot Update: The last generated or selected plot may be updated with this button after a change is made to the plot options.

The following options are also accessible from buttons in the DMSP-SPECTRA Options window:

Display Plot: Brings up the DMSP-SPECTRA Special Plot window if it has been closed.

Display Text: Brings up the DMSP-SPECTRA text window if it has been closed.

AUTO MODE: Puts DMSP-SPECTRA into an automatic checking mode. When in this mode, DMSP-SPECTRA looks in the directory just above the case directory. If it finds a "check_file" signaling new data, it reads and plots the spectra, erases the check_file, and waits for the arrival of the next check_file. To exit from the AUTO MODE, type "i" in the wait window.

Note: The data directory is set by the environment variable PLGS_BCSPECTRA_DATADIR.

4.3.3 DMSP-SPECTRA Outputs

The DMSP-SPECTRA module creates both a Special Plot window displaying the energy spectra and a text window displaying information on equatorward boundary crossings observed during the orbit. In the Special Plot window, the species (electrons or ions), output mode (counts or flux), year, day, and UT range is shown. Below this is a 2D color intensity plot of the count rate or flux as a function of energy (or energy channel number) and UT (or any of the other X variable options, i.e. Lat, Long, Recs). The vertical black lines give the location of the equatorward boundaries with the associated numbers corresponding to the estimated quality flag (1 is highest).

The text window shows case file information on the estimated equatorward boundaries for the event. Listed are an event counter, UT, magnetic longitude and latitude, and estimated Kp. The Qe variable is calculated from estimated Kp by the formula $Qe = 2 * Kp - 0.35$. The flag variable gives an estimate of the quality of the event (1 is highest).

In addition to the plots and text output, the DMSP-SPECTRA module creates, for each equatorward boundary found, the corresponding global equatorward boundary curve using the algorithm contained in the Aurora Science Module. This curve is saved as a Field Line Gridded Data Set which can be viewed with GEOSpace graphics modules.

4.4 THE CHIME MODULE

We are currently working on a GEOSpace representation of the Heavy Ion Model of the Environment (CHIME) for calculating single particle upsets of on board electronic chips for vehicles in near-earth space. The code produces a linear energy transfer spectrum for the flux of all particles incident on the chip material, and then calculates the SEU rate depending on the device cross-section and thickness. This model was originally developed by Lockheed Martin for the PC. The code has been transported to an SGI workstation and converted from an interactive to a batch mode version, in order to interface with GEOSpace. The SGI version of the code has been successfully tested against numerous example files from the original PC distribution. This batch version of CHIME has been subsequently incorporated into the GEOSpace program as both a science module and an application module.

4.4.1 The CHIME Science Module

The CHIME widget reads in source cosmic ray flux data from local interstellar spectra (LIS) defined at the outer boundary of the heliosphere via a solar modulation level, or

alternatively by specifying a time period. In addition, heavy ions from the sun, caused by solar energetic particle events (SEP) can be input. The SEP models are based on measurements made during the CRRES mission (including the March and June 1991 events) and on statistical distributions of energetic solar proton event intensities. The GEOSpace science module runs only that section of the CHIME program that reads in the cosmic ray and solar flare data and writes out tables of flux files (the LET spectra and SEU calculation code have been bypassed). GEOSpace loops over a 3D spherical grid space, executing CHIME at each point and reading in the flux tables, to generate a 3D data set of geometrically shielded flux values. This 3D data set can then be manipulated with the GEOSpace visualization tools. The CHIME module widget allows one to choose the energy and atomic number ranges for the plots. The anomalous cosmic ray fluxes exist as a separate viewing option, in accordance with the standard CHIME flux output.

4.4.2 The CHIME Application Module

The application module has similar options for selecting the source environment (cosmic ray or solar flares fluxes). A recent enhancement to this model has been to incorporate the CRRES PRO proton radiation belt flux, already available to GEOSpace in another module, into the CHIME system. In the application module, the full CHIME calculation of LET spectra and SEU rates are done. The application module widget allows one to choose the location of the space vehicle (fixed position in the magnetosphere or an orbit through it) and for specifying the on-board SEU device (a set of device parameters or a device cross-section file). Other widgets enable one to control the shielding thickness around the device and the resolution of the LET calculations. The CRRES PRO protons were added by inserting a routine to integrate the CRRES PRO proton flux between energy limits already calculated by CHIME for the cosmic ray protons, thus making minimal changes to the original code. When a vehicle orbit is specified, the code calculates the CRRES PRO flux spectra at each point and accumulates the data for an orbit-averaged result. The CRRES PRO LET spectra are determined separately from the cosmic ray and solar fluxes, and then added at the end to the geometrically unshielded and shielded results to create "worst/best" case rates. The standard CHIME output summaries can be displayed in a text window showing the SEU rate or LET spectra. The LET spectrum can also be displayed in a special 1D line plot. A CHIME vehicle orbit can be read in and shown in a regular GEOSpace 3D window.

4.5 THE APEX RAD MODULE

The APEX RAD application module is a UNIX version of the PC program APEX RAD developed at the Air Force Research Laboratory at Hanscom AFB. It uses empirical models based on data collected by the APEX satellite dosimeter to predict the amount of radiation expected at a particular orbit. The orbit is specified in the same manner as the ORBIT-APP application module with the additional option of selecting solar elements when specifying the orbital elements. Solar elements determine the orbit of a satellite using the

following parameters: inclination, the altitudes of apogee and perigee, and the local times of apogee and maximum inclination. These elements are primarily of interest to people who think in terms of the sun's location with respect to the satellite orbit.

Once the orbital elements have been chosen, the user clicks the "Run Model" button which starts the calculation of the dosage for the orbit. A series of four programs is run in succession to complete the calculation. The first program, LOKANGLE, reads the orbital elements file for the specified orbit and creates an ephemeris file. This file is then read in by MAGMODEL which converts the data from geographic coordinates into magnetospheric coordinates. It should be noted that this version of MAGMODEL differs from the version used with CRRESRAD in that the IGRF95 magnetic field model is used. The resulting magnetospheric ephemeris data are then input to TIMEBINS, which calculates the amount of time spent in each bin of the APEXRAD dose model for the orbit chosen. Finally, the dose for the time period of the orbit is tallied via the program DOSEDATA based upon the output of TIMEBINS and the dose rate for each bin as listed in the dosage data files.

When APEXRAD concludes its computations, a new window is opened on the screen displaying the results. The particulars of the orbit are shown at the top followed by tables listing the average dose per year as predicted by the model. Below each dosage is the percentage of the time of the orbit that was spent outside the range covered by the model. The rows of the table specify the activity levels while the columns designate the hemispheres of aluminum shielding for which the dosage listed refers. The attributes of the dosimeter are detailed at the bottom of the screen.

The APEXRAD science module provides the user the capability of mapping the radiation dose rate data from the APEX dosimeter onto a user-defined grid of points in space. Input to the module is supplied via 4 option menu widgets. These menus allow a choice of 5 magnetic field models, 4 hemisphere shielding thicknesses, 3 energy channels, and 6 activity levels. The magnetic field models available include the International Geomagnetic Reference Field (IGRF85) with or without the Olsen-Pfitzer static model, and 3 variations of dipole field. The hemisphere shielding thickness is chosen from among the four thicknesses used in the dosimeter, namely 4.29, 82.5, 232.5, and 457.5mil. The energy channels available are LOLET, for particles depositing 0.05-1.0MeV of energy, HILET (1-10MeV), and TOTAL (0.05-10MeV). The activity levels can be either for the entire mission or for 5 different ranges of the Ap index.

After running the APEXRAD science module, the dosage, L, and B/B0 values can be displayed via the graphics module. Figure 14 shows the dosage for the the following case: B-Model: IGRF85/O-P; Hemisphere: 82.5mil; Channel: TOTAL; Activity: Whole Mission. Also shown is the CRRESRAD results for a similar case. As can be seen from the figure, the APEXRAD results extend the CRRESRAD model to lower altitudes and cover a greater range in latitude.

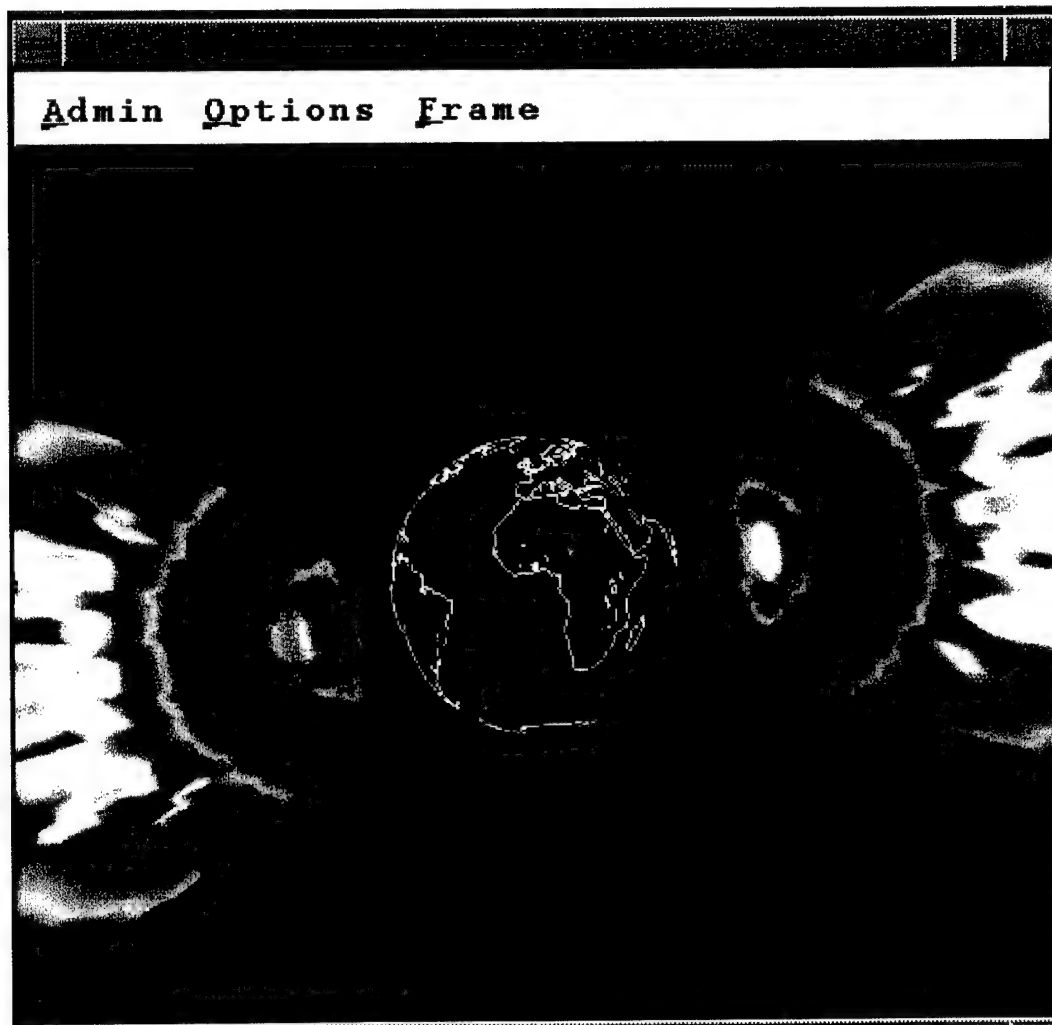


Figure 14. The dosage for the APEXRAD and CRRESRAD modules.

4.6 CONCLUSION

The GEOSpace program provides a convenient package for running near space environment models from AFRL and collaborators on a common UNIX platform with a user-friendly graphics interface emphasizing 3D visualization and animation. It gives easy access to the models and provides common application and 3D visualization tools. Because of the intrinsic 3D nature and time variation of the space environment, effective use of the models requires the capability to display multiple data sets, change the view quickly, and update the models in time. These capabilities are provided by GEOSpace, which fills the gap between space environment models scattered throughout the space community and working space system operators who desire a quick and complete description in the shortest possible time. We will continue to expand and enhance the GEOSpace program and to develop its capabilities to meet evolving user needs.

5. AIR COMBAT TARGET-ELECTRO OPTICAL SIMULATION (ACT-EOS)

5.1 INFRARED TARGET SCENE SIMULATION (IRTSS) DEVELOPMENT

The Infrared Target Scene Simulation (IRTSS) software manages large geographic datasets, supports multiple users and needs significant computer power to run its physics models. To this end a distributed system that communicates using UNIX socket facilities was designed. Several concepts drove the design. Multi-user support, multi-host scalability and ease of maintenance were the key issues.

A TCP/IP protocol driven architecture was designed to allow for distributed processing and data-storage capabilities. Invisible to the user, the IRTSS web server (back-end) allows numerous user-invoked CGI binaries to communicate with a single server capable of managing IRTSS software execution across multiple machines and platforms. A system concept diagram is shown in Figure 15.

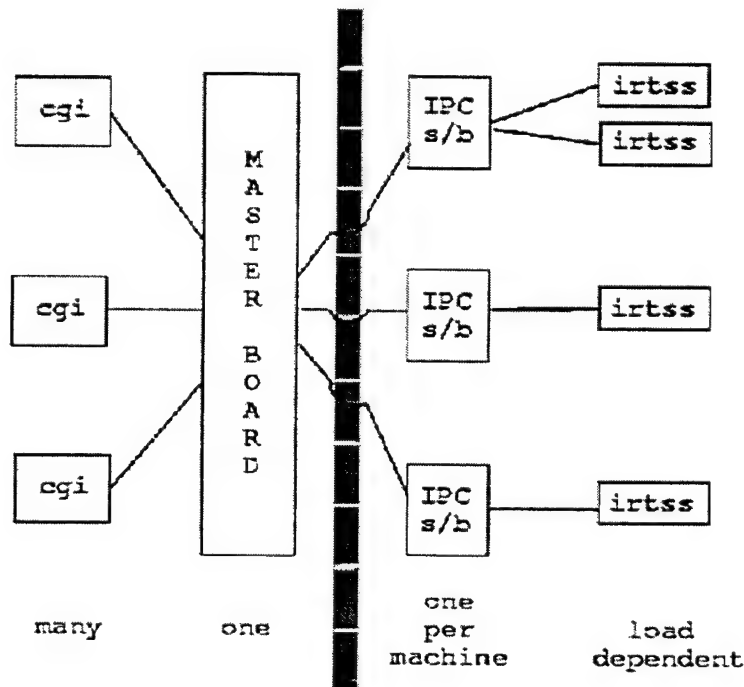


Figure 15. IRTSS system concept design.

The master board layer supports multi-user, multi-host operations. A notion of user id and host is used in the system to start different instances of the software on different hosts. The master board layer communicates with the CGI binaries invoked by the web server daemon that the user's browser interacts with. The switchboard (s/b) layer manages communication with each distributed instance of the IRTSS software on different hosts.

The net result of the various communications layers operating with a http daemon is scalable support of multiple users running computationally intensive processes from commercial web browser technology.

The crux of the IRTSS web server is the minimization of the variety of tasks that each machine must perform. High-load tasks such as IRTSS rendering are limited to one or two simultaneous processes per machine. Light-load tasks, such as managing communications between CGI binaries and processing machines, easily all take place on one machine. Transmission of communication packets between a running IRTSS process and the user CGI processes consume minimal system resources and are co-located with IRTSS processes. For each of these segments of the web server architecture, a stand-alone software package was designed.

The "master-board" is the central switching station for communications management. This software resides on the machine at which user web-browsers point. The master-board keeps a table of all software available within the architecture and the machines upon which it resides, the current load on each machine, and the status of each software process.

CGI binaries pass user requests to the master-board, and the master-board passes these messages to a specific switchboard that relays the message to the running IRTSS process. Any message returned from the IRTSS process -- such as error-checking results -- flows back from the switchboard to the master-board, which then communicates directly with the appropriate user CGI binary.

The switchboards run on any machine that executes an IRTSS process. One switchboard process is required per machine. Its role is to passively exchange messages between the master-board and an IRTSS process. Any information necessary to distinguish between specific IRTSS processes is contained in the message itself. Therefore, these machines can be described as software "slaves."

An important concept behind this architecture is that switchboards can be installed anywhere with internet access, not necessarily in the same location as the master-board or other switchboards. The only stipulation is that the master-board has an updated table of each switchboard's internet address and its IRTSS executables.

Communications are based upon TCP/IP, connected-service stream socket, client-server protocols. CGI-binaries act as clients to the master-board, which is server to both CGIs and switchboards. The switchboards are clients to the master-board and server to IRTSS processes. Finally, an IRTSS process is a client to its switchboard.

The IRTSS communications software infrastructure has proven to be a useful tool in constructing demonstrations and has supported flight test operations at both Eglin AFB, FL and Fallon NAS, NV. The ability to control the IRTSS software over the World Wide Web has enabled geographically distributed users to access newly developed Infrared Scene prediction technology.

5.2 MASTER ENVIRONMENTAL LIBRARY DEVELOPMENT

In cooperation with DMSO's Naval Research Laboratory-developed Master Environmental Library (MEL), a World Wide Web-based distributed, searchable environmental data retrieval system, one of the MEL's first product generators was developed. Product generators are data products derived from other data, typically through software vehicles such as a mesoscale model (the Navy's Coupled Oceanographic and Atmospheric Mesoscale Prediction System (COAMPS) is one) forecast run on the CSSM.

The AFRL product generator was built into the on-site MEL Resource Site that we installed and maintain. The product generator is an outgrowth of the MEL Resource Site Software, a suite of Perl scripts that process data requests from the MEL Main Access Site at NRL in Monterey, CA. The RSS services data product orders via a hypertext transport protocol (http) daemon on a UNIX server.

The product generator exemplifies the strengths of the distributed computing paradigm by pulling together data-retrieval and computing resources from a variety of locations to produce one complex product for delivery to a customer anywhere internet access is available (see Figure 16).

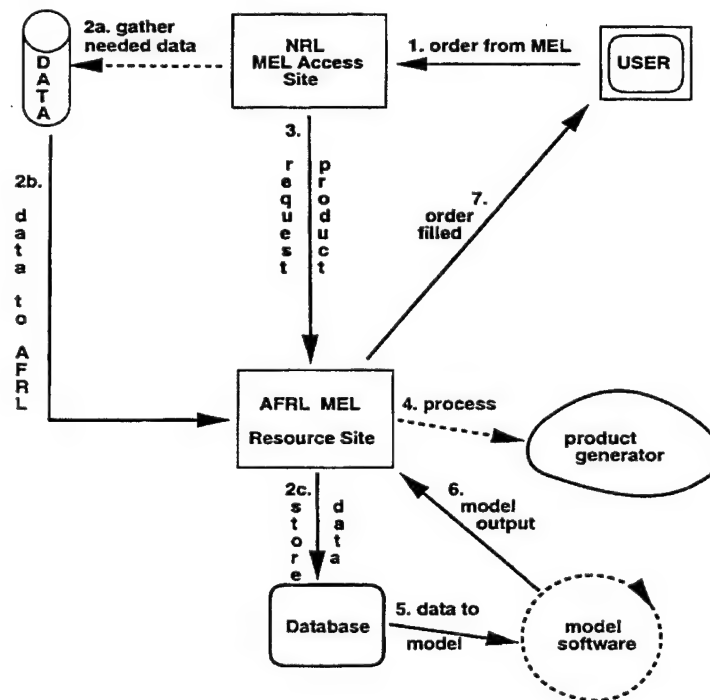


Figure 16. MEL product generator.

The AFRL MEL Resource Site acquires COAMPS meteorological data from the MEL through standard internet protocols. The product generator then decodes this data, and incorporates the data into a DIS-compliant database. This database contains other related AFRL data products such as imagery or diagnostics, and can then be used by a variety of customers as inputs to off-site weather-model software or as input to AFRL models that produce a higher-order dataset that a MEL customer can order.

This Resource Site product generator has been used to support radiometric validation research at ARL White Sands, and distributed USAF War Game Exercises that require weather effects as part of a simulation.

5.3 RADIOMETRIC VALIDATION OF CSSM

Clouds have a strong impact on many DoD missions. There is a need for physically accurate synthetic cloud environments for system design as well as for modeling and simulation of military operations. The PL sponsored Cloud Scene Simulation Model, CSSM [Cianciolo, et al., 1996] is a fractal cloud model that can generate 3-dimensional cloud liquid water content fields and evolve these fields in time. The model does not perform detailed physics calculations, as first principles cloud field generation requires extraordinary amounts of computation. The model's fractal algorithms have been tuned via visual inspection of resulting clouds and from analysis of aircraft based liquid water content data. The fields generated from CSSM can be used as input to radiative transfer schemes and scene rendering software to generate specific cloud scenes. Two kinds of field validation are needed to ensure that the cloud effects are being treated appropriately. The first type is validation of the spatial properties of the generated clouds. The second phase of validating a cloud simulation capability involves comparison of the radiative transfer methods used to generate a cloud scene with real world data.

Many experimental studies of cloud spatial structure try to access the smallest spatial scales that their instrumentation will permit. Many of these instruments are flown aboard aircraft, an expensive process that severely limits the number of cloud fields that can be probed. Satellite imagery provides another means to measure high altitude structure. Overhead views do not provide a direct means of quantifying the surface situation, especially in overcast conditions. Here we propose a method to measure cloud structure over length scales of about 3 to 30 km using inexpensive and simple pyranometer measurements.

A pyranometer measures the visible band energy reaching a point on the ground. Analysis of pyranometer time series can reveal a considerable amount about cloud cover. Assuming relatively constant wind speed and optically thick clouds the signal observed at a pyranometer should closely reflect the spatial characteristics of the clouds passing between the instrument and the sun.

Spectral analysis of the pyranometer data is one way to characterize this complex time

domain signal. Spectral analysis has several shortcomings, the most disturbing of which is that very different time domain signals can have similar frequency spectra [Marshak, et al., 1997]. On the other hand, spectral analysis of the pyranometer signal is straightforward to perform and provides a quantitative if limited way to compare synthetic and real spatial structure. It is unlikely that two processes whose spatial power spectra are significantly different are substantially similar.

Spectral analysis has been used on several different sources of cloud data, ranging from satellite imagery to in-situ hot-wire probe measurements [Marshak, et al., 1996]. A result confirmed in several studies shows power law decay of spatial fluctuations in Fourier space as: $E(k) \propto k^\beta$, where k is the spatial wave number. These studies have observed a power law spectrum over length scales of 0.5 to about 20 km. At either end of this range the spectrum is no longer a power law. Both in-situ aircraft and satellite measurements report beta to be in the range from -1.4 to -2.0. The well known theoretical Kolmogorov result for 3-dimensional turbulent flow gives beta a value of -5/3. This universal result provides a benchmark value to compare our results to.

The Air Combat Targeting Electro Optical Simulation (ACT-EOS) experiment site at Hanscom AFB has collected approximately week long pyranometer time series for several years at one minute resolution. This data set covers all four seasons and many weather conditions. We use this dataset, which includes radar and other measurements, as our primary source. Figure 17 shows raw pyranometer data for one diurnal cycle. Cloud signatures are clearly visible in the data. Subtraction of the characteristic cosine of solar elevation angle curve for the given day and location yields a cloud forcing signal at the surface. The top panel of Figure 18 shows a spectral analysis of the pyranometer cloud forcing signal with a β of -1.64. The pyranometer power spectrum appears to be a reasonable power law for most of its length. Our measurements can access time scales from 10^{-3} to 0.5 cy/minute. This translates into length scales of 3.6 km to 500 km assuming a 30 m/s wind speed at cloud height.

During the experiment there was an upward looking 35Ghz TPQ-11 cloud radar located ~0.25 km away from the pyranometer. This radar is capable of showing cloud structure up to 60,000 feet or so. By vertically integrating the raw reflectivity from the radar we are able to get another indicator of the time and space variation of the cloud structure moving over the site. The middle panel of Figure 18 shows a spectral analysis of the radar signal for the same time period as the previous pyranometer plot. The radar β is -1.52, very close to the pyranometer and not too far from the Kolmogorov result.

As an additional probe of cloud structure we retrieved visible AVHRR imagery for the New England area during the same experimental time period. The lower curve in the bottom panel of Figure 18 shows a spectral analysis of this imagery with a β of -1.73. The upper curve shows a spectral analysis of a stratocumulus cloud scene generated using the CSSM. The CSSM spectrum shows a β of -1.48, fairly close to the observed spectra. This CSSM run was not tuned to the specific atmospheric state for the observed day. It is possible that this could change the spectral exponent slightly.

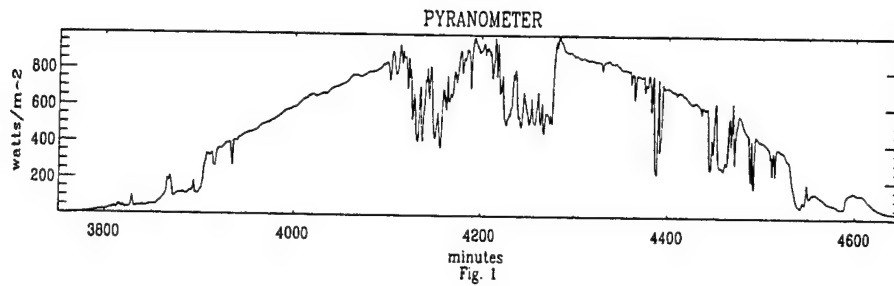


Figure 17. Raw pyranometer data for one diurnal cycle.

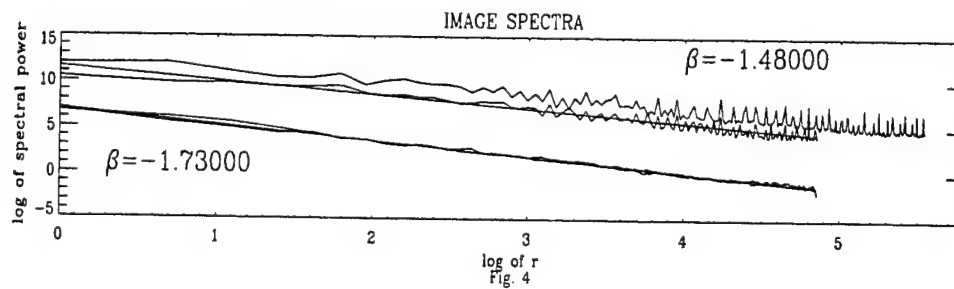
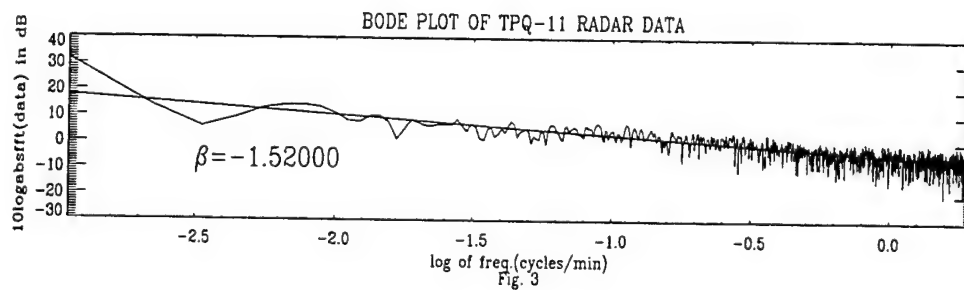
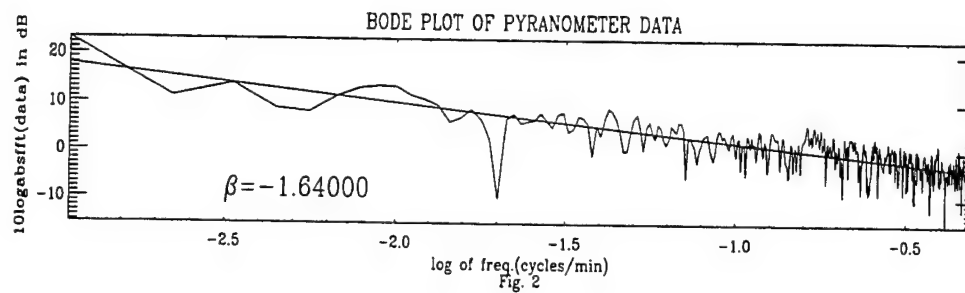


Figure 18. Spectral analyses of the cloud forcing signal.

After examining the pyranometer data for several experiments we find spectral exponents that fall in the range of about -1.4 to -2.4. These results show a generally steeper falloff than those quoted in *Marshak, et al.* [1996], who observe exponents of about -1.4 in their analysis of marine stratocumulus during FIRE and ASTEX. The pyranometer dataset used is much larger and encompasses many more cloud types than the 5 airplane flights used by Davis, therefore it is not too surprising that our results show more variability.

Simple ground based pyranometer measurements can provide information on cloud field spatial structure. This is confirmed by both ground and space based sources. Clearly the analysis presented here ignores much radiative transfer physics. However when cloud cover is broken and wind reasonably steady the pyranometer can access spatial cloud information. Spectral exponents are only one metric to compare spatial structure, however the nearly identical values from three different remote sensing methods are quite interesting. Investigation of how the method performs in overcast conditions are needed. It is expected that significant differences between radar and pyranometer measurements will be observed.

In the process of radiometrically validating a cloud scene simulation capability, spectral exponents are only one limited metric to use. Another approach is to compare 2-dimensional images generated synthetically with those observed in field experiments. AFRL has performed a field validation experiment using visible and 3-5 micron infrared imagers. These experiments have resulted in time series of 2 dimensional images of clouds at the test site. Comparison of these image time series with synthetically generated scenes is complex. A metric (a function on images) which is relatively invariant over the same class of images and clearly distinct on different classes of images is needed. The ingredients that constitute a class are somewhat ill defined, but need to be related to the end use of the cloud simulation.

To generate realistic synthetic scenes, a radiative transfer model must be used to propagate radiation through the synthetic liquid water content fields. We have used two codes to handle these calculations, the Boundary Layer Illumination Radiation Balance (BLIRB) model developed by the Army Research Laboratory and the Spherical Harmonic Discrete Ordinates Method (SHDOM) model developed by Frank Evans at the University of Colorado. Both models can perform radiative transfer calculations through clouds.

The two models differ somewhat in what constitutes the source function and emitting elements in the radiative transfer equation. These differences are displayed in Table 7. Skylight is radiation emitted from the top of the atmosphere. Thermal sources refer to atmospheric radiation - so the atmospheric temperature profile affects the thermal source values.

Various water content files generated by the CSSM were used to simulate cases of 25% to 100% cloud coverage. Each water content file simulates clouds within a box-shaped volume of air. Horizontal cross sections were taken at different heights within the volume to investigate resulting flux and radiance values (e.g. direct downward flux) from specific

input parameters to the model in an effort to obtain realistic cloud scene simulations from both models. Radiation and flux values were calculated for the grid cells in these cross sections with the SHDOM model at two specific wavelengths and flux values were computed with the BLIRB model for one wavelength range.

TABLE 7. Contributing Components and Emitting Elements	
BLIRB: Source Function is a combination of solar, lunar, thermal, point and beam sources, allows for the option of skylight	
Atmospheric effects	Surface effects
1. boundary conditions - open or periodic 2. atmospheric aerosols: e.g. rural, maritime, or desert 3. gaseous absorption 4. temperature: profiles exist for mid-latitude summer, or winter, sub-arctic summer or winter, tropical and U.S. standard 5. scattering 6. cloud presence	1. ground albedo - A. Lambertian, retro or specular B. various surface types e.g. tundra, grass, sand 2. terrain effects - shadowing and reflectance 3. bidirectional distribution of reflected light
SHDOM: Source function is a combination of solar and thermal sources. The solar source is considered to be a beam of light; allows for the option of skylight.	
Atmospheric effects:	Surface effects:
1. boundary conditions - open or periodic 2. gaseous absorption 3. temperature 4. scattering 5. cloud presence (determines extinction and cloud albedo among other things)	1. surface type - variable or fixed A. Lambertian B. Fresnel C. RPV (used to model bidirectional reflectance and characteristics of land surfaces (e.g. vegetation)) 2. ground temperature (comes into play only if a thermal source exists)

Figure 19 shows the results of the direct upward (left column) and direct downward (right column) flux for the 25% cloud coverage case with the BLIRB model; the rows signify different levels within the cloud volume. Each individual image within the figure is scaled from its minimum to its maximum value, so the values representing white (the maximum value) and black (the minimum value) are unique to each image.

Additional water content files with higher grid resolution were used with SHDOM. Since SHDOM was unable to directly handle these files because the larger sizes of these files exceeded array and memory limitations, these water content files were downsampled to a size SHDOM could use. Radiance fields output were expanded back to their original size using a modified format of bilinear interpolation to gain back some of the resolution lost in the downsampling process; these radiance fields were illuminated by an original-sized (e.g.

128 x 128 pixels) extinction field. Figure 20 shows an example from the 128 x 128 x 64 cloud case. The top image is a downsampled 64 x 64 horizontal cross section; the second image is the first image expanded back to 128 x 128 using a modified format of bilinear interpolation; and the bottom image is the second image illuminated by the extinction field shown directly to the right of these two images.

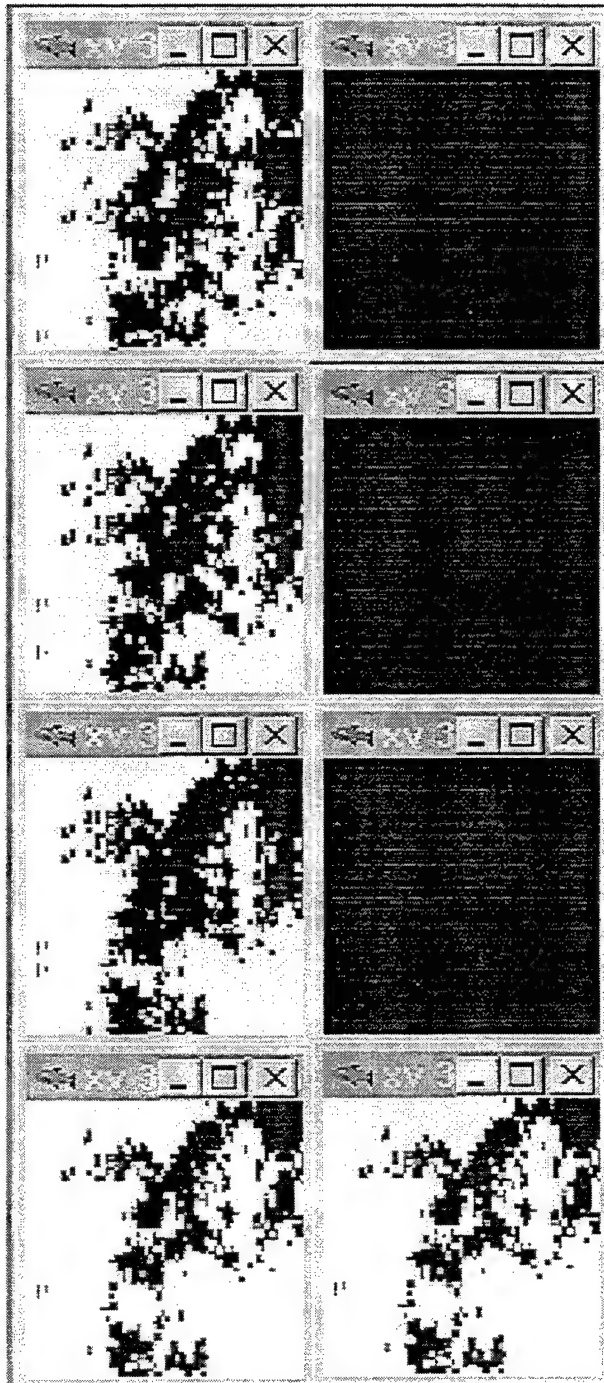


Figure 19. Results of the direct upward (left column) and direct downward (right column) flux for the 25% cloud coverage case with the BLIRB model.

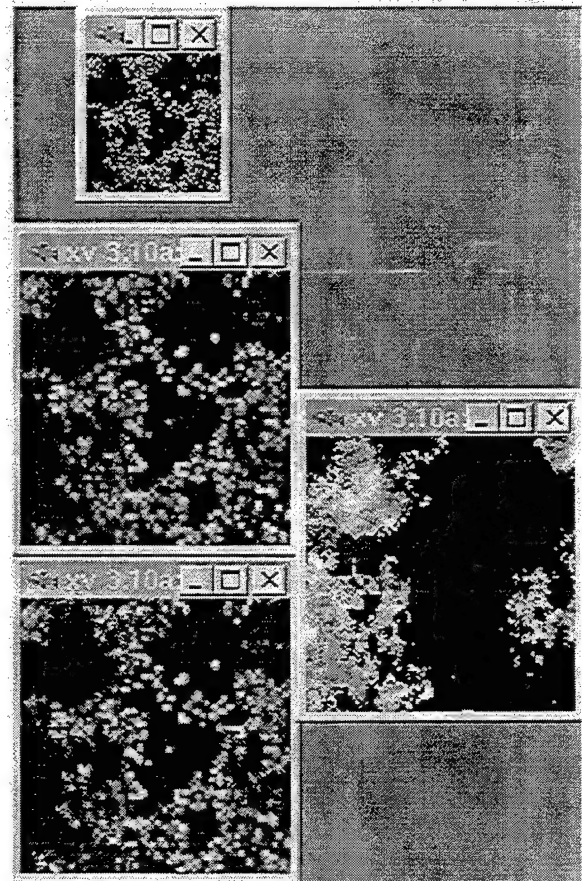


Figure 20. Example from the 128x128x64 cloud case.

We have investigated several different approaches to constructing figures of merit for comparison of field imagery with synthetic imagery. Moment analysis, gray level co-occurrence matrices (GLCM) [Gillespie, *et al.*, 1995] and singular value decomposition have been used. Moment analysis is computationally cheap and is especially suited to the first order calibration of radiative transfer schemes. Since all the spatial structure in the scene is integrated out, statistical moments cannot be the sole means of comparison.

In the GLCM approach neighboring pixel values are treated as values of two random variables. Their joint probability density function is estimated via their joint histogram, and statistical moments with respect to this density function are obtained to yield quantities such as Contrast, Homogeneity, Entropy etc. This technique yields a family of quantities that have some utility in image classification. Some of the spatial structure in a cloud scene is captured, but length scales longer than one pixel distance are not captured. Studies are presently ongoing using a multiple discriminant analysis technique to determine which quantities are most useful for characterizing 2-dimensional cloud images.

Contributing components to the source function and emitting elements to be used with the radiative transfer equation are shown in Table 7. Emitting elements are sources of radiation present in the atmosphere that are not part of the source function but attenuate intensity toward a given point in the atmosphere

5.4 VISUALIZATION

DoD modeling and simulation applications are increasingly seeking fast methods for visualization of realistic clouds as a method for gauging atmospheric effects on missions during planning, rehearsal and training.

We have developed a technique that renders clouds realistically in near real-time. Clouds are easily integrated into scene rendering software written employing OpenGL libraries and SGI's specialized texture-mapping hardware. The cloud data visualized by this software are produced using AFRL's Cloud Scene Simulation Model (CSSM), which uses fractal and physics-based techniques to produce synthetic fields of liquid water content corresponding to atmospheric clouds.

This cloud visualization technique was spawned by a broad-based need to meld the benefits of fast, hardware-based volume rendering with the physically accurate images obtained by radiative transfer calculations performed on a cloud field, a process too slow for real-time simulations.

Since clouds are characteristically formless objects, they are not amenable to traditional polygon rendering methods. Typical techniques offer a fair visual representation when viewed from great distance, but suffer from a lack of depth and no fine detail, making them unattractive for fly-through simulations. A relatively new method, three-dimensional texture-mapping, was used to create images with sufficient fine detail and speed to

facilitate such simulations.

An optical properties tool called Fastmap was used to derive optical depth information from the CSSM output. Fastmap maps CSSM liquid water content to particle-size distribution information and graphical quantities such as extinction optical depth in both infrared and visible spectra.

We used the AFRL Weather Impact Decision Aids (WIDA) program's Infra-Red Target Scene Simulation Software (IRTSS) software as a visualization environment in which to develop this cloud rendering capability. IRTSS renders high-resolution target and terrain scenes in both the IR and visible spectra at a high frame rate using OpenGL, hardware polygon rendering, and texture-mapping.

The format of the CSSM/Fastmap output was well-suited to the 3D texture supported by an SGI OpenGL library extension. The software developed in the work converts the liquid water content grid of a CSSM output file directly into a rasterized texture image. Both visible- and IR-spectrum cloud rendering is possible.

In keeping with a physics-based visualization, we determine the radiance field through a Beer's law attenuation calculation for setting cloud brightness values. Simply, we wanted to preserve the facts that 1) clouds are darker on the bottom, and 2) there is less ambient light beneath a cloud deck than above it.

The software ray-traces the Fastmap extinction coefficient grid produced from the input CSSM clouds, from each grid cell toward a hypothetical distant light source above the cloud field once while collecting cloud data. The software then integrates extinction optical depth along this path, then uses the value to estimate cloud brightness for each grid cell.

Considerable performance testing shows that the goal of cloud rendering high resolution images in near real-time -- on the order of 10 Hz -- has been met.

5.5 CLOUD SPECTRA AND CLOUD VERTICAL STRUCTURE FROM SATELLITES

Previous studies have compared the brightness temperatures resulting from two different radiative transfer models, RADTRAN and FASE. When identical results were produced from FASE using atmospheric profiles with and without clouds, it was discovered that FASE was not properly handling liquid attenuation. After conversations with the one of the FASE authors, Ned Snell, it was decided that this problem had "deeper roots" than first imagined. Since the corrections were beyond the scope of this investigation, an additional solution was proposed by Alan Lipton. It was decided that a combination of FASE and RADTRAN would serve as an immediate solution to the problem. The new model would use the FASE routines to compute gaseous optical depths while making use of RADTRAN liquid optical depth calculations. This work was carried out under the direction of Gerald Felde.

The first step in creating the new RADFASE model was to make several minor modifications to RADTRAN calculations. For example, radiance values were substituted for brightness temperature, making use of a newly added function to calculate the Planck temperature. These temperatures are eventually converted back to brightness temperature with a separate new routine. In addition, a term was added to the radiance calculation to compensate for space contributions. It was also noticed that in looping over the atmospheric layers, RADTRAN had redundantly added the top layer twice, contributing to slightly higher brightness temperatures. This was corrected in RADFASE.

Due to the basic differences between RADTRAN and FASE, several steps are required to run the new RADFASE model that make it rather complicated. One major difference is that RADTRAN is given either a selected list of frequencies or it is allowed to step over a range of frequencies given the starting point and step size. FASE, however, does not allow selection of specific frequencies. A beginning and ending wave number are selected while the step size actually changes throughout the run. To compensate for this, a list of the desired frequencies was added to the FASE input file and the user allowed to select one of three methods for determining the proper optical depths for use in the model. The user chooses to either 1) select the nearest frequency to the frequency of interest, 2) calculate the linear interpolation of the optical depth at the exact frequency of interest using the two frequencies on either side of the exact value, or 3) calculate the average optical depth and frequency for all values within a selected range. After testing each method, method number two was used for the final runs of RADFASE.

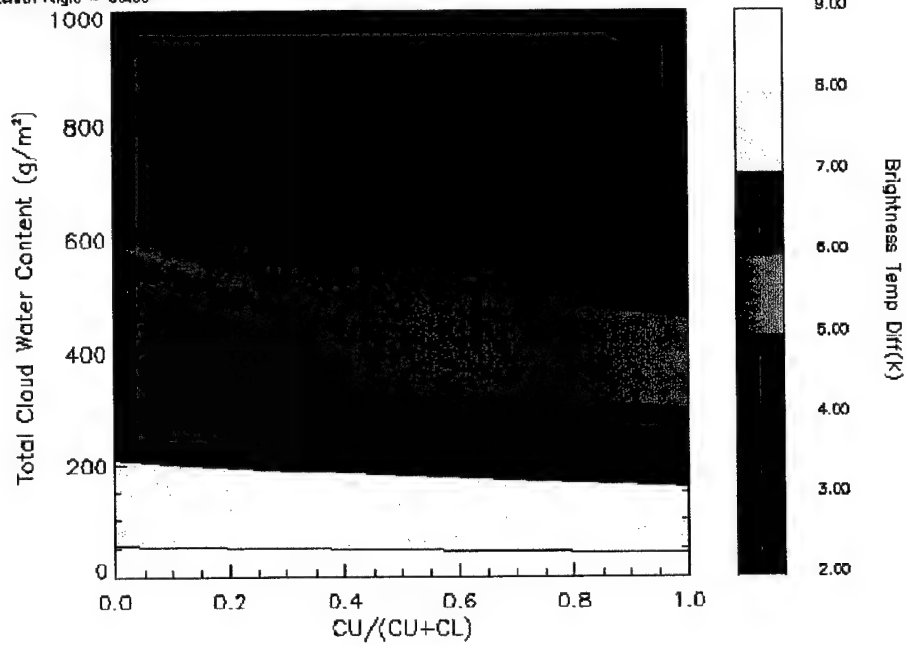
Several runs of RADFASE and RADTRAN were performed using various atmospheric profiles for comparisons of the two models. For each run, the thickness and water content of the cloud layer was varied while using a constant zenith angle and frequency list. A table was produced displaying the horizontal brightness temperatures and their differences for each of the individual frequencies.

Additional RADFASE runs were performed with atmospheric profiles containing two cloud layers from 0.0-1.5 km and 3.0-4.5 km, each with varying levels of cloud water content (CWC). Runs were performed for zenith angles of both 55 and 65 degrees. Contour plots for each frequency-zenith angle pair were made displaying the vertical brightness temperatures (T_{bv}) and the difference in vertical and horizontal brightness temperatures ($T_{bv}-T_{bh}$) at various total cloud water content levels ($CU+CL$, where CU = CWC of upper cloud and CL = CWC of lower cloud) versus the ratio of CWC in the upper cloud layer to the total CWC ($CU/(CU+CL)$). An example of each is shown in Figure 21. Cloud vertical structure information is obtained from satellite data by overlaying the two contour plots and comparing with the satellite measured vertical and horizontal brightness temperatures.

Runs 400-455...RADFASE 1.0
Frequency = 32.00GHz
Zenith Angle = 65.00°

Brightness Temp Diff Up (V-H)

Thu Jan 29 12:13:54 '98



Runs 400-455...RADFASE 1.0
Frequency = 32.00GHz
Zenith Angle = 65.00°

Brightness Temp Up Vertical

Thu Jan 29 12:13:54 1998

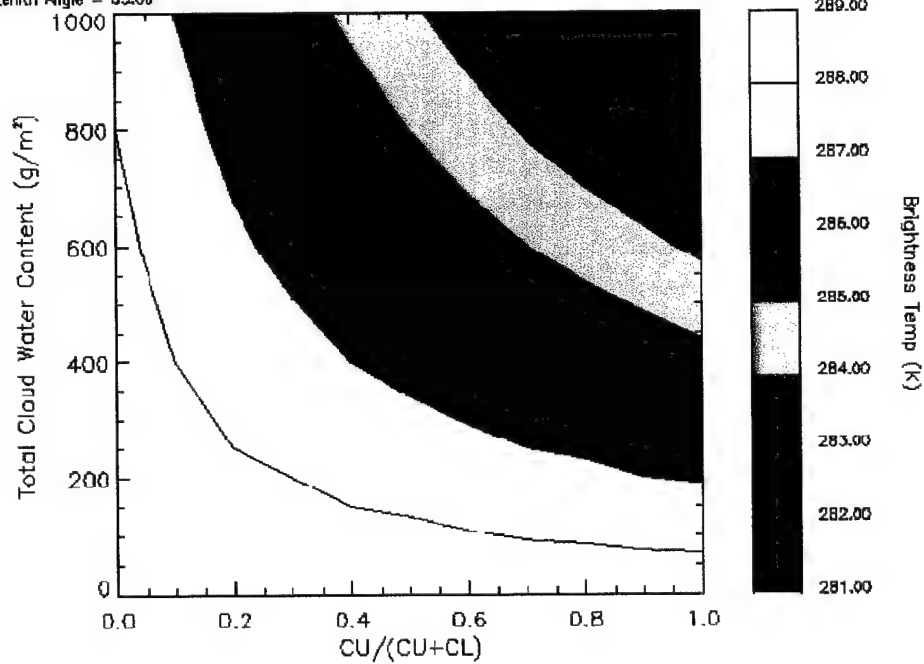


Figure 21. RADFASE results for a run at 32 GHz with a zenith angle of 65°. A) [Top] Contour plot of the difference in vertical and horizontal brightness temperatures at various cloud water content levels. B) [Bottom] Vertical brightness temperature contours at various cloud water content levels.

6. SCINTILLATION NETWORK DECISION AID (SCINDA)

6.1 SCINTILLATION

After two decades of intensive theoretical and experimental investigations, the space-time variability of nighttime F-region irregularities remains an outstanding problem [Basu and Basu, 1985; Basu, et al., 1996]. These irregularities cause amplitude and phase scintillation of satellite signals which cause serious concern among system engineers. Scintillations affect satellite communication and navigation systems in various ways [Aarons and Basu, 1985; Basu, et al., 1995]. Amplitude scintillations induce signal fading which can produce message errors in satellite communication systems and may cause the loss of position fix or degradation of accuracy in Global Positioning System (GPS) navigation systems.

Forecasts of equatorial scintillation are needed to be certain that the outages are caused by scintillation and not by system failures, and also, to develop alternate methods of communication and navigation. This need has been emphasized in the interagency "National Space Weather Program (NSWP) Strategic Plan".

The climatology of equatorial scintillation is quite well established and its features can be reproduced by use of the upgraded scintillation model, WBMOD [Secan, et al., 1995]. However, scintillation weather information can not be provided through WBMOD, due to the extreme temporal and spatial variability of scintillation.

There are at least two types of nighttime F-region irregularities arising in the equatorial region, namely, those related to plasma bubbles [Harendel, 1973; McClure, et al., 1977; Scannapieco and Ossakow, 1976; Ossakov, 1981; Kelley, 1989], and the other type called the bottom side sinusoidal (BSS) irregularity [Valladares, et al., 1983].

6.2 DEVELOPMENT OF SCINDA

The Scintillation Network Decision Aid was developed as a "proof of concept" system with the purpose of providing near real-time warning of communication outages due to equatorial spread F (ESF) instabilities [Kelley, 1989]. The ESF phenomenon results in plasma density depletions or bubbles in the topside ionosphere. Data are collected at two South American locations that continuously monitor the scintillation index S_4 . The complete process of downloading the data through analysis is described in McNeil, et al. [1997]. The data are analyzed with the Discrete Bubble Model (DSBMOD) [McNeil, et al., 1997], which detects, characterizes, and propagates the depletion bubble to provide a picture of current outage conditions and to forecast predicted outages for the next few hours. Output from the model consists of three-dimensional depletion bubbles that are mapped along magnetic field lines; have characteristic top-side heights, time durations,

and turbulence strengths; are calculated from the measured S_4 , and are dependent on the geometry of the station and satellite link where the measurement was made. A data-driven model of the anomaly crest is used to predict the scintillation level along the latitudinal extent of the bubble and a phase screen model [Rino, 1979] is used to compute the equivalent S_4 for arbitrary ground station and satellite pairs.

The model results are displayed and manipulated by a visualization tool incorporating several options of operational significance. The tool has full ephemeris capability for any satellite in the current data base. Bubbles are displayed in three dimensions along with selected ground station to satellite links, and continental outlines or a surface photograph are rendered for orientation. Links are colored to indicate outage conditions. In addition to the real-time capability, the tool has a play-back option for anomaly analysis. Two-dimensional maps can also be generated showing ground projections of the bubbles with S_4 index computed for a chosen satellite and frequency. The 2-D maps can be projected ahead in time up to a maximum of three hours to show the predicted outages at future times. Hard copy of these maps, suitable for facsimile transmission, can be generated in support of mission operations. To provide global coverage and to forecast when scintillation has not been observed or data are not available, the tool displays the predictions of the Wide Band Model WBMOD [Secan, et al., 1995]. This version of WBMOD is itself driven by real-time scintillation data, where available. The overall concept of SCINDA is diagramed in Figure 22.

The two UHF sensors now in place have been operational for more than four years. The LBAND systems currently in place have been operational for more than a year now, and add considerable detail for ionospheric analysis. Climatological information gathered from the rather unique configuration is currently being analyzed and is expected to contribute to our understanding of equatorial ionospheric irregularities. The system is being expanded to provide coverage in regions of military significance and to investigate the global behavior of scintillation. GPS scintillation units have been installed at the South American sites and are now fully integrated into SCINDA. UHF and GPS systems are in operation at Ascension Island, and will soon be included in the network. GPS receivers have been installed in Northern Australia, though it is unclear when they will be available for inclusion in the network. A mobile DMSP receiver and a GPS unit will be deployed on Guam sometime this year.

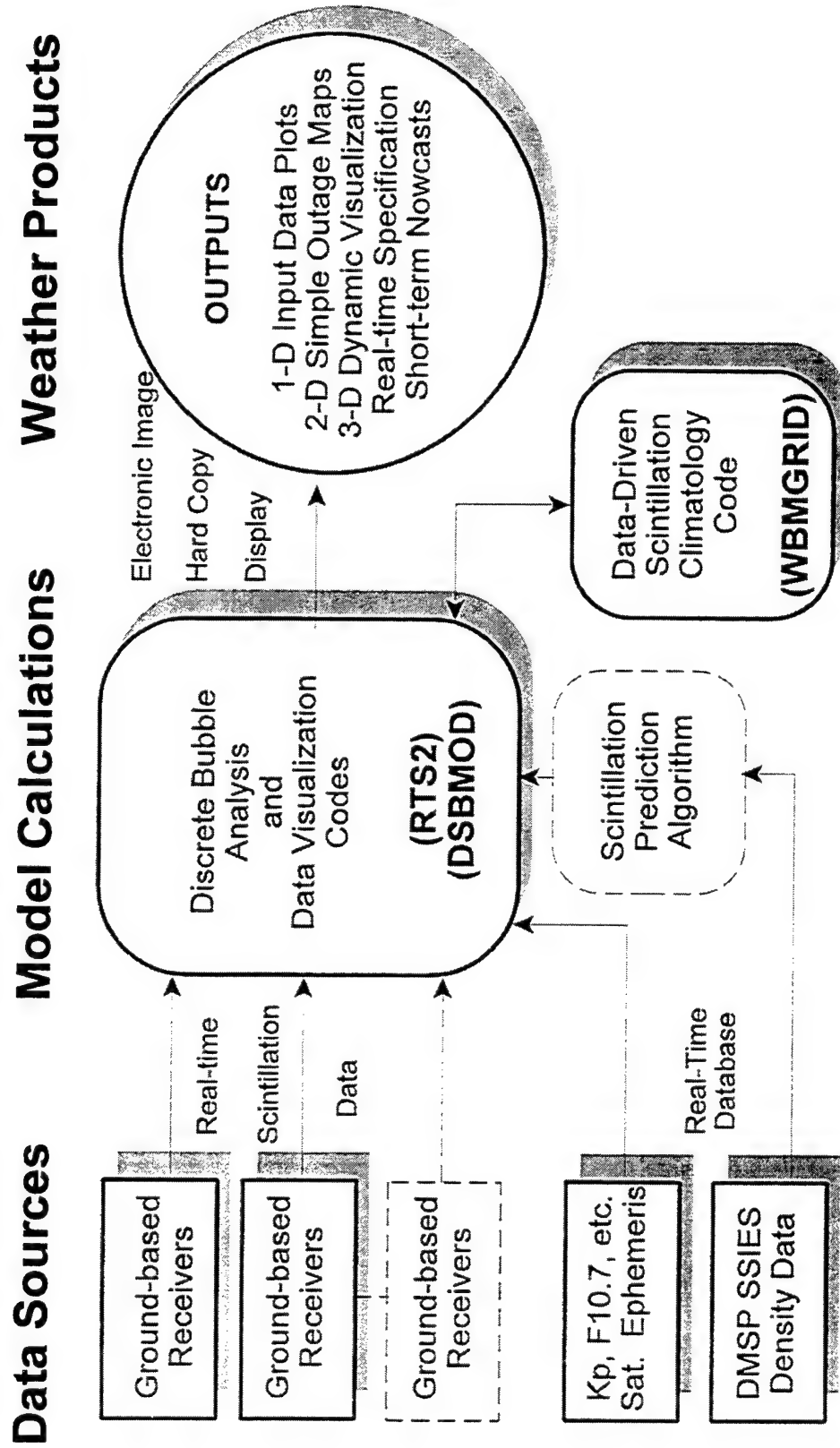


Figure 22. SCINDA system concept.

6.3 VERSIONS OF SCINDA

A new version of SCINDA numbered 3.5 was delivered to 55th SWXS and SSSG in November 1997, and a follow up release version 3.5b was delivered in January 1998. In the process of preparing this delivery, the entire SCINDA system was modified in many ways, including the development of L-band capabilities, WBMOD 24 Hour Climatology Product, SSIES hooks, Multi-Message Line, Full Globe Rotation, and Satellite Icons. These improvements and changes took place between May 1997 and December 1997.

In the first four months of 1998 the SCINDA project concentrated on the development of SCINDA version 4.0 with a new graphics library, and the validation of the current SCINDA models. The validation process looked at all sky data, data reliability, consistency in projections, time and spatial projections of data, and at "false alarm" generation rates.

Over the course of the past year, there have been several major changes to the data collection network. GPS receivers at Ancon and Antofagasta have been added. Algorithms have been developed to transfer data from the remote site only if new data are included in the file. New software has been installed at the sites as part of prototype for the Novatel GPS receivers. Upgrades to the networking software have also been made for enhanced reliability.

6.4 MODEL DEVELOPMENTS

The DSBMOD model has undergone many changes to make it more effective at telling the operator what is happening. A multi-line broadcast message system was developed. In addition, a broadcast message was also added to the data stream, in order to inform stations outside of Radex when important events occur with SCINDA. Several bugs within the model were fixed, including the routine to eliminate structures when the sunrise occurs.

DSBMOD is now able to generate L-band scintillation structures using the GOES-8 data. These structures are spread out latitudinally to about 12 degrees around the geo-magnetic equator. They are drifted in the longitudinal direction based on the ionospheric drift velocity measured from the collocated UHF receivers. The model also includes information in the message line, and determination of communication link scintillation state. The L-band model in DSBMOD also has the capability to extrapolate $C_k L$ values to other frequency regimes, expanding the capabilities of the Outage Map prediction tool.

A threshold recognition and subtraction algorithm was added to DSBMOD's processing. This is necessary to remove the baseline S_4 level which is due to the drift of the satellite position from the antenna signal strength. The median S_4 level between 2200Z and 2300Z is used to determine this baseline level. If the level is above 0.3, then the model refuses

to use the data to predict scintillation structures, and puts out an error message indicating that the antenna needs to be realigned.

GPSMOD was created to use the GPS receiver data for DSBMOD. The GPS receivers at Ancon and Antofagasta were added to GPSMOD using the phase scintillation (σ_ϕ) to indicate scintillation activity level. GPSMOD has the ability to accept data from any station, the inputs and model are generic, in order to accomodate new GPS stations. No structures are projected based on the GPS receiver data. However, all the ionospheric intercept points are calculated from GPS ephemeris, and displayed with their activity level as indicated by the σ_ϕ . This is at least an indication of the scintillation activity levels in the region, and is also an excellent method for validating the drift of the LBAND bubbles generated from the GOES L-band data.

The ionospheric penetration points along the station-to-satellite link are indicated by "dots" in SCINDA, colored to indicate the scintillation intensity. These dots are moved eastward according to the climatological zonal ionospheric drift, adjusted for the drift velocity measured at Ancón and Antofagasta, between times of GPS data reporting. This is important when there are data drop outs during the night, to keep the detected scintillation inline with the movement of the ionosphere, rather than with the satellite motion.

6.5 SOFTWARE UTILITIES

To service the operational needs of 55th SWXS, a WBMOD 24-hour product utility was created. The utility was incorporated into both the GEOSpace and SCINDA programs. The utility allows crews to designate a list of satellites for a particular station. Then the WBMOD program is applied to each link over a 24-hour period, and a listing of probable signal degradation is created for each specified link. The program includes several features like automated geophysical parameter lookup functions, and automatic display of a concatenated results file.

A completely new online help system was created for the SCINDA main display. The new help is HTML based, and Netscape is used to display it. The help includes fully "functional" images of the displays, allowing the operator to select the function from the display, and a help window is displayed.

The user interface to the SCINDA main display was reworked for the October 1997 freeze and November 1997 release of SCINDA version 3.5. These changes included frequency selection, day/night terminator follow mode, a reorganization of buttons, and the development of a new threshold control window. Continuous color displays of the scintillation intensity in both the UHF and L-band displays was included for the SCINDA 3.5 release. A legend window was also created in order to indicate the dB Fade levels associated with each color used in the display. The "Real-Time" mode was modified to reduce the processor load, and the play back feature has a new 24-hour feature.

A Gallery feature was added to the SCINDA interface to allow the user to view ten runs simultaneously. This works by saving the image of the main display to GIF files, and creating an HTML page to view the images. Combined with the 24 hour time step feature, this is a quick way to look for days with active scintillation.

New view controls were added to SCINDA to allow the operator to more fully control the perspective. This entails the ability to designate a viewpoint origin, and then the rotation and translation from that point. This allows the designation of predefined viewpoints above each of the major equatorial theaters.

The generic graphics library for the new SCINDA 4.0 release was approximately 90% completed under this contract. This library will serve as the basic code for several other projects in the future, and will increase the performance of the SCINDA graphical user interface. The graphics library is capable of displaying generic data files, and will therefore increase the ease with which new features are added to the SCINDA system.

6.6 THE NOVATEL RECEIVERS

The Novatel GPS receivers have been problematic in the computation of the scintillation index S_4 during moderate scintillation. An unusual summer time scintillation event was studied to examine the cause of high S_4 calculations. The GOES receiver recorded an S_4 level of 0.6, the strongest summer time L-band S_4 observed. Using a spectral analysis, it was determined that an as-yet unknown source of contamination in the power levels is irreparably changing the S_4 values. The good news was that the phase scintillation (σ_ϕ) values did not appear to be affected, and therefore a decision was made to use the phase scintillation values to indicate scintillation intensity from the Novatel GPS receivers.

Updated data collection software was developed and installed on a Linux laptop PC. This was a prototype development intended to replace the existing systems at Antofagasta and Ancon. This is also the system that will be replicated for new sites as they come on line. This prototype was installed in August 1997.

In an effort to diagnose the problems with the amplitude scintillation (S_4) numbers generated by the Novatel receivers, an analysis of simulated scintillation data from Wright-Patterson AFB was facilitated.

Because of continued problems with the reliability of the S_4 calculations from the Novatel receivers, the 60 second phase scintillation (σ_ϕ) has been used to incorporate the GPS receiver data into SCINDA. As part of this effort, a phase mask for the Antofagasta site was constructed to remove multi-path effects. It was found to coincide almost exactly with the previous S_4 mask. After a reevaluation, the σ_ϕ mask was modified to eliminate phase fluctuations over 0.1 radians.

6.7 PREDICTION AND CLIMATOLOGICAL STUDIES

The climatological studies done within the SCINDA project were presented at the Spring 1997 AGU conference in Baltimore, Maryland. This included a video demonstration of the development of scintillation structures as seen from the SCINDA main display. Spectral studies and night-to-night predictive studies were also presented at the conference.

Spectral studies were done on the 512 point decimated time series data from Antofagasta to determine if bottom-side sinusoidal (BSS) effects could be differentiated from spread-F scintillation structures. The spectral studies showed the characteristic interference patterns of BSS. This indicates that spectral analysis of the scintillation data holds promise for differentiating true spread-F scintillation from other natural factors, and perhaps also from jamming effects.

A night to night analysis of scintillation activity was done to increase the predictive capabilities of SCINDA. Most notable from this was the fact that there was a 91% chance of at least one hour of scintillation following a night with at least three hours of scintillation. These techniques hold promise compared to the uncorrelated averages provided by current climatological models such as WBMOD.

6.8 DEMONSTRATIONS AND PROMOTIONAL MATERIALS

A workshop on the effects of scintillation on communication and navigation systems was held at ComSat corporation in Bethesda, MD on October 22-24 1997. Several parts of the demonstration poster were prepared, and an SGI workstation was transported to the workshop for demonstration of the full SCINDA capability. There appeared to be appreciation of the SCINDA system among the workshop participants.

A comprehensive set of web pages were designed as a demonstration of the SCINDA project. These pages include a fully functional image map of the major SCINDA components. A video clip of the SCINDA system in action was also included in the demonstration materials. These materials were copied onto CDROM format for use by Space Command in briefings, and for use by USAF representatives at NUNN project briefings for NATO members in the United Kingdom. Additionally, double sided color pamphlets have been prepared for demonstrations at the NUNN conference, at Space Command, and at an air show in Berlin, Germany.

The set of demonstration web pages, along with a real time image of the current South American sector scintillation activity are made available as a test web site. The real time images on the test web site are snapshots of the scintillation activity taken every half hour throughout the night. The images are archived for a three day period. This is a prototype for the site that will be established on the official Hanscom web server.

7. THE STUDY OF ATMOSPHERIC METALS

Since the early optical observations of the Na(D) nightglow in the first half of this century, it has been known that the Earth's atmosphere contains considerable concentrations of metal atoms, ions, and complex molecules. Metals have been of considerable interest to both experimenters and modelers because metals in the atmosphere are related to several phenomena that directly impact many Air Force systems. Metals constitute a large part of the atmospheric UV backscatter in the Earth's day glow. Metals are good tracers for thermospheric transport processes, this being due to their long lifetimes above the mesopause. Variations in the mesospheric metal layers are used by adaptive optical systems to correct visual telescopes for turbulence.

It is generally accepted that atmospheric metals arise from the ablation of cosmic dust or meteors as they are heated during entry into the Earth's atmosphere. Any serious modeling of atmospheric metals must begin with accurate modeling of the source of these metals. Metals and the showers that produce them have been implicated in the formation of sudden layers and sporadic-*E*, which are very important processes for HF communicators. Aside from the potential relationship between meteor showers and sporadic-*E*, there is considerable interest at present in meteor burst communications which rely entirely on meteor trails for transmission and reception over the horizon. Since meteor trails have traditionally been extensively studied by radar, it follows as well that trails could be a significant source of radar clutter both for over-the-horizon radar and space-based radar imaging systems. Sporadic-*E* and spread-*F* also present potential complications for these systems. Emissions from trails could also contaminate UV and visible space-based targeting systems, since optical tracking algorithms must be made insensitive to these events. The possibility of significant modifications in the *E*-layer due to major meteor storms also deserves mention, especially in light of the potential for major Leonid storms in the next few years.

We have become involved in a program directed toward modeling of the atmospheric effects of meteors and of the metals they leave behind. Our modeling has addressed many important aspects of the ablation process that initially injects metal atoms into the atmosphere, the chemical reactions of these metals with the ambient constituents, and the transport of these metals both in the mesosphere and, in ionic form, high into the thermosphere. This modeling has been carried out in a comprehensive fashion, treating all of these aspects of the problem in analytical ways whenever possible. It has also been a goal of the program to examine and incorporate metal and other data whenever possible for model validation purposes and to enhance our understanding of important processes. This report describes three specific areas in which recent substantial progress has been made: (a) modeling of the differential ablation of cosmic dust and the subsequent modifications of the relative abundances of metals in the mesosphere, (b) modeling of meteor trails as they are observed with a potassium lidar and, (c) completion of modeling of the observations from the first of six GLO experiments carried out on the Space Shuttle.

Following a description of our overall modeling program, we will describe the major advances made in these three fields.

7.1 MODELING TECHNIQUES

Previous modeling of meteoric metals in the Earth's atmosphere have for the most part focused on one particular aspect of the problem. Although quite successful in achieving their respective goals, these types of models suffer in that one, in general, requires the results of another for input. For example, even the most comprehensive model of *Carter and Forbes* [1998] requires the assumption of a profile for the deposition of iron in the atmosphere. These features limit the model codes in that they are not readily applicable to a wide variety of geophysical phenomena. For example, one cannot study ion transport with a steady state code, nor can one readily study the response of the metal layers to changes in deposition rates and characteristics with such a code. Even in the time-dependent codes, with which such studies could be carried out, the changes in deposition can only be guessed at. Most transport codes, lacking sufficient chemistry, are inadequate to allow for testing of proposed reaction schemes and rate constants.

We have developed a new type of code that is free of many of these limitations in that it is comprehensive. By this we mean that the result depends on the result of some generally accepted (or variable) model for required inputs. Among these required inputs are atmospheric density and composition, ionospheric density and composition, diffusion coefficients, the Earth's electric field, and other transport processes, such as neutral winds. All other required processes are modeled within the code through reasonably well accepted physics. These include rates and profiles of metal influx, which we derive from accepted equations describing the entry and deposition, and which we have in the course of this work refined to account for the differential rates of deposition of various types of metals. Another important aspect is the relatively complete treatment of chemical reactions which create ions, recycle them to neutrals, and ultimately remove neutrals from the system. By the investigation of simultaneous neutral layers, we have been able to refine the chemical schemes for various metals by comparison with data, thereby giving us a model which can be used with some confidence in the treatment of many species, with extension to those species not presently included being absolutely straightforward. In Figure 23, we attempt to convey the methodology of our modeling technique by showing the flow of information and the required inputs.

The first step in the model is to compute deposition rates of metallic species. This requires both the specification of an atmospheric density, which is currently derived from MSIS, and information about the source or sources of the cosmic dust. This information includes overall influx rates and angles of attack, the velocity of the particles, and the distribution of the particle sizes in the various cosmic dust sources. Atmospheric density also depends on such things as location, epoch, and solar/geophysical activity. We have enumerated the most important dependencies within the boxes belonging to each specific model.

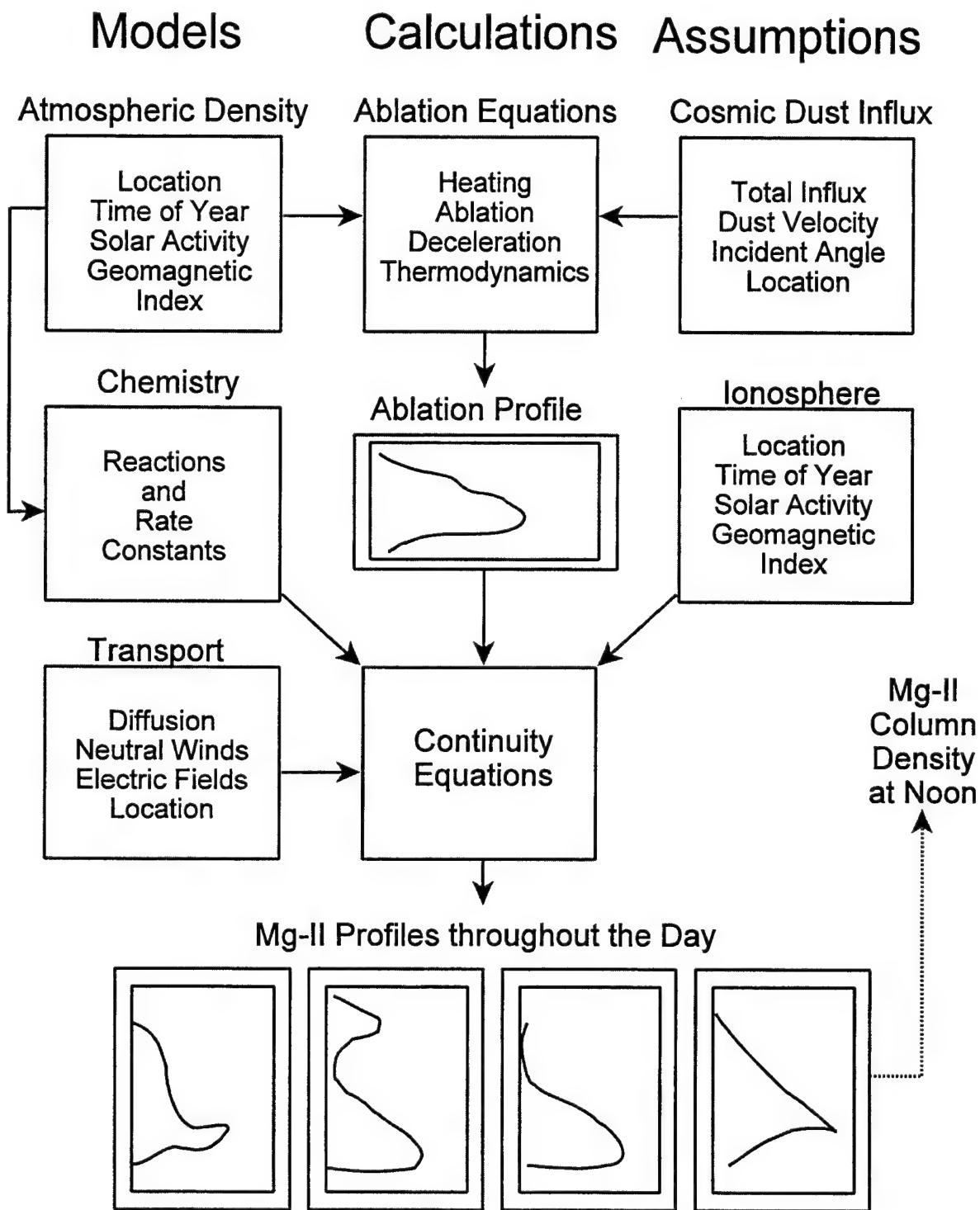


Figure 23. The inputs and flow of computations in a generic representation of our modeling, with "Mg-II Column Density at Noon" meant to represent one of many possible results derived from the model.

The deposition profiles are computed through standard equations for meteor entry and ablation, which follow closely those of *Love and Brownlee* [1991]. We have recently added to these a model for the differences in ablation for different metal species [McNeil, *et al.*, 1998a; 1998b] and have found that these differences have profound effects on the relative abundances of these metals in the mesosphere and thermosphere. These entry and deposition equations are now applicable to various metals. It is through these equations that the effects of meteor showers and storms can be modeled. We will elaborate on our results to date in both these areas, when we review some of the recent applications of this modeling.

The result of the first computation is one or a series of deposition profiles which is then injected into a code for the computation of the time behavior of the atmospheric metal layers in response to this deposition. The model solves continuity equations which are currently limited to vertical variation in the metal densities and result in a time-dependent altitude profile of the metals, which we have attempted to illustrate in Figure 23 for Mg⁺. The model also allows profiles to be derived for neutral Mg and, currently, for neutral and ionized Ca, Na and K. Other species can be added by revisions in either the chemical schemes, the deposition models, or both. For descriptions of the chemical schemes used for the various metals see *McNeil, et al.* [1995;1996]

The results of these computations can be used in a variety of ways, depending on the application. In the study of metal radiance at the equator, the densities derived from the model were used in the computation of radiance from the various metals using a second model incorporating the instrument look direction, the local time of day, and the shielding of the Earth's ozone layer. In our work, which revolves around the use of modeling in the attempt to understand specific data, it is often desirable to use this approach rather than attempt to reduce the data to such an extent that it is directly comparable as densities. One might say that our approach is in two distinct steps: first we attempt to model the atmosphere and then, using these results, we attempt to model the experimental results for comparison.

Time varying driving forces can be introduced at several points along the way. The input models themselves, such as MSIS and IRI, can be driven by variations in solar/geophysical parameters and these, in turn, can impact deposition, both through the change in altitude and extent to which ablation of cosmic dust takes place. These changes can also change the rates of cycling between metal ions and atoms as well as the rates of removal from the system. The chemical rates can also be given time variation through variation in the temperature with corresponding variations in reaction rates. The aspect of the model which we find most exciting in this respect, however, is the ability to introduce meteor showers in a self-consistent manner. This aspect is particularly relevant in view of the recent interest generated by the potential for a strong Leonid shower in the next few years. We expect that this model will be applied to a wide variety of problems in the future, including meteor shower modeling.

7.2 RELATIVE ABUNDANCES OF MESOSPHERIC METALS

It has been known for some time that an anomaly exists in the relative abundance of calcium and sodium in the mesosphere. While cosmic dust contains nearly equal amounts of both metals, the calcium column density is 50 or 100 times lower than the sodium column. The possibility that chemistry is responsible for the depletion of calcium relative to sodium has been ruled out. We have applied our model to investigate whether differential ablation could be the cause [McNeil, *et al.*, 1998a; 1998b]. The concept of differential ablation revolves around the idea that the more volatile sodium is evaporated off the meteor more completely than is the calcium and that it is evaporated off at an earlier time during meteor entry.

The basis of this modeling was the application of a differential vapor pressure model, which computed vapor pressures above a model solution of metal oxides, to the standard *Love and Brownlee* [1991] equations for meteor entry and evaporation. The formalism for computing the vapor pressure for an ideal mixture of metal oxides in the melt was developed by *Fegley and Cameron* [1987] on their work on the formation of the planet Mercury. Briefly, the Fegley and Cameron model uses thermodynamic equilibrium to compute the vapor pressure and composition of the vapor above a melt which is a combination of metal oxides, such as Na_2O , CaO , MgO , SiO_2 , *etc.* What is striking about the curves presented in Fegley and Cameron is that the vaporization of the sodium oxide is complete within the first 5% of the mass loss. Also, during this period, the vapor above the melt is almost completely Na, O and O_2 . As obviously follows, the change in composition of the melt with respect to the other metal oxides is minimal during the sodium vaporization. These features suggests a very simple model for sodium ablation, that the sodium comes off independently of any of the other metals in the particle.

To implement this model, we need a vapor pressure which we obtain by the Fegley and Cameron technique for a mixture of 49% SiO_2 , 49% MgO and 2% Na_2O . These vapor pressures were evaluated at several temperatures and were fit to a standard form for vapor pressure laws. The crux of the sodium ablation model is, then, that the sodium comes off first while the rest of the cosmic dust melt remains intact. This is quite consistent with experimental results which, while perhaps not precisely duplicating the cosmic dust ablation process, argue for the early evaporation of sodium. Potassium, which is currently incorporated into the model though not shown here, is assumed to evaporate identically to sodium, based again on high volatility from both model and experimental results.

Once the sodium has vaporized, the pressure drops dramatically. After this point, we model the ablation of magnesium with the vapor pressure of a two-component system initially containing a 1:1 mixture of SiO_2 and MgO . The general idea is that, so far as magnesium is concerned, the ablation takes place almost as if the other elements were not present at all. Magnesium will be removed at a rate proportional to its mole fraction in the vapor. However, over the better part of the evaporation process, the concentrations of Mg and of Si are approximately equal, so it suffices to assume that the vapor is of the same composition throughout the evaporation process in so far as magnesium is concerned.

We model the deposition of calcium by relation to magnesium. According to *Fegley and Cameron* [1987] magnesium and calcium in the vapor parallel each other quite well down to the 80% ablation point. This behavior is also seen in the experimental curves, where the relative abundance of CaO and MgO is approximately constant down to the point where about 90% of the meteor has vaporized. As dust particles pass the point of 80% or so ablated, it appears that they become rapidly enriched in calcium relative to magnesium. However, during most of the ablation process, calcium and magnesium appear to be coming off at rates proportional to their abundances. For this reason we have chosen to model calcium ablation with the same vapor pressure law as is used for magnesium.

Interestingly enough, we find that the differential ablation hypothesis works rather well *if* it is assumed that the vast majority of the cosmic dust particles enter the Earth's atmosphere with small geocentric velocities. Figure 24 shows a deposition functions for the case where 98% of the influx is at 12 km/second (the minimum escape velocity of the Earth) while the remaining 2% are of higher velocity. We see that calcium and sodium differ in two important respects. First, the calcium deposition is lower in absolute magnitude than is the sodium. In this case, the ratio of deposited Na:Ca is 6:1. We call this effect "direct" differential ablation.

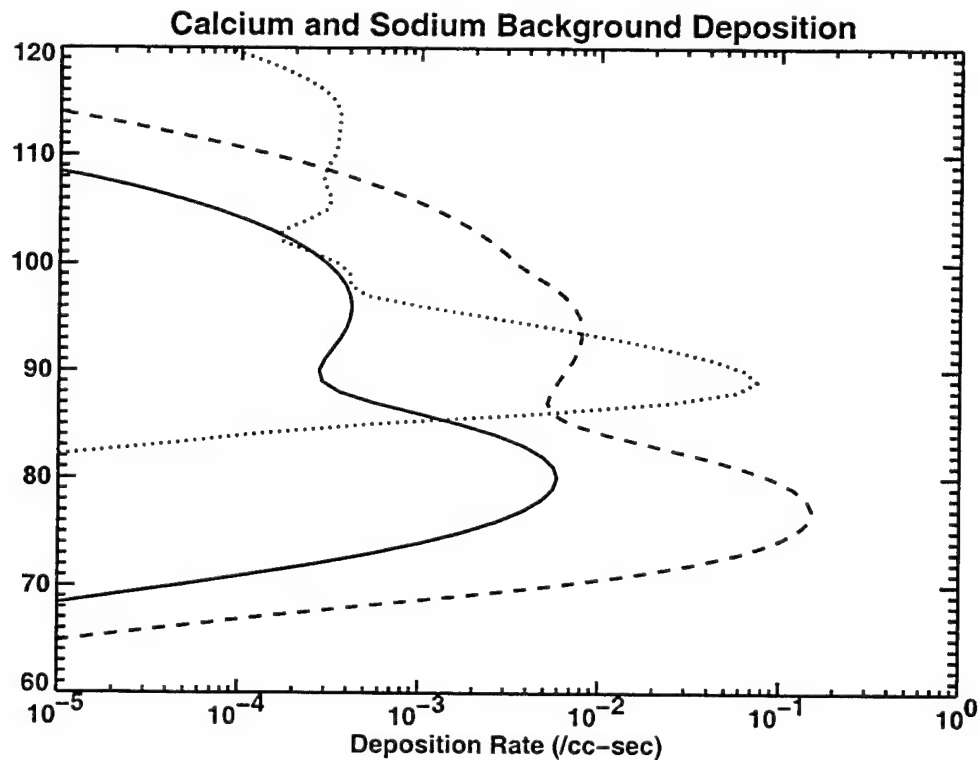
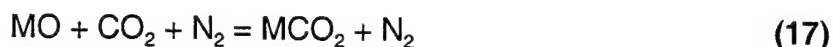
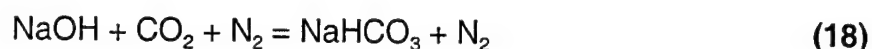


Figure 24. Deposition functions for calcium (solid line), sodium (dots) and magnesium (dashes) as computed from the differential ablation model.

A second and more significant difference is that calcium is deposited at substantially lower altitudes than is sodium. In this case, sodium deposition peaks at 90 km while calcium peaks at 80 km. This second aspect of differential ablation is even more important than is the fact that a substantial fraction of the calcium remains within the meteorites. Both calcium and sodium are removed from the system primarily through three-body processes. The gas phase metal oxides MO (with M=Ca,Mg) or the hydroxide species NaOH are removed through these three-body reactions:



for calcium and magnesium or



for sodium. The rates of these reactions are significantly higher at lower altitudes, since both CO_2 and N_2 vary approximately exponentially with altitude in the mesosphere. Therefore, if calcium is deposited substantially lower than sodium, it will be removed proportionately faster, leading to a lower steady state concentration of calcium, and thus a higher level of depletion relative to sodium.

The velocity distribution chosen resembles somewhat the measured velocity distribution of sporadic meteors, with a peak at relatively low velocity. However, it is important to note that the major contributions to the atmospheric metal layers come from particles between 50 μm and 1 mm in diameter. These are far too small to be seen visually, and only the largest and fastest of these would even produce an observable radio echo in common equipment. The hypothesis of a cloud of small, slow dust is consistent with the idea of the decay of cometary ejecta through circularization of the orbits of the smaller particles due to the absorption and release of solar photons. This is the Poynting-Robertson effect. The tendency of the Earth's dust cloud to favor 200 μm particles is well established, most recently by LDEF measurements analyzed by *Love and Brownlee* [1993]. The Poynting-Robertson effect is therefore called upon to explain the low velocity, since they orbit with the Earth at 1 A.U. and enter with the "capture" velocity of 11-12 km/sec. The velocity of the dust has not been observed directly through experiment, however. The origin of the majority of cosmic dust may be, as some claim, asteroidal.

In the course of this modeling, we also needed to investigate the rate of the ion sink mechanism



the product of which is almost completely reconverted to the neutral metal species. The rate of this reaction is unknown experimentally for Ca and Mg, although the compound has been observed for magnesium. Comparisons were made to compilations of ion mass spectroscopy measurements, which allowed us to derive a rate constant giving good

agreement with the observed mesospheric ion layer.

The proof of any modeling of this sort comes ultimately in comparison of predictions with data. Examining the neutral layers first (see the right side of Figure 25), the peak neutral densities for sodium and magnesium are approximately the same while the model of *Plane and Helmer* [1995] gives a magnesium layer which is smaller than the sodium layer by about a factor of five. *Plane and Helmer* [1995] use an alternative sink mechanism involving $\text{Mg}(\text{OH})_2$, which could easily explain the difference. There is as yet no measured magnesium layer with which to compare. The peak in calcium density is about 30 times smaller than the sodium peak. *Qian and Gardner* [1995] find through simultaneous lidar measurements of Na and Ca that a factor of 25 is roughly the ratio of the peak calcium to sodium density while we arrive at a value of about 30. One substantial difference between the layers of *Qian and Gardner* [1995] and our model layers is that the former are closer to each other in peak altitude and overall shape while our calcium peak is about 1 km lower than the sodium peak with also a lower top and bottom-side. This suggests that the model removal rates may be somewhat off. If the sodium removal rate were closer to the calcium removal rate this would lower the bottom-side of the sodium layer and also increase the depletion ratio between sodium and calcium neutrals, bringing even closer agreement with the measurements.

Turning to the ions (see the left side of Figure 25), the *Plane and Helmer* [1995] model agrees with the present one in predicting a sodium ion peak near 100 km compared with an magnesium ion peak around 90 km. That the sodium ion peak is actually somewhat higher than that for magnesium is, at least, suggested by several rocket results [*Aikin and Goldberg*, 1973; *Kopp and Hermann*, 1983]. These also suggest a magnesium ion peak around 92 km, which is quite close to our result. The absolute column density of magnesium ion is predicted by the model to be about $1(10)/\text{cm}^2$ while *Anderson and Barth* [1971] find it to be closer to $4(9)/\text{cm}^2$. The peak magnesium ion density is about 2,000 /cc which is consistent with ion mass spectrometry measurements [*Aikin and Goldberg*, 1973; *Kopp and Hermann*, 1983]. Both of these are scalable parameters in the model, but recall that they correspond to a previously chosen column density for the sodium neutrals of $5(9)/\text{cm}^2$ so that these comparisons do have meaning.

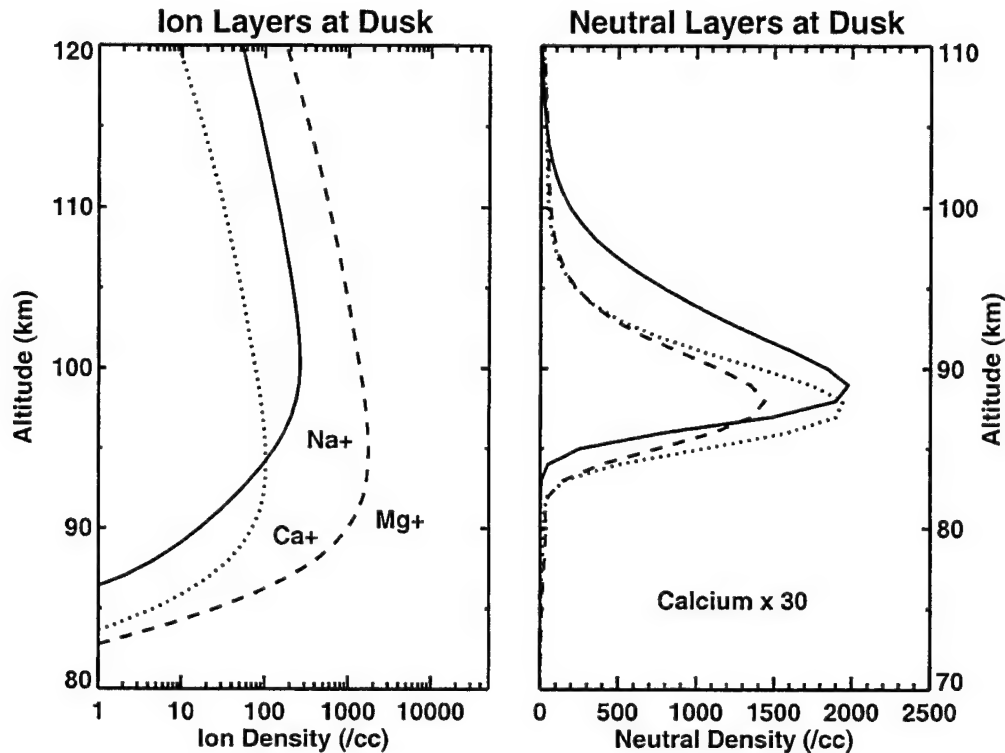


Figure 25. The mesospheric ion and neutral layers at dusk as derived from the model for the three metals considered. Note that the neutral calcium layer has been scaled up by a factor of 30.

7.3 MODELING OF METEOR TRAILS

The motivation for this work arose from observation of the 1996 Leonid meteor shower with a potassium lidar [Höffner, *et al.* 1998]. During the night of November 16-17, the outburst component of the Leonids was observed in Kühlungsborn, Germany. The outburst is that section of the meteor stream which gives rise to the spectacular showers with hourly rates in excess of many thousand visible meteors. The lidar observed a total of 9 trails which were attributable to the Leonids. These ranged in duration from 3 seconds to more than 2000 seconds and appeared to fall into two groups, five with durations of 10 seconds or less and the other four lasting 100 seconds or more. Also of considerable interest was the altitude distribution of the trails. The shorter ones were confined to below 88 km and the longer ones were not observed above about 97 km. This was somewhat odd at the outset because the Leonids are very high velocity meteors at 71 km/sec and would be expected to ablate and be deposited at substantially higher altitudes.

In an effort to better understand the measurements made by the lidar instrument, we have developed a model of the neutral metal trails from meteoric ablation and have computed the characteristics of the trails as they might appear in the lidar. The model was originally developed to investigate the altitude dependence of the occurrence frequency of the observed trails. However, it can also be used to estimate the range of meteor sizes that

can be observed with the equipment and to compute the average diameter of the observed trails as well as the expected durations.

The modeling begins with the computation of the line density of potassium assuming an ablation model identical to that proposed by *Love and Brownlee* [1991] and it is assumed that potassium metal comprises 0.025% by weight of the meteoric material. Values for the initial line densities are then computed for a given particle of diameter d assuming an out-of-atmosphere velocity of 71 km sec⁻¹ characteristic of the Leonids, a particle density of 0.6 cm⁻³ and an incidence angle of 39° from zenith. It is further assumed that ablation and trail formation is a constant function of altitude between 70 and 120 km. This assumption is the most benign in light of the large uncertainties in the structure, thermodynamics and atmospheric interaction of the meteoric particles.

The initial trail is assigned a characteristic radius equal to twice the altitude dependent mean free path λ , which represents 2-3 collisions before thermalization of the metal atom. The diffusion equation is solved for the time and space variation of the metal density, giving

$$n(r,t) = \frac{\Lambda_0}{4\pi} \frac{1}{Dt + \lambda^2} e^{-rt} e^{-\frac{r^2}{4(Dt + \lambda^2)}} \quad (20)$$

with Λ_0 the initial K line density and D the diffusion coefficient. It is assumed that the trail and the lidar beam are orthogonal at the center. The factor e^{-rt} accounts for chemical removal of the potassium with the altitude dependent rate r . The equation can then be integrated within the 50 m by 200 m dimension of a beam "cell" to yield the total number of K atoms within the cell, which is the observed quantity and which is to be compared with an approximate detection threshold of approximately 10 cm⁻³. Thus, a trail will be observable from its creation until the time that the number of atoms within the cell falls below the threshold.

In order to estimate the relative number of trails expected at a particular altitude, the distribution of particle sizes must be introduced. In this model, we have taken the distribution from the published total meteor numbers during the 01-05 UT window. The resulting distribution has a mass index of 1.71 below about 0.1 g but shows an excess of particles in the 0.1 and 5 g range, over and above the expected linear behavior.

With the mass distribution in hand, the weighted contribution to the number of trails at a particular altitude can be computed from the lifetime and the wind speed. The contribution of a particular particle at a particular altitude can be approximated by the product of the lifetime and the wind speed since the trail can be visible anytime during the lifetime, as defined above, and since trails will be swept into the lidar beam at a rate proportional to the wind speed. Figure 26 shows the computed probability of observing a potassium trail of any duration with the two different eddy diffusion profiles.

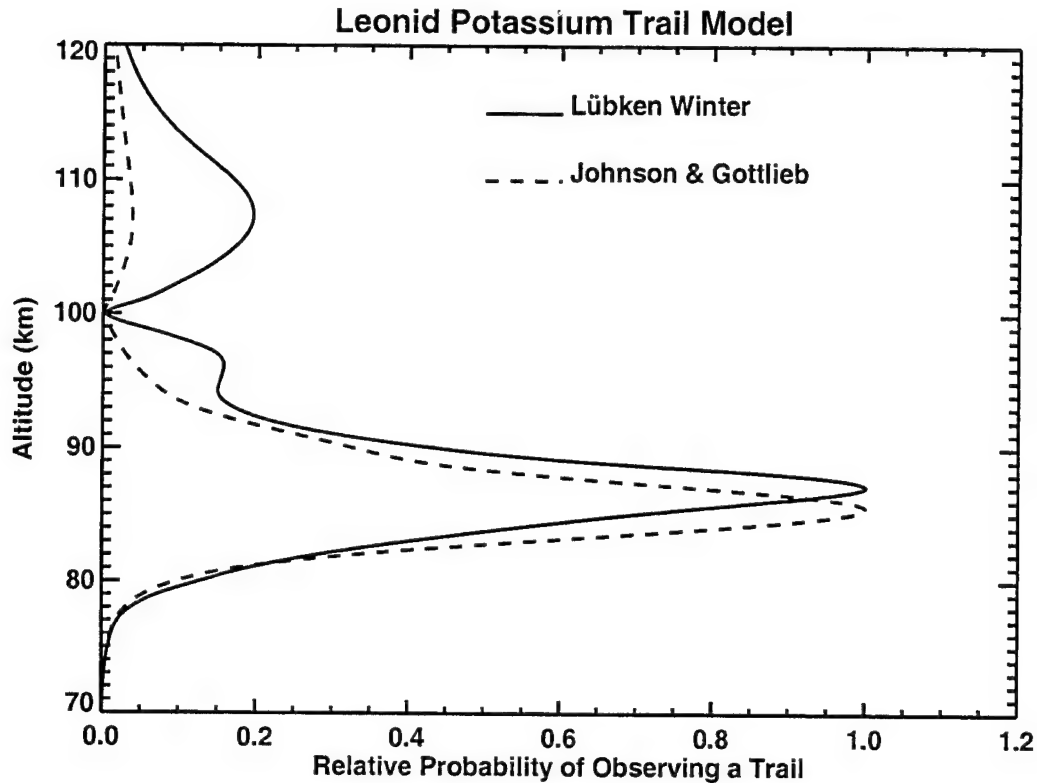


Figure 26. The computed probability of observing a potassium trail from the 1996 Leonid meteor outburst as a function of altitude for two formulations of the eddy diffusion coefficient.

Both profiles show the concentration of trails between the altitudes of 85 and 95 km which is evident in the measured statistics. Rapid conversion of the atomic K to molecular species defines the bottom side of the region in which detection is to be expected. The top side of the region is similarly defined by the rapid diffusing away of the trails. The model predicts that trails above the null in the wind, here at 100 km, would make up less than 10% of the total observed trails. Initially it appeared somewhat strange that there were no trails detected at high altitude, since considerable deposition by 70 km/sec dust can be expected above 100 km. It would seem, though, that diffusion at this altitude and above is rapid enough to dilute the trails so that only those arising from very large particles might be observed.

Although we do not attempt from this very limited data set to draw any conclusions about the distribution of particles on the Leonid stream that night, we can make some progress in discerning what sort of particles probably gave rise to the trails detected that night. First, we can compute the minimum particle size that would be visible in the lidar beam. The limiting factor here is the requirement that the signal must persist for something on the order of one second.

It turns out that for these model parameters, the limiting diameters at which durations of more than one second are never encountered are very close to 1 mm. At a density of 0.6 g cm^{-3} , this is $5 \times 10^{-2} \text{ g}$ and, according to Öpik's formula, corresponds for Leonids to a magnitude of more than +7. The prediction is, then, that the lidar can detect substantially smaller meteors than are observable visually, where the limiting magnitude is rarely much greater than +5.

The question then becomes whether the duration of the signal can be related in some way to the size of the meteoroid. This would be critical if the lidar were to be used to characterize shower populations. We have examined the duration of trails arising from various sized meteoroids as a function of the time of initial detection, t_i , after trail formation. Several things are evident, the first of which is that there is a strong dependence of duration on altitude. At 85 km, even the largest of the particles give rise to durations of only a few tens of seconds while at 95 km, the largest of the particles can create trails lasting several hundreds of seconds.

What is also interesting that the duration of a trail is reasonably constant, especially for trails from meteoroids of less than 10 mm, over the life time of the trail. This is in spite of the fact that density of the trail continues to decrease. Thus it would seem possible from these results to assign the trails with duration of less than 10 seconds to meteoroids of less than, say, 3 mm. The longer trails, with durations of several hundred seconds, would seem to have arisen from meteoroids the 10-20 mm range and would not have occurred at 85 km, presumably because chemical removal dilutes the trails too rapidly. Of course, the calculated duration is strongly dependent on the many assumptions of the model, as it is on the assumed detection threshold and on the wind speed. Still, the clear relationship between size and duration, irrespective of when the trail was deposited, gives at least some hope in relating the measurements to the shower population. We add that there is other information available, namely the measured number of K atoms in the lidar beam, which in the future could provide additional characterization of the size distributions.

We have also computed the probability for detecting a trail of a particular duration. This is shown for one case at 85 and 95 km in Figure 27a. The low altitude curve shows a peak at 8 sec and a second one at 200 sec while the higher altitude curve peaks at 20 and 3000 sec. The secondary peak is apparently due to the non-linear behavior in the mass distribution. Although these curves support the altitude variation of the trail size and although the secondary curve at 95 km is certainly interesting in light of the observation of two "populations" of durations what we find more interesting is the fact that there is considerable probability of observing trails of any duration. The same result is obtained when we examine the relative contribution of particles of a given size to the total number of trails (Figure 27b). This curve is nearly flat, that is, within a factor of three at most, from the threshold to the largest particles expected. This is a result of the increasing lifetimes for the large meteoroids coupled with the fact that they are less numerous. This suggests that the lidar samples the size distribution uniformly rather than in proportion to the number of particles present.

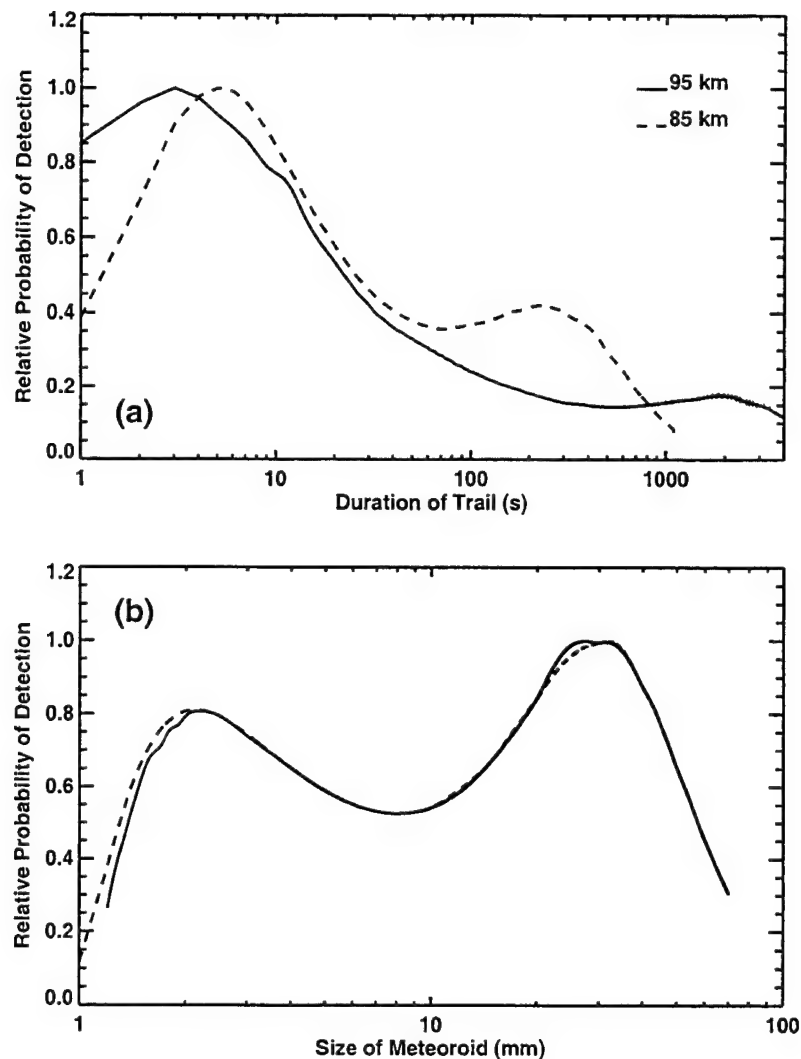


Figure 27. Relative probability of detection (normalized to the maximum of the probability) vs. duration of a trail (panel a) and size of a meteoroid (panel b). Solid lines apply to 95 km and dashes to 85 km.

7.4 GLO-I DATA ANALYSIS AND MODELING

The GLO-I experiment was carried out in October of 1991 from the space shuttle. In the dawn/dusk shuttle orbit, the instrument recorded radiances from metal species at various tangent heights. The line-of-sight approximately crossed the terminator near the magnetic equator and near local noon in the northern polar regions. Measurements were made of the metal species Mg^+ , Ca^+ , Mg and Na . This experiment both confirmed several earlier observations of thermospheric metals, in a unique way, and discerned several new features which were previously unknown. This preliminary GLO experiment has been followed by five others, the latter experiments using improved technology and multidimensional imaging. These data sets will be important in future work. In fact, the

GLO program was the primary motivation for initiating this modeling program some four years ago. We have presently completed our modeling of GLO-I and we briefly review here some of the features of the data set which we have successfully modeled. The variety of the results should illustrate the need for versatile models in this work.

The GLO-I experiment provided several unique observations. Those which we have treated theoretically can be enumerated as follows:

- (1) There is a strong asymmetry in the density of metallic ions at high altitudes near the magnetic equator. On the dawn side, there are almost no ions, while there are often many at dusk.
- (2) The densities of calcium and magnesium ion in the thermosphere appear to parallel each other very closely.
- (3) There is a great deal of neutral sodium at high altitudes, which is surprising at first glance because the neutral species cannot be transported there directly through electric fields or winds.
- (4) Neutral and ionized magnesium were observed in the thermosphere simultaneously.
- (5) The equatorial crest has been observed in the thermosphere at dusk and shows roughly a two-peaked maximum at $\pm 20^\circ$ magnetic latitude.

The dawn/dusk asymmetry of magnesium ions had been treated previously in *McNeil, et al.* [1996] and we need not discuss that aspect further here. The second observation, that Mg^+ and Ca^+ follow each other quite well arises as a prediction of our model and the relative abundances of the two species in the thermosphere have been found to closely match those predicted by our models. This is also equivalent to their relative meteoric abundances, since our models find calcium and magnesium to behave very similarly, both in regard to ablation and to chemistry.

The finding of a large radiance from neutral Na at high altitudes was quite remarkable, since there is no reasonable way to transport the neutral species upward from where it is deposited. Radiances were found to often in excess of 100 Rayleighs in the regions above 200 km. It is also found that the neutral sodium has a strong dawn/dusk dependency similar to the ionized metals, although not as pronounced. We have developed comprehensive models similar to that for magnesium, described in *McNeil, et al.* [1996] for sodium. These models appear to explain the presence of neutral Na quite adequately. The metal is transported upward in the afternoon in the form of Na^+ through the Earth's equatorial electric field, just as is Ca^+ and Mg^+ . At high altitudes, Na^+ can only be neutralized only through radiative recombination



Although this process is relatively slow, it creates neutral sodium at very high altitudes and over an extended period of time from noon to dusk. These neutrals effectively "rain down" through the thermosphere, giving high concentrations of neutrals on the dusk side. We show in Figure 28 the prediction for sodium neutral dayglow for both the dawn and dusk

thermosphere. We see that the model predicts both a strong dawn/dusk asymmetry and a sodium radiance exceeding 100 Ry on the dusk side. It should be remembered that these models all derive from a common influx rate of meteoric material. They therefore are self-consistent between metal species. It should also be noted that they produce reasonable values and characteristics for the permanent metal layers in the mesosphere.

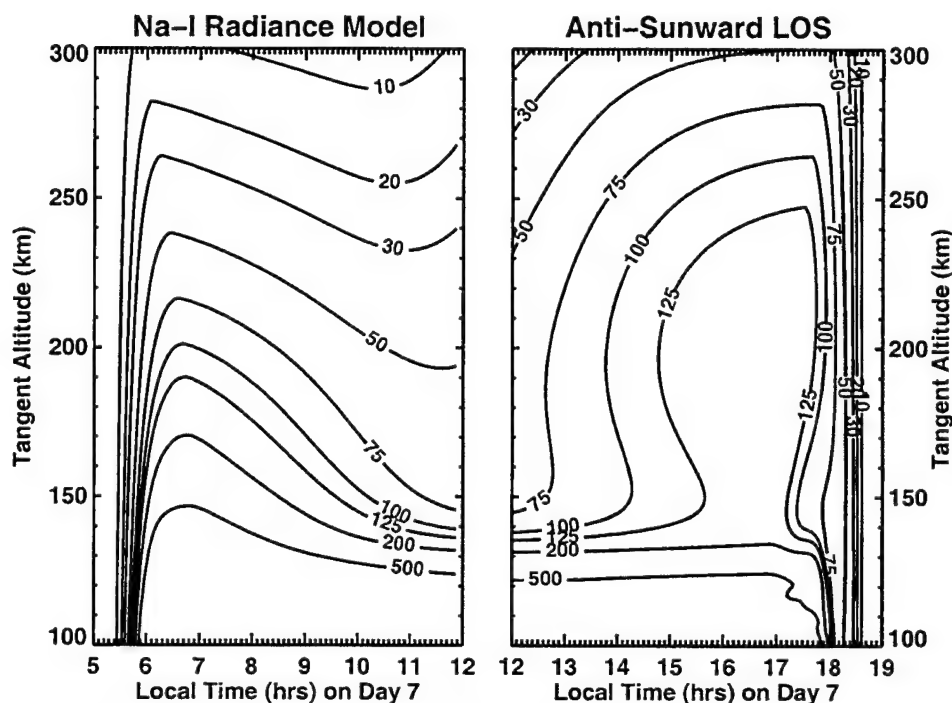


Figure 28. Predicted radiances from neutral Na due to solar scattering on the geomagnetic equator near the dawn side (left) and the dusk side (right) of the terminator.

The simultaneous observation of both the neutral and ionized species of Mg was interesting in that it allowed us to directly test our model in both neutral and ion. There were a total of eight spectra in which neutral Mg could be discerned. Generally, the signal is too weak at high altitude to be differentiated from background. When compared to the models, we found agreement to within a factor of two for the neutral and ionized metals above 200 km. This is quite reasonable, all things considered.

Finally, an attempt was made to characterize the equatorial anomaly crest as a function of geomagnetic latitude. The problem is complicated by the fact that GLO-1 did not always look at the same tangent height. It is also complicated by the fact that the anomaly is sometimes substantially more pronounced above the equator, sometimes below, and other times with relatively equal metal densities. This has been attributed to variations in the meridional winds. We selected all complete GLO-1 dusk passes and found that all of them showed at least a northern or southern anomaly. Because of the limited data, we made no attempt to separate these, but simply binned each into latitudinal divisions and selected

both the median radiance value and the 90th percentile radiance value for comparison with the model. These are shown in Figure 29. Remember that these do not always represent the same look altitude, but all are greater than about 250 km.

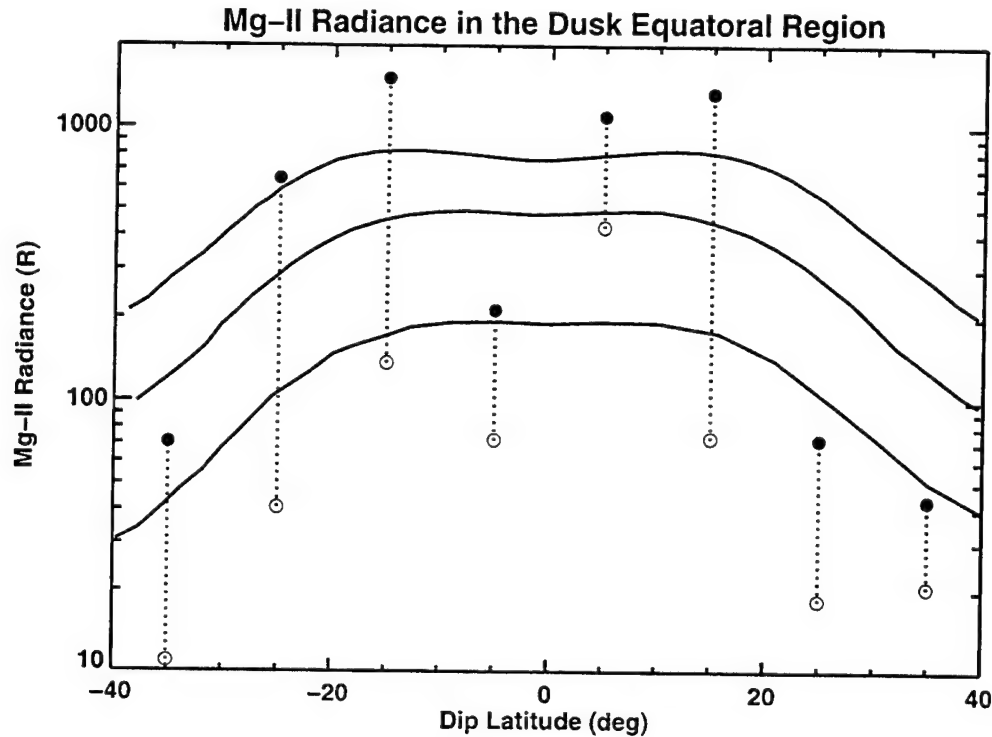


Figure 29. The dusk equatorial anomaly crest, expressed in terms of Mg^+ radiance, as a function of latitude as measured by GLO-I and as modeled. Measurements are expressed as median (open circles) and 90th percentile (filled circles) radiance values in 10° bins. The model is evaluated for tangent altitudes of 250, 275 and 300 km.

The model is evaluated with consideration of the changes in vertical transport due to latitudinal variation in the electric field as well as changes due to the change in the dip angle of the magnetic field. Changes in the background ionosphere are not included, which could potentially weaken the radiance at higher latitudes as well as in the trough region itself. The present background ionosphere model in use, IRI, does not have a good representation of the anomaly crest in any case.

In spite of the logarithmic scale, the model appears to predict a relatively substantial anomaly crest in the metal radiances. This is somewhat surprising since the development of the crest is often assumed to require two-dimensional treatment in which motion along the magnetic field lines is accounted for. This model allows for only vertical motion. An interesting result not shown here is that the model predicts that the density increase, seen at dusk at the equator, moves closer to local noon as the magnetic latitude increases. Data on the local time behavior of the anomaly is available from the subsequent GLO missions and it will be interesting to investigate this behavior more thoroughly in future work.

8. ANALYSIS AND VISUALIZATION FOR IONOSPHERIC MODELS

Graphical interfaces have been designed for several ionospheric and atmospheric models allowing a user to easily run the model and visualize the results. The Parameterized Ionospheric Model (PIM) User's Display (PUD) package, originally designed to display only data from the PIM, has been integrated into GEOSpace allowing the user to visualize PIM results in 3D. The PUD software package has since been upgraded to include data from the Wideband Model (WBMOD) and various ray tracing algorithms and is now known as the Ionospheric Modeling/Analysis System (IMAS). The IMAS look-and-feel was used as the starting point for a separate visualization tool for the Artificial Satellite Analysis Program (ASAP) developed for possible future integration into GEOSpace. The same was done for the Voice of America Coverage Analysis Program (VOACAP), an HF propagation tool.

8.1 IONOSPHERIC MODELING/ANALYSIS SYSTEM (IMAS)

8.1.1 PIM

A beta release of the PIM User's Display (PUD) was completed and integrated into the GEOSpace package. Version 1.7 of PUD has been documented, thoroughly tested, and delivered to AFRL. It includes features which allow the user to set the minimum-maximum range for any 3D PIM plot, as well as the individual step values for frequency and elevation on a ray trace display. The PIM data file to be displayed is specified on a GEOSpace command line and directly passed to the PUD process where it is loaded and ready for viewing upon startup. Once loaded, the data file may be saved and recalled at a later time. Printouts are also available. Figure 30 shows an example of the PIM foF2 plotted at 00:00 UT on 07/06/98 with the PUD software.

An interactive HyperText Markup Language (HTML) online help system was also added to the PUD software which includes graphic descriptions and anchors to documentation on various features of the models. These HTML files may be viewed through any standard browser such as Netscape or Microsoft Explorer.

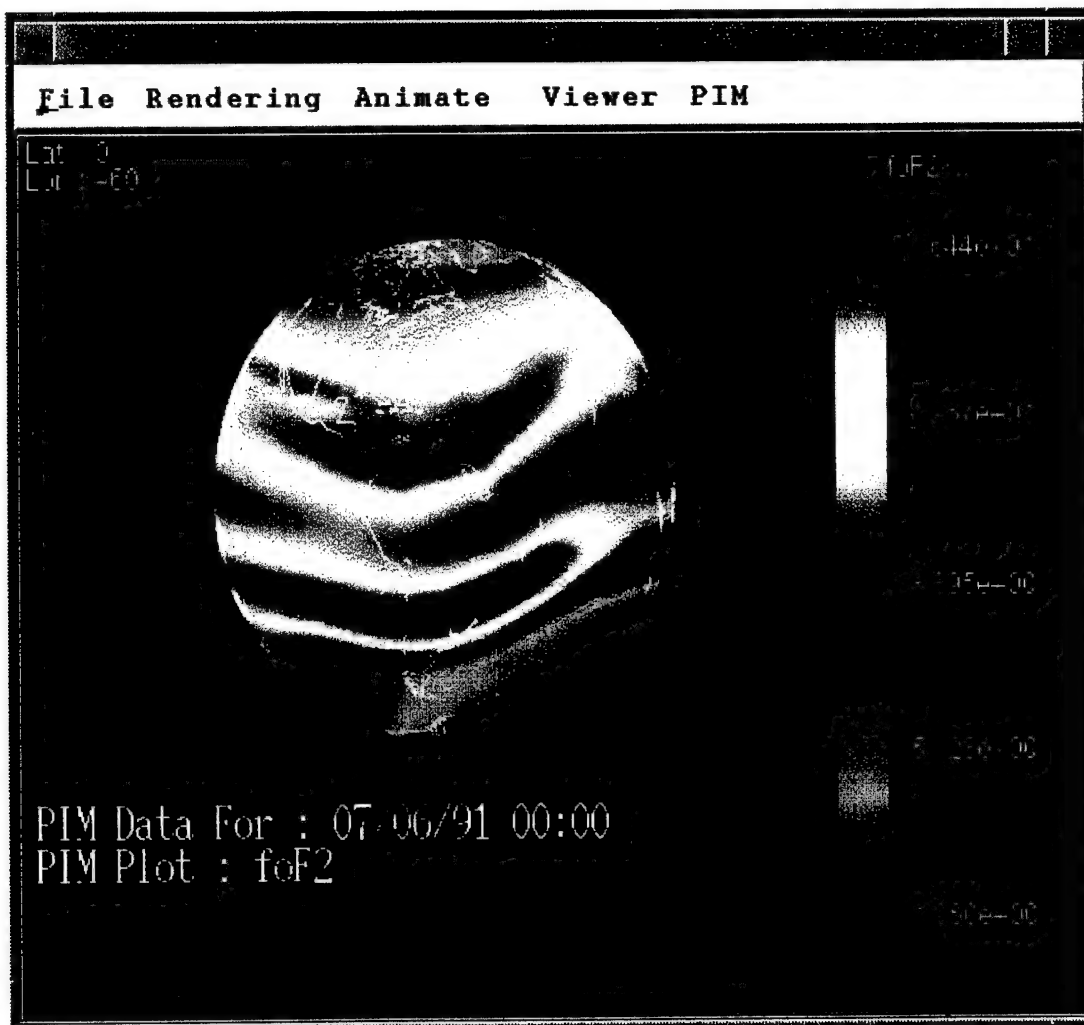


Figure 30. PIM foF2 is shown at 00:00 UT on 07/06/91 with the IMAS software in GEOSpace.

8.1.2 WBMOD

Since the completion of Version 1.7, additional features have been added which allow a user to run WBMOD based on the user selected input values for the Julian date, K_p , Sunspot Number (SSN), and satellite selection. A range for the Universal Time (UT) may be specified as well. The WBMOD results may then be viewed on the 3D Earth display just as the PIM data. Once the data have been loaded, the WBMOD user inputs may be saved to a file for recall at a later time. The current software can display S1, S4, percentage of time, and PRMS. Additionally, data may be displayed in a transparent mode making the continental outlines visible.

From the WBMOD interface, the user is able select a range of frequencies to include in the display. A slide bar in the plot window allows the user to step through each frequency at the specified delta. The WBMOD display also has the ability to show the position of the chosen satellite. When the check box labeled "Show transmitter" is activated, a transparent cone is projected from the satellite onto Earth's surface showing the area on Earth visible from the satellite. The user may select the "Orbit" option of WBMOD which will vary the transmitter location based on the orbital position and velocity of a satellite. While in this mode, the path of a specific satellite may be animated or its position viewed as a static plot at any particular instant.

8.1.3 Ray Tracing

In addition to WBMOD and PIM, 2D and 3D ray tracing algorithms have been incorporated into the PIM User's Display Software (PUD). These additions prompted a name change for the PUD software package to the Ionospheric Modeling/Analysis System (IMAS).

Because IMAS requires a latitude and longitude to associate a ray trace to the other parameters being graphically presented, software was developed to convert range distances from a radar station to latitude and longitude. With this, both the 2D Australian ray tracing algorithm and the Jones-Stevenson 3D ray tracing algorithm have been added to the IMAS package. An interface has been developed which will graphically display the results from both of these. When running the 2D ray trace, the user is free to select the appropriate range, azimuth, and number of hops for their analysis. An example is shown in Figure 31 where 2D ray traces for three selected frequencies are shown based on the PIM plasma frequency levels.

When selecting a 3D ray trace, a slide bar appears in the window while the ionosphere is being built updating the percentage which has been completed. The algorithms used for retrieving both 2D and 3D grids have been optimized for faster visualization. This 3D model also has the ability to calculate the elevation and azimuth angles required to communicate between two specified points for a given frequency.

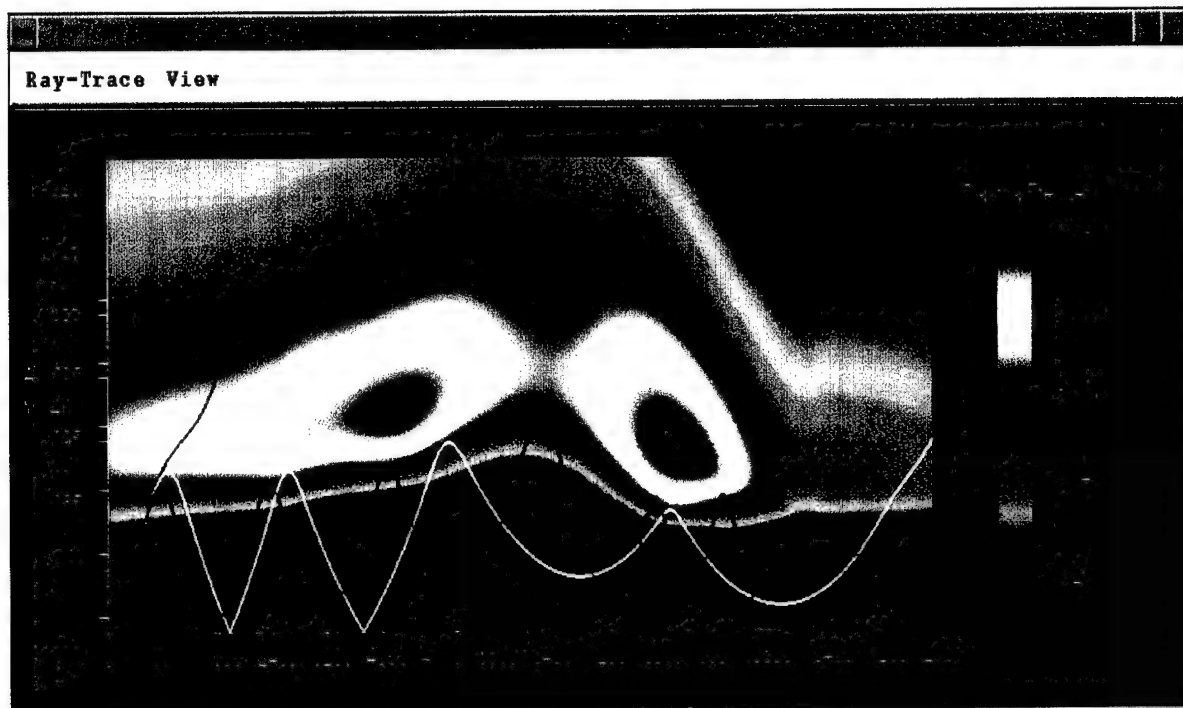


Figure 31. 2D Australian ray trace for three selected frequencies shown based on PIM plasma frequency levels. Image produced with IMAS software in GEOSpace.

8.1.4 Contouring Data System

A collection of IDL and FORTRAN routines has been integrated into the IMAS software providing the ability to contour data supplied in geomagnetic coordinates. The contour lines may be plotted in both geomagnetic and geographic coordinates. The system allows for both regularly and irregularly gridded source data. Contour plots may be produced for the following data sets in both geomagnetic and geographic coordinates: Hall Conductivity Model, PED Conductivity Model, H-M Model BC, Joule Heating Rate, Field-Aligned Current, Electric Field Magnitude, Ionospheric Current Magnitude, and Ionospheric Hall Current Magnitude.

An additional plot window was created to show the relationship between the density and altitude values in the currently active ionosphere slice. In addition, the foF2 and foE values are also plotted as selected by the user.

8.2 ASAP VISUALIZATION SOFTWARE

A visualization tool for the Artificial Satellite Analysis Program (ASAP), an ephemeris propagation program for orbiting planetary spacecraft, was developed using the look-and-feel of the IMAS software. This product will possibly be integrated into the GEOSpace package at sometime in the future. The program will load in satellite elements and graphically display an orbit showing the decay until the satellite touches down on Earth on a 3D globe display. 2D plots are available for the apogee and perigee of the satellite as a function of altitude and time as well as the $F_{10.7}$, K_p , and C_d A/m, each which may be changed by the user.

8.2.1 MSIS Atmospheric Density Model

The MSIS atmospheric density model was integrated into the ASAP Visualization Software package. Access to the output of the MSIS model is available through the Thermosphere Forecast Model plotting options pop-up. An option is also available to view the differences between the Jacchia and MSIS models either as an orbit path or as a shell of data around the globe. Additionally, two separate 2D plots showing the apogee and perigee of the selected satellite allows the user to analyze the impact of the atmosphere on the time of impact and orbit decay. Any single orbit may be displayed versus time in a separate window to detail the change in the altitude of the satellite while in orbit. Pop-up windows are available to adjust the A_p and the SSN values used by the atmosphere models.

8.3 VOACAP

The Voice of America Coverage Analysis Program (VOACAP) is a version of the Ionospheric Communication Analysis and Prediction (IONCAP), modified for increased accuracy of area coverage analyses. Like IONCAP, VOACAP is a text based application. A graphical interface has been developed for VOACAP giving the user the ability to both run VOACAP and view the results. This graphical user interface (GUI) is intended to be used with IMAS and GEOSpace. Rather than imbedding the graphical code directly into the VOACAP code itself, the GUI makes a system call to run VOACAP based on the selected inputs.

8.3.1 Development of Graphical User Interface (GUI) for VOACAP

The most recent version of this work in progress, contains the same main menus as given in GEOSpace, "Admin," "Execute," and "Data." These have been named to conform with GEOSpace in the event this software is to be integrated with the GEOSpace package. Through options in these menus, the user can alter most settings necessary for a VOACAP run. Currently input files may be read and saved via the first menu item, "Admin". All files

are handled through the dialog box allowing freedom with directory selection and file naming conventions. By selecting the "Data" menu, the user may select to change transmitter and receiver options. Multiple antennae may be selected (up to 30 at either location), although the GUI does not have processing to check for invalid antennae input. Other options, such as latitude and longitude may be selected as well. A variety of general settings, including date, frequencies, sunspot number, required reliability, method, etc., are to be set by the user and may be saved for reuse at a later time.

8.3.2 PIM Input Files

VOACAP has been modified to allow for the processing of the PIM ionospheric output files. The user may select to read in a PIM file rather than using a standard CCIR or URSI ionosphere. It should be noted that the PIM input in the GUI looks for file name root, not an entire file name. The format is ROOT_DATx. VOACAP has been edited to accommodate this feature. The ROOT name is up to the user, however, the name "NONE" is not acceptable. VOACAP suffixes "_DATx" to the ROOT where x is the hour specified in the PIM data file. This makes file handling compatible with PIM outputs in GEOSpace.

8.3.3 Graphical Results from VOACAP

There are currently two graphs available with the VOACAP GUI. The first displays the maximum usable frequency (MUF) over a period of 24 hours. The voaf_gui_input.config file allows the user to change minimum and maximum frequencies to be displayed. The default frequency range when graphing VOACAP MUFs is set from 0 to 50 MHz. In addition to the MUF, the Signal-to-Noise Ratio (SNR) is displayed with a colored contour throughout valid frequencies over the entire time period. This option may be turned off by the user.

A second plotting method allows the user to graph the SNR at a certain frequency (given at run time) over a 24 hour period. Either plotting method will accept less than 24 hour period of data to be graphed in the event the full data set is unavailable.

9. SPREE AND CHAWS DATA ANALYSIS

9.1 SPREE DATA ANALYSIS

The STS Mission Rehearsal Joint Integrated Simulation (JIS) was attended in support of SPREE, 6-9 Feb 96. Final preparations were made to support the launch on 22 Feb 96. A 9.0 GB disk drive, an 8 mm tape drive and an RGB printer interface box were shipped to Marshall Space Flight Center (MSFC), AL, along with blank 8 mm tapes and other necessary supplies. This equipment was added to the existing GSE configuration upon arriving at the Huntsville Operations Support Center (HOSC). Support was provided for SPREE GSE hardware and Realtime Display Software for the duration of the STS-75/SPREE mission. Tasks performed were the archival of all Realtime (RT) and Playback (PB) Orbiter Downlink (OD) data; finding and recovering gaps in the OD data set; maintaining data flow to the SPREE Realtime Display Software, and the archival of all processed data files and log status files.

The XY Plot display process was completed for use during the SPREE real-time operations. The display allows the user to plot the values of two data parameters against each other over a specified time span. The user may write the data values of the currently displayed plots to an ASCII file.

The SPREE flight display software was released for use at the MSFC during the STS-75 shuttle flight, launched 22 Feb 96.

9.1.1 SPREE Post-flight Data Support

All equipment sent to MSFC to support the STS-75/SPREE mission was returned to Phillips Lab (now Air Force Research Laboratory, Hanscom AFB) and was reconfigured to support the SPREE post-flight data processing and analysis. The shipping occurred after the impounding of equipment and data relevant to the tether breakage investigation had been lifted.

The Realtime (RT) and Playback (PB) Orbiter Downlink (OD) files were merged to create a contiguous set of all the raw OD data collected during the STS-75 mission. This data was reprocessed through the PCDECOM software to generate the files which were used with the SPREE post-flight data analysis software. Two 9.0 GB disk drives were temporarily added to GPDSEVER to facilitate the OD merging portion of the STS-75/SPREE post-flight data processing. The merged raw data files were compressed and written on an 8 mm tape. The format of the SFM data base files reading routines were appropriately modified, and the display processes requiring these new values were updated to access them.

The SPREE Flight Data Recorder (FDR) #1 duplication process was completed and the tape was received for processing. FDR data segmentation processing was completed. There were no anomalies in processing the tape recorder, and all data was released for further processing.

STS-75 SPREE FDR data base files were installed and the data base lookup tables were modified. Analysis of FDR performance showed nominal results, which were similar to those of STS-46 with the exception of the FDR unit #1 write errors.

A three-second orbiter thruster offset was found to be introduced during the merging of the three orbiter downlink telemetry streams. The existing PATH data base was corrected by re-merging the time-tagged thruster information from the GNC orbiter downlink stream. The revised PATH data base was then verified through correlation of thruster firing events with known SPREE data responses.

9.1.2 SPREE Interactive Data Analysis Tool (SIDAT)

Postflight SPREE Interactive Data Analysis Tool (SIDAT) software was updated to include many of the new processes added for STS-75 real-time operations. New displays include SmartFlex Status Display, TSS Monitor, SPREE Command Echo Display, and the XY Plot Display. The STS-46 real-time SPREE and other information data base files were converted into the same formats as used for the STS-75 real-time data base files. This allows for a single version of the SIDAT software to access and display SPREE data from both STS-46 and STS-75 flights.

The post-flight version of the Attitude display process was enhanced to include the additions used during STS-75 real-time operations. These include the Tethered Satellite, tether line, deployment boom, graphic objects to the orbiter depiction and the integration of the tethered length information from the SmartFlex data.

Two forms of TSS Event Display were developed which present a time history of occurrences relating to the TSS circuit operation, in a form similar to the Orbiter Event Display. Parameters being tracked include TCVM Current Monitor values, four TCVM resistor relay switch states and the DCORE EGA unit firings.

All SIDAT graphical display processes were updated to take advantage of a new coloring feature. A checkbox labeled "invert" was added on the SIDAT command bar to work with the "Color/Gray" selection. Four possible colorings of the graphical displays are now possible: color-on-black, color-on-white, grayscale-on-black, and grayscale-on-white.

The ASCII file writing feature, common to many SIDAT display processes, was enhanced to include a printer specification, allowing all SIDAT software installations to take advantage of the software-driven file printing capability.

The newly developed TSS Circuit display depicts the TSS-1R electricity-generating circuit. Parameters from the SmartFlex data base are used to show the circuit switch settings, electron gun activity, and current and voltage measurements. The TSS Circuit display was enhanced with the addition of a "TSS Monitor" window. This allows one to view some of the same data values, but in a different format. This feature works in both the "Survey Slave" and "independent" modes of the TSS Circuit display.

The Line Graph sub-process of the SIDAT ESA Data Display process was enhanced. The option to alter the Y-axis data scale limits specifying the upper and lower exponent values allows one to closely examine small trends not readily visible when plotted in the fixed Y-axis data scale limits.

At the request of the researcher, several new CD-ROM disks containing the SIDAT software and STS-75/TSS-1R deploy phase data were produced. Several minor enhancements were applied to a few of the data display processes prior to the CD-ROM generation. The startup script used in determining the operating system version was also updated.

9.1.3 Spacecraft Particle Correlation Experiment (SPACE)

Spacecraft Particle Correlation Experiment (SPACE) FDR data base files for STS-75 were processed to generate their associated FFT data base files, using programs developed for the STS-46 flight data. Also, data spikes were removed, bit roll-over errors were corrected, and the normalized amplitude spectrum was obtained.

The SIDAT SPACE data display programs were updated to correctly annotate the high frequency (HF) bands from either flight (STS-46, 10, 2.5, and 0.625 MHz, and STS-75, bands were changed to 10, 10, and 5 MHz, respectively). The SPACE HF FFT data base files were regenerated, due to a slight change in the processing method.

An update of the SIDAT software and data was generated for the Principal Investigator of SPACE, Dr. Gough. The seven tape set includes the current version of the SIDAT software, the STS-75/TSS-1R and the revised STS-46/TSS-1 data base files.

9.1.4 STS-75/TSS-1R RELBET Generation

The generation of the STS-75/TSS-1R RELBET data base required extensive investigation. Using the data available during the TSS-LR deployment phase, comparisons were made between the state vector-generated orbiter to satellite position and the orbiter "snap" radar range information. Analysis revealed several problems regarding the timing of data values and periodic discontinuities in the orbiter attitude. The orbiter state vectors were also found to have several updates during the deploy sequence, causing more data disruptions. New orbiter state vectors were generated by interpolating between Keplerian orbital elements.

TSS state vectors were reconstructed from the revised orbiter state vectors, regenerated orbiter attitude values, and smoothed "snap" radar range targeting information. A document fully describing the investigation and generation of the STS-75/TSS-IR RELBET data base was delivered in November 1996. The STS-75 PATH files were reprocessed to include the new TSS RELBET information and to correct orbiter information anomalies observed during the RELBET investigation. Periodic discontinuities in the orbiter attitude values were resolved with the regeneration of the orbiter LVLH matrix from the state vectors. Several values related to orbiter position and/or attitude were recalculated, such as the magnetic field vector and ram angles. TSS state vectors and range information values were replaced with those calculated for the RELBET data base. The revised PATH files were reinstalled as part of the STS-75 SIDAT data base.

9.2 CHAWS DATA ANALYSIS

The Charging Hazards and Wake Studies (CHAWS) experiment is a plasma diagnostics instrument for investigation of the interaction between large bodies in Low Earth Orbit and smaller bodies in their plasma wake. CHAWS was flown as a collaborative experiment on the Wake Shield Facility (WSF) on Space Shuttle missions STS-60 and STS-69. The Wake Shield Facility (WSF) is a 12-foot diameter, stainless steel disk designed to generate an "ultra-vacuum" environment in space within which to grow thin semiconductor films for next-generation advanced electronics. The improved understanding of spacecraft environmental interactions derived from CHAWS results will enhance the utilization of space.

The CHAWS experiment consists of two sensor units and a controller. The sensor units are equipped with a series of compact particle detectors known as digital Retarding Potential Analyzers (RPAs). These small devices are capable of counting individual ions in the plasma stream. From these sensors, the composition, temperature, and flow direction of the plasma stream can be measured. Each RPA detector has been subdivided into two or four "channels", for a total of 16 subdivisions. The subdivisions allow for the particle flux direction vector to be derived from the channel count ratios.

Three RPA detectors are located on the ram side of the WSF, housed in a box with the center detector aperture perpendicular to the WSF surface and the inboard and outboard detectors canted at angles of +40 and -40 degrees from the center detector, as seen in Figure 32.

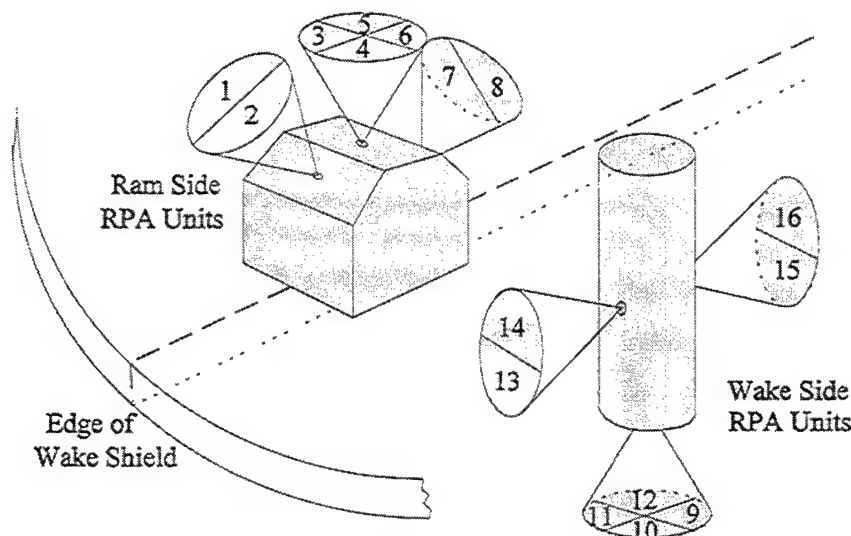


Figure 32. CHAWS instrument and detector fields of view.

The three RPA detectors on the wake side are integrated into the Langmuir Probe cylindrical housing. The center detector is located at the end of the cylinder and the inboard and outboard detectors are located midway on the side. Five current measurement points are also mounted on the probe; one at the tip, and four around the "waist". The Langmuir probe can be biased to high negative voltages to attract ions from the edge of the plasma wake. The densities, spatial distributions, and plasma parameters of the attracted ions can be determined using the data from the different detectors and knowledge of the orientation of the WSF.

9.2.1 Real-Time Data Processing

The collection and processing of CHAWS experiment data during on-orbit operations is vital to the project due to the lack of available on-board data recorders. With the availability of near real-time data, researchers are able to verify proper operation of the hardware and confirm the correct conditions are present for each procedure. The near real-time data also allows for the instrument operating mode to be modified in response to observed events, maximizing the scientific value of data gathered. The archival of all available data permits postflight reprocessing for the extraction of other parameters for correlation in the data analysis process.

CHAWS Orbital Monitoring Package (CHOMP) is a Ground Support Equipment (GSE) laptop-based CHAWS data monitoring system. It has been designed to process and display information regarding the health and status of the CHAWS instrument. CHOMP provides textual and graphical displays, enabling users to confirm sensor activity and

monitor performance. Although designed as a GSE program, CHOMP was also used on a laptop computer by the STS-69 crew during on-orbit CHAWS operations.

Two data streams are available from the NASA network connections. The ODRT (Orbiter Downlink, Real Time) stream is transmitted in real time at a rate of 128 kilobits/second during telemetry AOS periods. The ODPB (Orbiter Downlink, PlayBack) stream, recorded by the on-board orbiter telemetry recorders during LOS periods, is available from the NASA data center. When requested, the ODPB data is retransmitted by the data center at a rate of 192 kilobits/second, where the additional 64 bits contain voice data. Through the archival of both types of orbiter downlink streams, the most complete telemetry data base can be reconstructed.

PC-Decom is a PC-based software system that provides a user-defined interface to telemetered data. For the STS-60 and STS-69 Space Shuttle missions, PC-Decom was configured for receiving the NASA Orbiter Downlink data in both real-time and playback modes. Selected parameters for the orbiter, WSF and CHAWS are extracted from the 128-kbit real time data stream and displayed for telemetry monitoring. The 100% raw and "unpacked" orbiter, WSF and CHAWS data packets are relayed via Ethernet to the Sun workstations for archival and further processing.

The Listener software receives the orbiter downlink telemetry as transmitted by the PC-Decom software. The Listener software examines packets received from the network via UDP protocol, and selectively extracts those for the CHAWS, WSF and orbiter data streams, as defined by a configuration data base. Mission-specific routines perform extraction, processing and archival of data.

The Listener software places the data for each of the three types, CHAWS, WSF and orbiter, in separate shared memory segments, a standard Unix System V InterProcess Communication (IPC) facility. When a full frame of data is completed, the Listener software notifies the data display processes of the CHAPS software package, described in a following section, that new data is available for access and display in near real-time. The Listener software writes the processed data to the appropriate data base files. These data base files allow for limited data review capabilities during real-time operations through specific CHAPS display processes.

9.2.2 Postflight Data Processing

The merging of the archived ODRT and ODPB raw data streams collected during real-time operations produces a nearly contiguous data set of the mission events. This merged data set is used as the input stream to a modified configuration of the real-time data processing system to create the final CHAWS, WSF and orbiter databases. These data bases serve as the input to the CHAPS and CHUNKS data analysis software packages in the postflight environment.

9.2.3 CHAPS Data Analysis Processing

The CHAWS Analysis and Postflight Survey (CHAPS) software is a comprehensive collection of applications for viewing CHAWS data and associated space vehicle information in many different graphical and textual forms simultaneously. The CHAPS software, designed to operate on Sun workstations, uses a simple and self-explanatory user interface. Using standard Unix System V InterProcess Communication (IPC) shared memory segments and semaphore sets, each of the active CHAPS displays independently accesses and processes data from the shared data stream, producing the concurrent user-selected data displays for analysis. During real-time CHAPS operations, the data from the current CHAPS operations, as well as the related Wake Shield Facility (WSF) and Space Shuttle parameters, is viewed in real-time as received via the telemetry data provided by the Listener software, described earlier. Postflight CHAPS operations provide a master data control process, allowing the user to specify the time for surveying the available experiment data, and feature data display processes virtually identical to those used in real-time operations. While surveying the experiment data, the user may build and maintain a working data base of times of interest.

The command process panel, shown in Figure 33, is the main-level user interface for invoking all CHAPS display processes. The user simply selects the desired display process specified on the command panel buttons or pull-down menus. As each process invoked or exited, an informative message is displayed on the base of the command panel. Selected CHAPS display processes are described below.

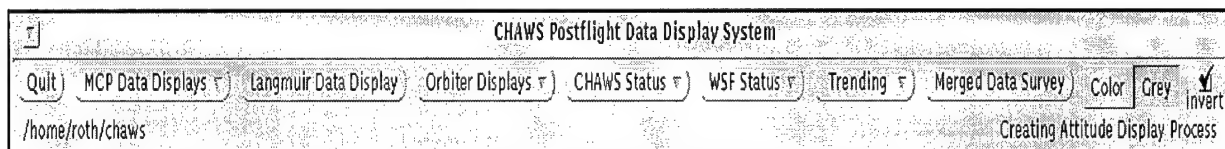


Figure 33. CHAPS command process panel.

The CHAWS MCP Data Display (as shown in Figure 34) presents three parallel color raster images of selectively summed MCP data from the ram or wake side apertures over the RPA steps, versus time. Each of the three data raster images may be configured to display data from one to several of the MCP units, in one of several calibration types. The configured summations may be displayed in Raw Counts, Count Rate, Flux or Density calibrations. Such raster images allow the user to perform qualitative data analysis. Associated line graph pullouts may be invoked directly from the color raster images, allowing the user to perform quantitative data analysis in parallel. The default configurations sums all MCP units of each of the three apertures on either side.

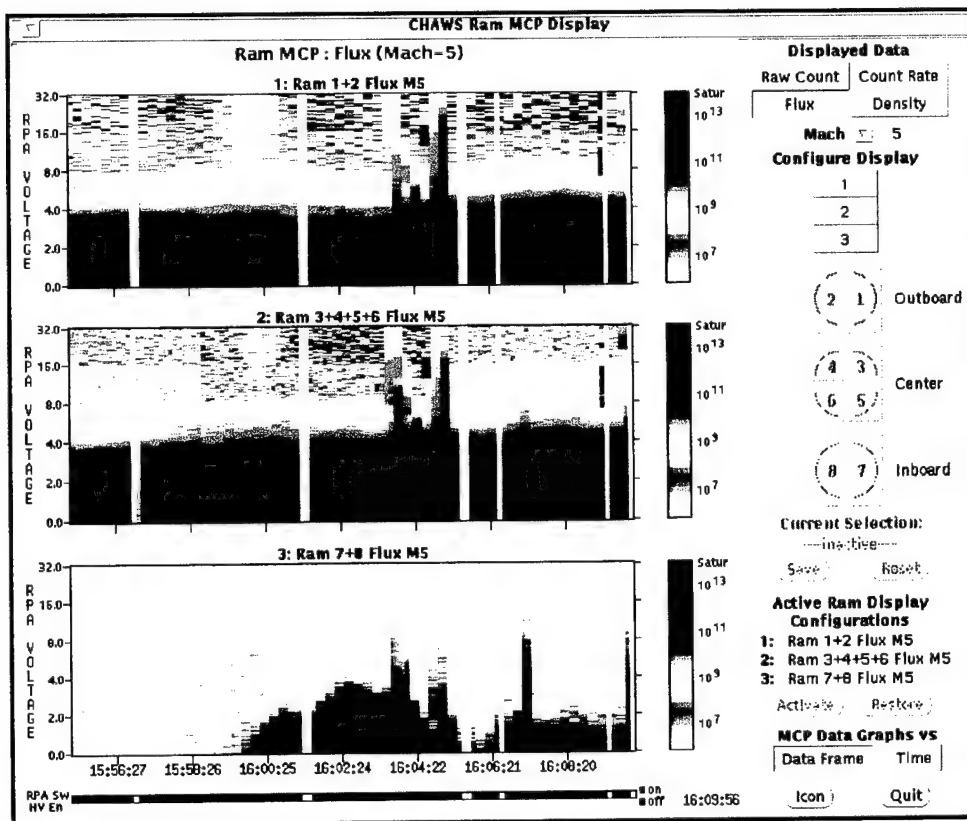


Figure 34. CHAWS MCP data display.

For each of the three MCP raster images, two types of line graph displays are available, "Data Frame" and/or "Time", for a maximum of six concurrent line graph displays. The user-selected line graph type is invoked by a mouse pointer selection on the data raster image. A "Data Frame" type line graph produces a plot corresponding to a vertical "slice" of the raster image at the mouse pointer position data time. A "Time" type line graph produces a plot corresponding to a horizontal "slice" of the raster image at the pointer position RPA voltage value, centered in a two-minute time span. The line graph display is described in more detail later in this section.

The CHAWS Langmuir Data display presents three parallel color raster images of data from the Langmuir probe. An example is shown in Figure 35. The first of these raster images presents a summarized form of the data from the eight MCP units mounted on sides and end of the Langmuir probe. The second presents the six Langmuir current values, and the third, the applied Langmuir voltage.

The raster images of the Wake MCP, current and Langmuir voltage provide a qualitative data analysis capability, showing the large-scale features of the data. The user may perform quantitative data analysis with the available line graph displays. Three concurrent line graph displays are may be activated, one for each of the Wake MCP, Current and Langmuir Voltage raster images. Each of these may be invoked using the mouse pointer

to directly select the data feature to be studied in detail. The mouse cursor, when over the raster image, will bracket a time slice of data to be plotted.

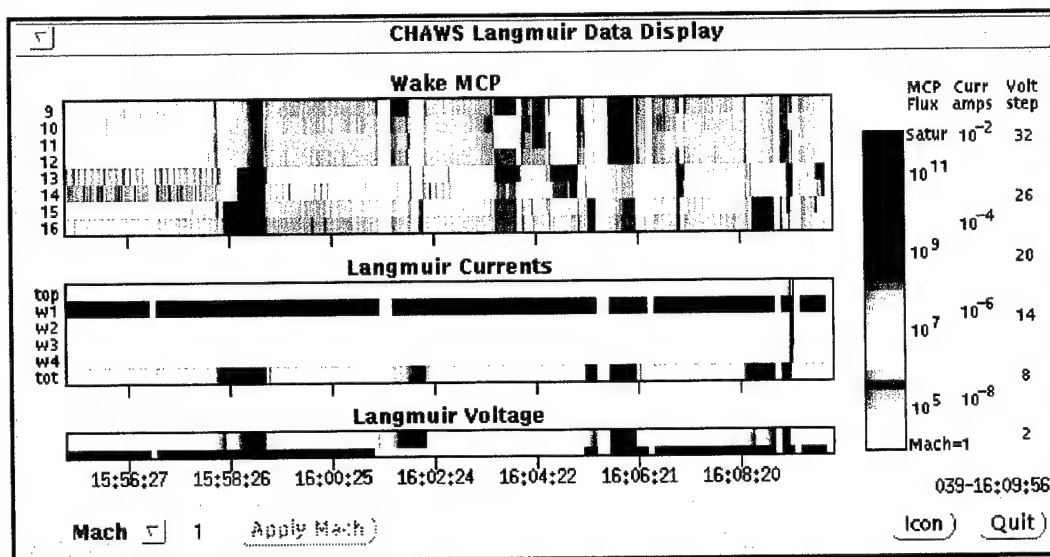


Figure 35. The CHAWS Langmuir data display.

The CHAWS Line Graph process displays the data from the CHAWS MCP or Langmuir Data Display processes in line graph form in a variety of forms, depending on the data and display type selected. In all forms, the user may examine each value plotted in the graph. As the user moves the mouse pointer within the line graph area, the value of the nearest plotted data point is annotated, along with additional information such as time, data frame clock cycle, RPA Step number, etc. Alternatively, the user may select to have all the information written to a specified ASCII file. This file may be viewed on-line, printed, or used as input to an external program.

The trajectory display, shown in Figure 36, depicts the current position and flight path of the orbiter on a world map with day/night terminators. The current latitude, longitude, altitude and attitude values are displayed numerically. The ram and B-field angles to the orbiter bay normal are calculated and also displayed numerically.

During real-time operations the downlinked CAS state vectors are used to construct an orbital element data base. In the postflight data analysis environment, the user may view the orbiter trajectory information in a "Survey Slave" mode or "Independent" mode. When in "Survey Slave" mode, the displayed orbiter information is controlled by the Merged Data Survey process, allowing the user to track the orbiter trajectory information in parallel with the CHAWS instrument data displays. In "Independent" mode, the user selects the time for the orbiter information display, and may view the sub-second thruster firing information. The user may also step the time of the orbiter information display forward or backward in various increments.

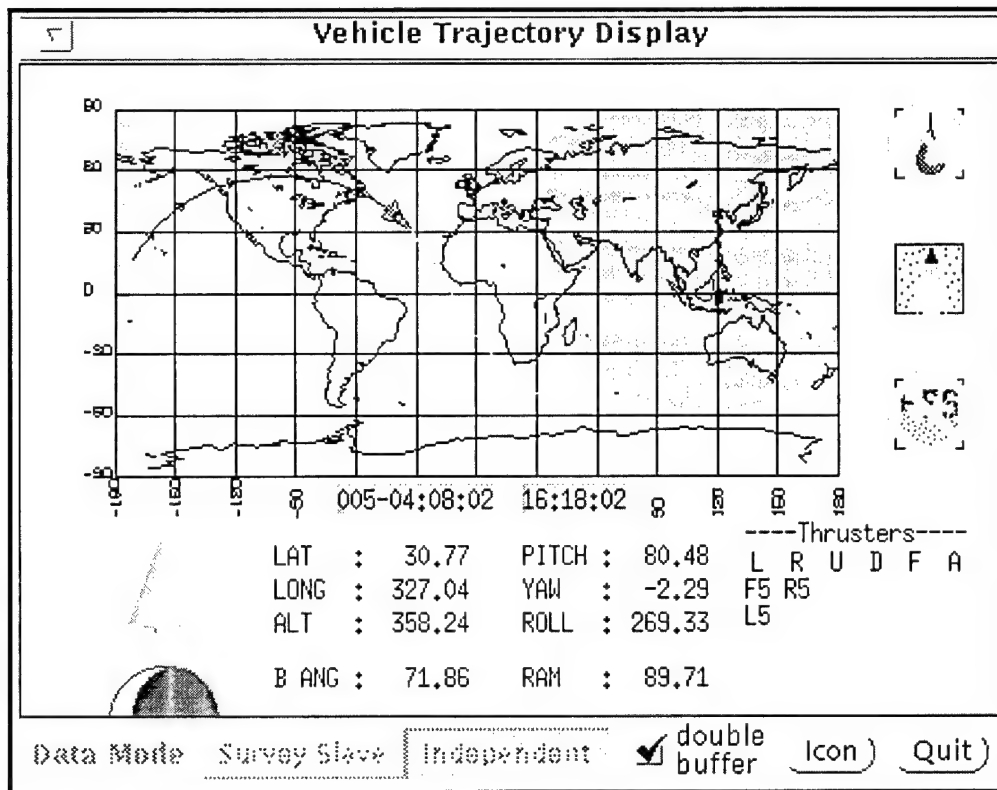


Figure 36. Trajectory display.

The attitude display presents a three-dimensional depiction of the orbiter in its current attitude. An example is shown in Figure 37. The positions of the orbiter RMS arm and the WSF are also drawn in their respective orientations and positions as indicated by the orbiter data. Small plumes, at the appropriate locations of the orbiter, are used to indicate thruster firings, water dumps, and/or FES usage. These orbiter events are also indicated through the use of icons and text. The current latitude, longitude, altitude, and attitude values are displayed numerically. The ram, sun, and magnetic field angles to the orbiter bay normal are also calculated and displayed. An indication of the orbiter being either "Sunlit" or "Eclipsed" is also displayed. The WSF status (*Stowed*, *Grappled*, or *Deployed*), attitude values, and range to the orbiter are annotated. The spacecraft charging effects value, $\vec{V} \times \vec{B} \cdot \vec{L}$, and the \vec{L} vector magnitude are annotated while the WSF satellite is grappled by the RMS arm.

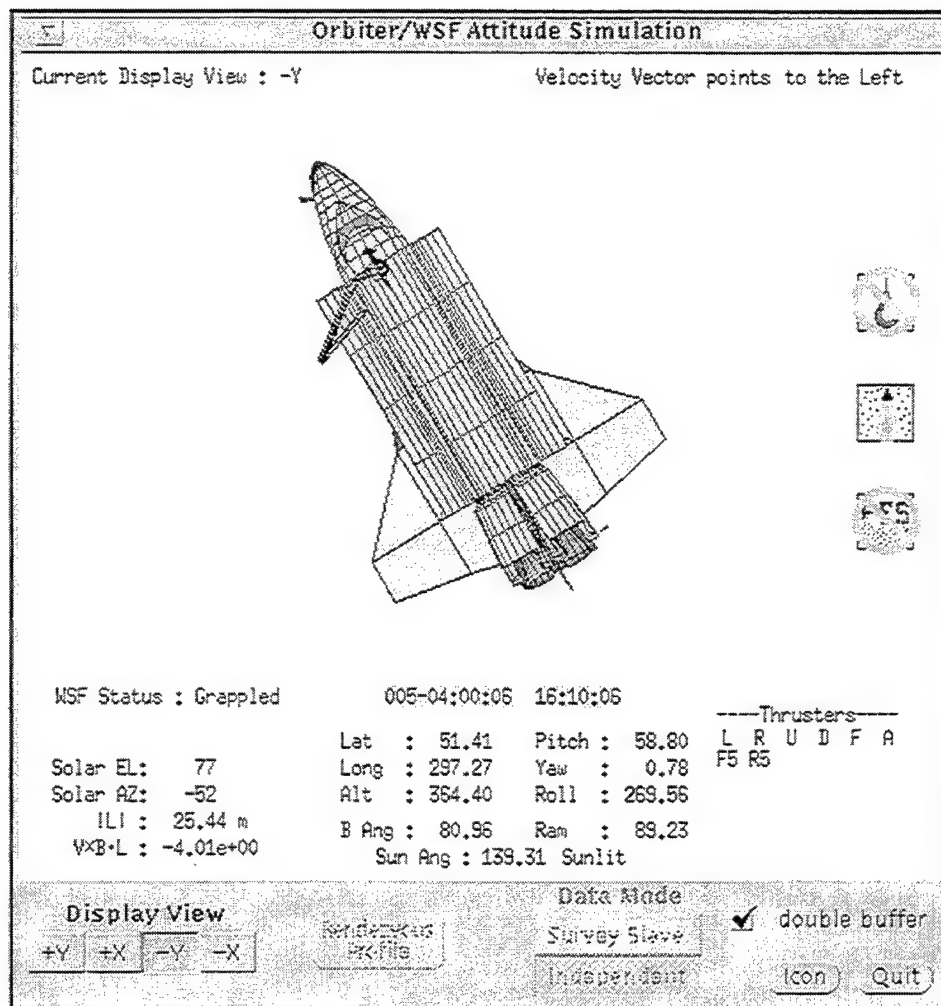


Figure 37. Attitude display.

The Orbiter Event Display process presents a time-based display of orbiter events. An example is shown in Figure 38. The orbiter thruster firings, water dumps and FES usage are presented in parallel rows, where the active events are indicated by blocks in the appropriate event row or rows. The Orbiter Event Display time scale is identical to those in the CHAWS MCP and CHAWS Langmuir Displays. An example of this window is shown in Figure 39.

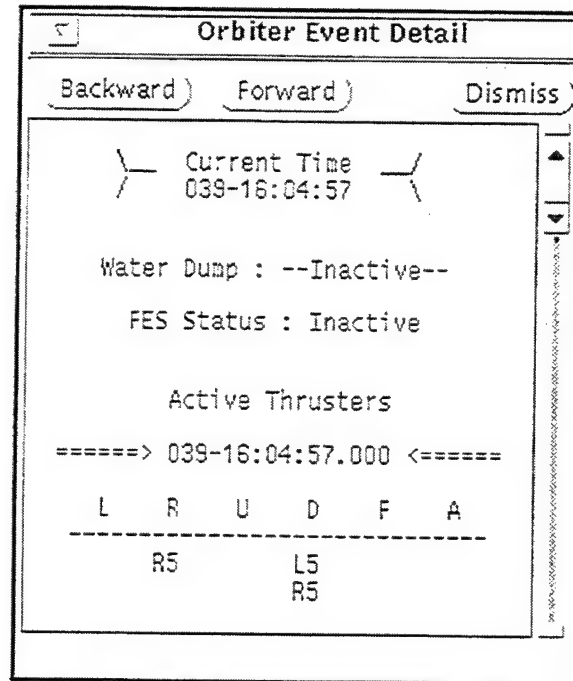


Figure 38. Orbiter event detail.

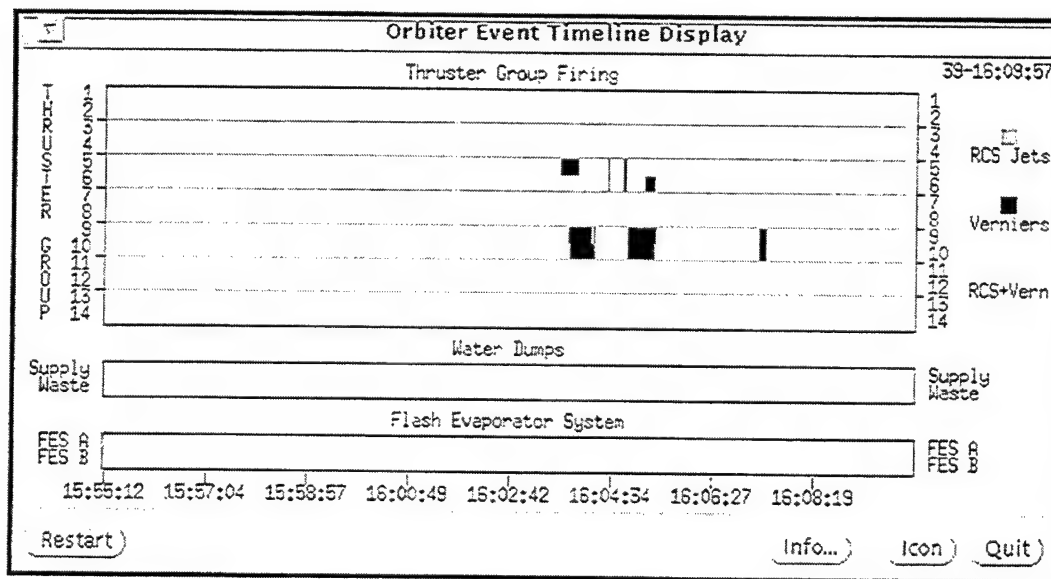


Figure 39. Orbiter event display.

The CHAWS Status Processes track changes in the CHAWS instrument operation. The current settings are presented in a scrolling text window (see Figure 40). When these logs exceed 400 lines, their contents are saved in ASCII files for future reference. The CHAWS System Status Process logs changes to the CHAWS instrument states, such as the DPU state, RPA state, HV status. The CHAWS Langmuir Probe Status Process logs detailed changes in the Langmuir probe status, such as the HV status, sweep status, and voltage sweep number.

CHAWS System Status Display								Icon	Quit
CHAWS Time DDD-HH:MM:SS	DPU	RPA	HV Command	HV Status	Langmuir Sweep	Ram MCP	Wake MCP		
039-15:49:46	on	on	enabled	off	off	on	on		
039-15:50:16	on	on	enabled	on	off	on	on		
039-15:58:04	on	on	enabled	on	on	on	on		
039-15:59:03	on	on	enabled	on	off	on	on		
039-16:01:09	on	on	enabled	on	on	on	on		
039-16:02:09	on	on	enabled	on	off	on	on		
039-16:05:14	on	on	enabled	on	on	on	on		
039-16:06:14	on	on	enabled	on	off	on	on		
039-16:08:57	on	on	enabled	on	on	on	on		
039-16:09:35	on	on	enabled	on	off	on	on		

Figure 40. CHAWS System Status display.

The Trending display allows the user to examine the CHAWS (see Figure 41) or WSF health and status values over time. For either data mode, the user selects one of the available data parameters from a scrolling list to be plotted as a function of time. The user specifies a starting time and time duration, producing the appropriate graph with an automatically scaled data axis. Once plotted, the user may alter the selections and generate a new graph, or may "edit" the currently displayed graph. The range of both the time and data axes may be shortened graphically using the mouse pointer, or the user may specify the minimum and maximum limits of the data axis. The Trending process window may be shortened, allowing multiple Trending displays with different parameters to be stacked for parallel comparison.

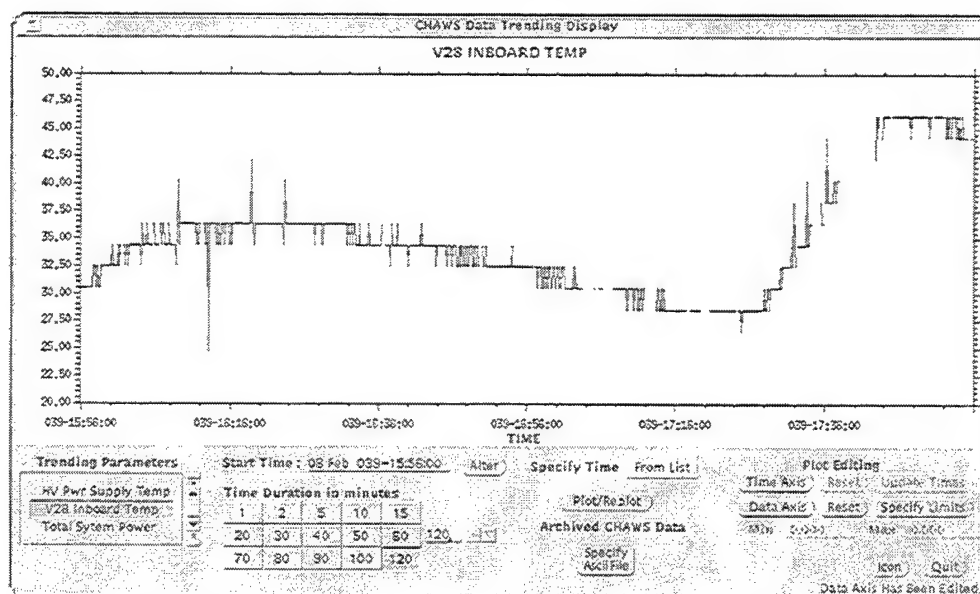


Figure 41. CHAWS Data Trending display.

9.2.4 CHUNKS

CHUNKS is an interactive or batch-mode program used to access the CHAWS data base files and produce ASCII files of tabulated data calculations and plot files. This program is meant to complement the capabilities of CHAPS by scanning the post flight data for correlations and computing physical variables of interest. The CHUNKS program uses the same calibration and calculation methods as used in CHAPS, maintaining consistency between the two packages.

The data base contains information describing the shuttle orbiter (CAS), the Wake Shield Facility (WSF), and the CHAWS experiment. The CHUNKS routines for reading these data base files are derived from and are compatible with those of CHAPS. The CHUNKS program marches through the data base, by stepping CAS GMT time, and checks to see if there is a matching WSF or CHAWS time. If so, it reads in the corresponding structure records. Selected variables can be extracted from the structures and printed out, along with various derived variables. All of the CHAWS structure variables are accessible, and selected variables are available from CAS and WSF. The CHUNKS program has been used extensively to survey the CHAWS missions and to test out algorithms, e.g. for the ambient density and temperature.

An input parameter file specifies the data parameters chosen to be extracted and manipulated. Up to five output files can be requested for displaying orbiter (CAS), wake shield facility (WSF), and CHAWS information. The CHAWS data records typically span 7.5 seconds and the information for this period is designated as frame data. Each frame contains data for the 160 channel micro-channel plates (MCP), which is designated as channel data. The frame and channel information can be accessed separately and the data comes out in different files. There is also an option to output a file with the estimated current-voltage (IV) characteristics along with calculated flags for identifying the valid sweep times.

Since the CHUNKS program accesses the standard data base, it must read the same auxiliary files as CHAPS, which contain path information. The CHUNKS default is to read these files from the current directory, but this can be modified by including the path as a command line argument. A command line argument can also be used to switch between batch and GUI mode. Documentation for CHUNKS is available on line in the form of README files.

The files produced by CHUNKS vary in content, dependent on the data and calculations requested. A header section appears listing the column numbers and the corresponding names of the chosen variables. The actual data lines follow, with the variables shown in the order selected. Test runs have been made at various time intervals to validate that CHAPS and CHUNKS output the same information for common cases.

10. DIGITAL ION DRIFT METER (DIDM)

10.1 DIDM-1 DATA ANALYSIS SUPPORT

The Digital Ion Drift Meter (DIDM) is one of the three experiments on board the Space Test Experiment Platform (STEP) Mission 4 satellite, launched in October 1997. The DIDM instrument is designed to measure ion drift, ion temperature, and ion density in the Earth's ionosphere. It utilizes miniaturized state-of-the-art detector components and on-board digital signal processing. The analog ion drift meters in use today were designed in the 1970's, and have limited dynamic range. These instruments are large, heavy and require significant amounts of power for operation. DIDM is a prototype of the next generation of smaller, more sensitive versions of instruments measuring the continuously changing space environment. DIDM measures ion drift through the use of two particle detectors, which electrostatically focus the incoming ions onto microchannel plates.

10.1.1 DIDM Data Base

The DIDM data base comprises the downlinked DIDM instrument telemetry and the associated STEP 4 satellite information, and was projected to span at least six months of instrument operation. Researchers planned to analyze the returned data to determine the accuracy and efficiency of the instrument for the measurement of ion drift, ultimately resulting in improvements in the design and operation of future instruments. An effective method for the maintenance and access of such a large and growing data base is required for the data to be of any value to the researchers. The constantly changing World Wide Web has been determined to be the ideal medium for the analysis of the DIDM experiment data. However, the web-based data analysis process has to be fast and responsive to the user. In the traditional web-based data base access, all data processing and associated graphics generation is performed on the web server platform, a slow and unresponsive process. Such a method often requires the same data to be retransmitted from the server for minor changes in the data display, and ignores the CPU processing power of the client platform.

The web-based data analysis system planned for the DIDM experiment uses a different approach, one that shares the CPU processing load between the server and client computer platforms. A schematic of this system is shown in Figure 42. The user accesses the DIDM data analysis web pages with a commonly available web browser from a networked computer platform. Web pages using the standard HTML user interface capabilities allow the user to select the DIDM and/or satellite data parameters and time span for study. The request for data is submitted to the web server, and is processed with the use of Common Gateway Interface (CGI) scripts and programs. The specified data are accessed from the data storage by these programs and are transmitted to the client in a machine-independent format. The client's web browser launches a local, platform-specific

data analysis application upon receipt of the data. The data file contents are displayed in the data analysis application executing on the local platform, giving the user immediate response. These data analysis applications are of an object-oriented design, allowing easy porting between different types of computer platforms. Such a web-based data analysis system shifts some of the CPU processing load from the server to the client, requiring data to be transmitted only once, and allowing the user to easily manipulate the data in the display application running on the local platform. In this configuration, the user's computer platform is used as both an input and output device for the data analysis. Due to a failure of the STEP-4 satellite shortly after its launch in October of 1997, only portions of the planned web-based DIDM data analysis system were fully developed.

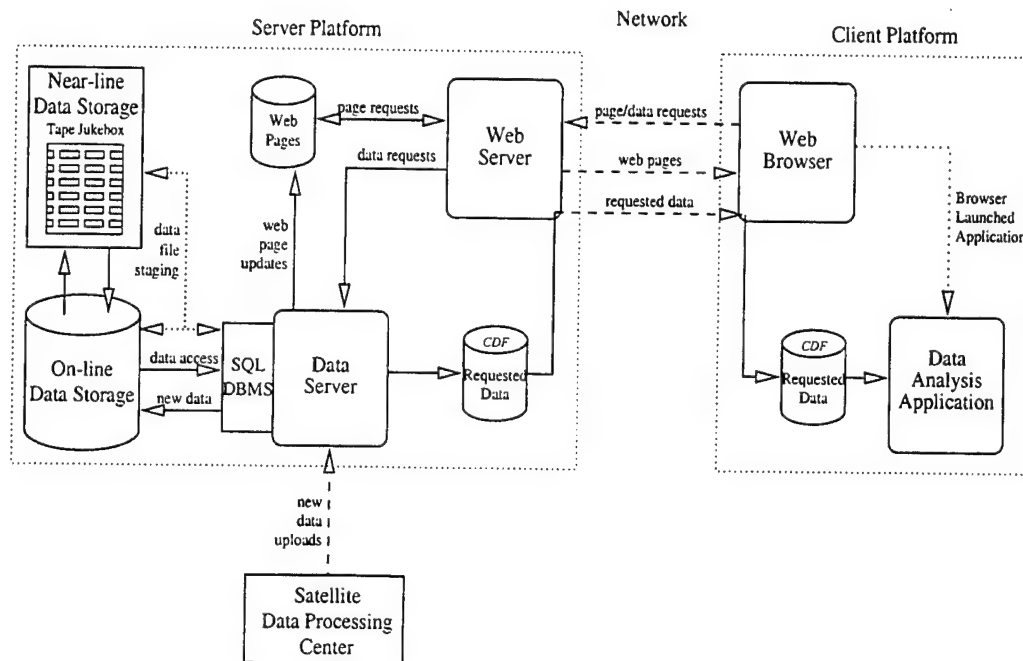


Figure 42. Schematic of DIDM web-based Data Analysis System.

The maintenance and management of the continuously growing DIDM data base can be largely automated through the use of scripts run at specific intervals and an SQL data base system on the web server platform. The RDT&E Support Complex (RSC) for the STEP 4 satellite maintains a file server for posting of new DIDM data files following a satellite contact. A script written in Perl performs periodic ftp sessions to this file server, where new data files are identified and downloaded as they become available. These new data files are to be archived to 8-mm tapes. An initial processing application is run, surveying the contents of the newly downloaded data files, and generating "standard" data product files. These standard data products are specific data calculations which are most commonly requested or give a representative view of the more voluminous raw data. An SQL data base is populated with detailed information about each data file, such as time coverage, data type, file path and archive tape location. Additional scripts update the appropriate web pages to advertise the availability of the new data to the users. During all user

requests for data, the SQL data base is queried to obtain the status and location of the relevant data files. The data file access statistics are also updated. As the amount of on-line data nears the disk capacity, it is planned that the file usage statistics are to be used to determine which data files may be removed from on-line status. These files would still remain accessible from a tape jukebox system containing the archive tapes of all downloaded and processed data files. The use of a multiple tape storage system allows the files to be restored to on-line status autonomously when requested, and also would serve as a method for data base recovery from catastrophic disk drive failure. This self-maintaining data storage system, using disk drives for on-line data storage and a tape jukebox for near-line storage, would eliminate the need of daily data base maintenance by an operator.

The transfer of the DIDM data from the web server to the client's platform in a machine-independent form is accomplished through the use of Common Data Format (CDF) files. The Common Data Format was developed by the National Space Science Data Center (NSSDC) as a method for the storage, management and manipulation of multi-dimensional scientific data sets. The routines in the CDF file interface library are supported on a wide variety of computer platforms, and allow both sequential and random data access. When written in the eXternal Data Representation (XDR) format, CDF files are easily transportable between many different platforms. The CDF files are self-describing, and are able to contain additional information such as titles, parameter labels and units and comments. This feature allows the files to be used in other CDF-capable applications, such as IDL, a popular data graphing package.

The DIDM data display applications are launched by the user's browser on the client platform, upon receipt of the CDF file containing the requested data parameters. Figure 43 shows the display for raw DIDM telemetry data. Figure 44 shows a display of angle calculations based on DIDM drift angles and simulated STEP-4 ACS system data. These object-oriented data display applications are designed to be easily portable between different computer platforms and simple maintenance. Each application has three major components: the platform-specific CDF file interface routines, the common data manipulation and display routines, and the platform-specific low-level graphics and I/O functions. Subsequent modifications and enhancements of the data display applications for all supported platforms can be accomplished quickly because of the component separation. Currently, only MS-Windows 95 and X-Windows based platforms are supported. Two versions of functions for performing window initializations, GUI creation, and graphics and I/O operations have been developed, maintaining identical routine names and parameter lists.

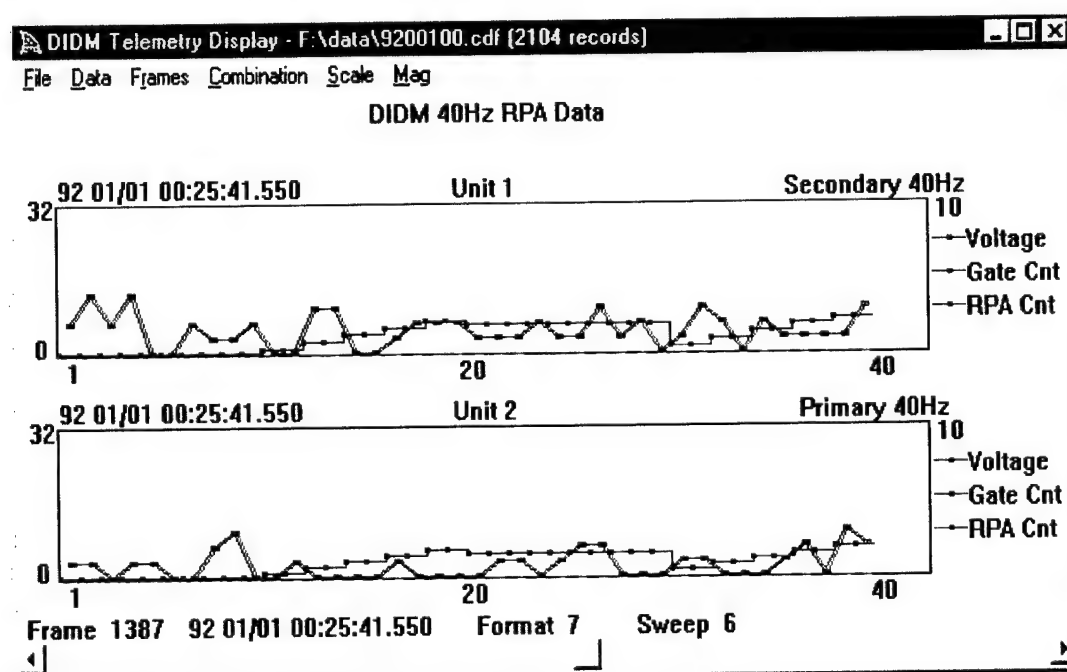
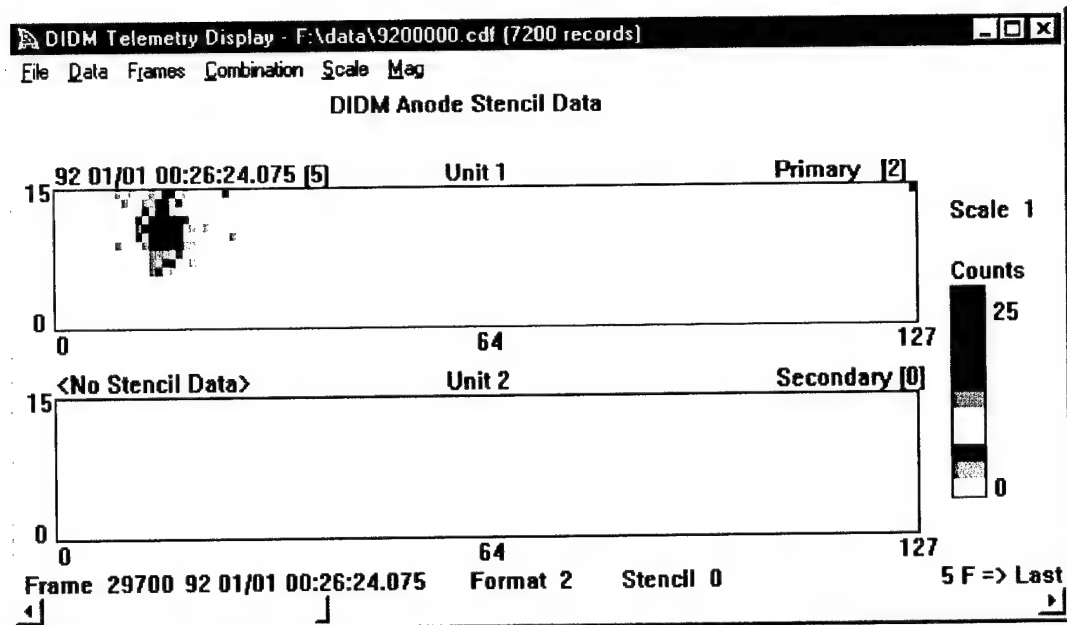


Figure 43. Sample DIDM anode data display.

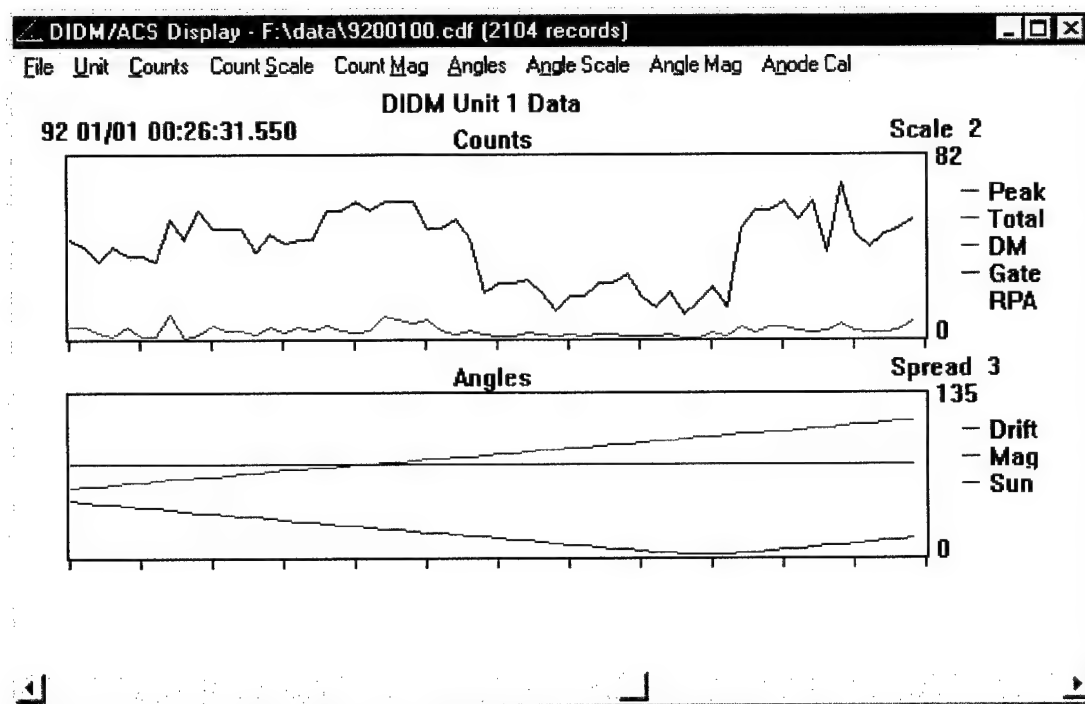


Figure 44. Sample DIDM/STEP4 Angle Data display.

10.2 DIDM-2 ANODE DESIGN SUPPORT

10.2.1 Anode Response Simulator Application

A DIDM anode response simulator application has been developed to be used in support of the design process for the next generation of DIDM anodes. Using a set of DIDM anode characteristics, this application simulates the counting of electrons striking each of the three anode regions, "Wedge", "Strip" and "Z". These counts are used in determining the trajectory of the incident particles detected by the DIDM instrument. Figure 45 shows the DIDM-1 anode design. An algorithm was developed to define the anode region boundaries analytically, where the boundary functions are expressed in terms of percentages of angular width of one anode "cycle". The DIDM-1 anode design contains 120 cycles. The properties of a simulated electron spot are specified by the user, including the spot center azimuth and radius, the spot size and density. The electron spot simulation is performed as a large number of closely spaced position checks, starting at the spot center and slowly working outward in concentric circles about the spot center. Using the analytically defined region boundaries, the region containing the position tested is determined, and the appropriate anode region counter is incremented. The total counts detected in each of the three DIDM anode regions are used to calculate an azimuth and radial position of the electron spot center, using previously defined formulas. Additional anode simulator options

allow the user to specify different values for the number of anode cycles and angular percentages defining the region boundaries. For each simulation the overall impedance of each region is also calculated. The relative impedance values of the three regions are important in determining the overall performance of the anode design.

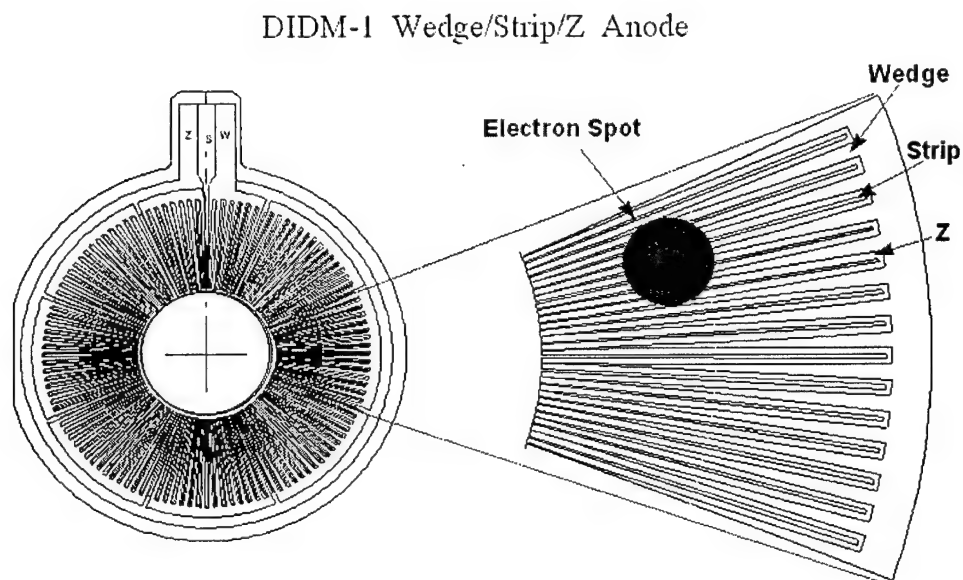


Figure 45. DIDM-1 anode design.

10.2.2 Graphic Design Application

A graphic display application has been developed for use in conjunction with the anode response simulator. This application graphically displays the simulation of the electron spot, where each of the test positions is colored according to the anode region in which it is located. The user specifies the location of the electron spot center, spot radius, and positional check step size. This display application not only validates the methods used in the anode simulator process, but also provides the researcher with a clear visualization. A sample display is shown in Figure 46.

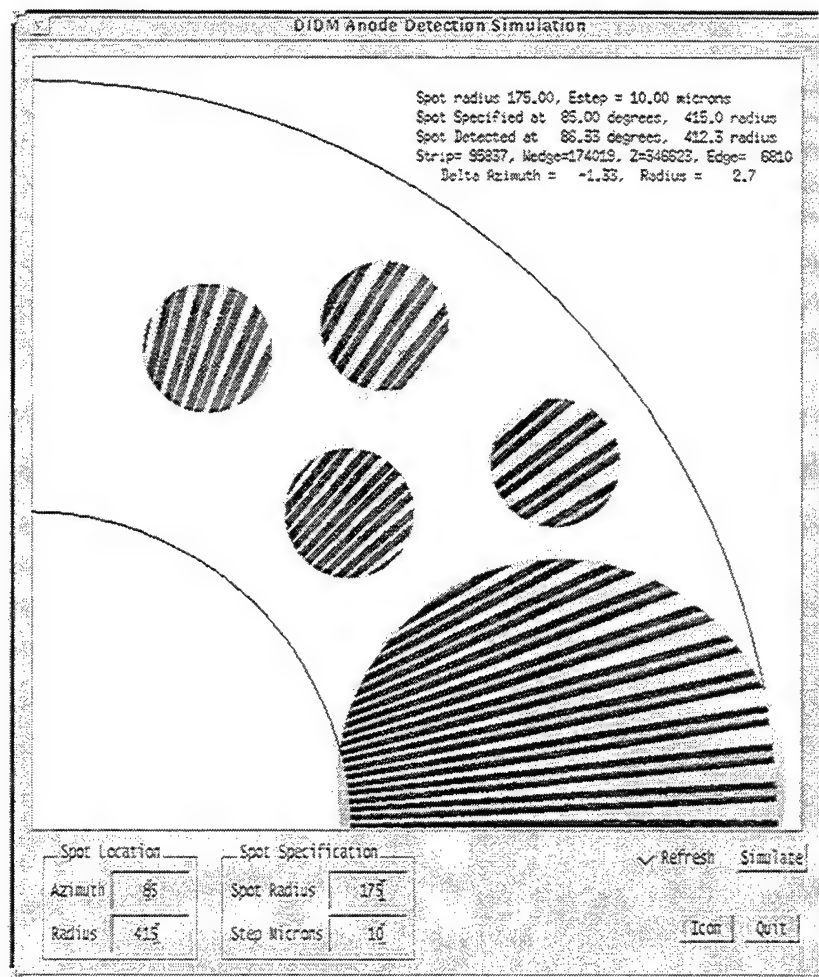


Figure 46. Sample graphic anode simulator display.

Using this anode response simulator, several intensive series of runs have been made, varying the electron spot center position and spot size for several anode design permutations. Plots of the results from these runs have been produced, showing the region detection counts in various reference frames. Samples of such plots are shown in Figure 47. Additional plots have been produced displaying the relative impedance of each of the anode regions for the different anode design permutations. These plots of the anode responses have provided the researcher with valuable information needed to modify the existing anode design for maximizing its performance in future iterations.

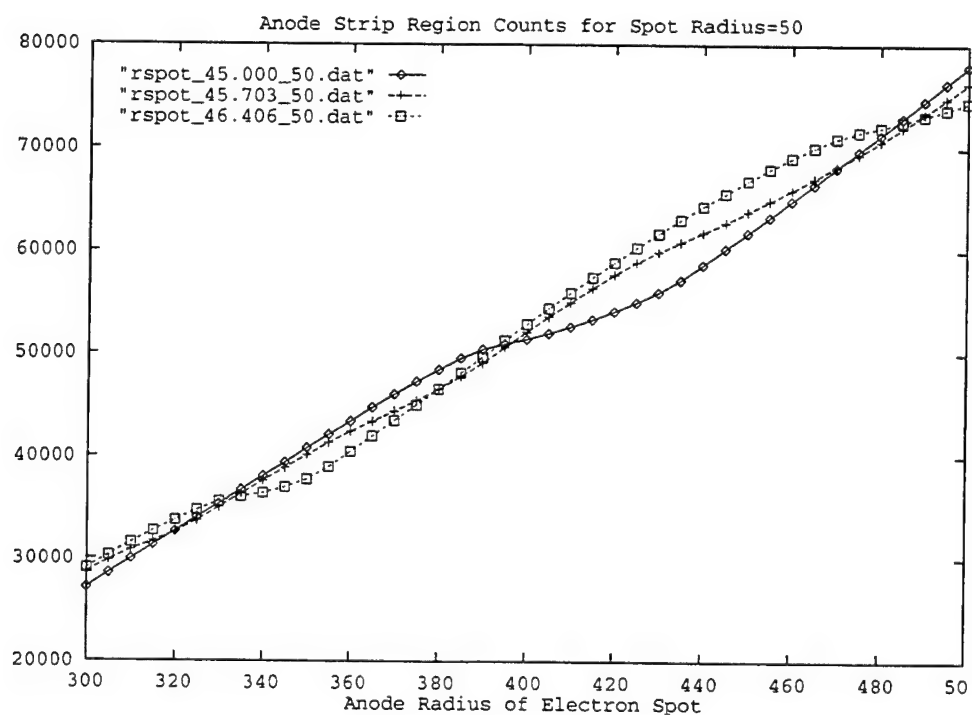
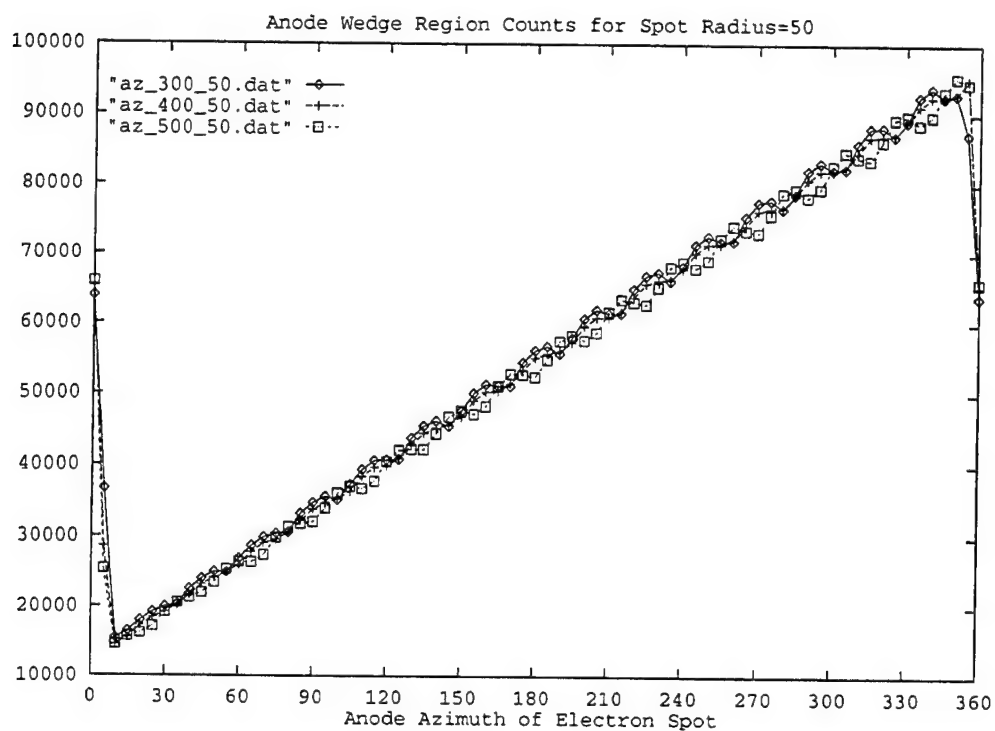


Figure 47. Sample anode simulator response graphs.

11. REFERENCES

- Aarons, J. and S. Basu, "Scintillation on Transionospheric Radio Signals", Handbook of Geophysics and the Space Environment, A. S. Jursa, ed., AFGL/AFSC/USAF, 1985, ADA167000.
- Aikin, A. C. and R. A. Goldberg, Metallic ions in the equatorial ionosphere, *J. Geophys. Res.*, **78**, 734, 1973.
- Anderson, J. G. and C. A. Barth, Rocket investigation of the Mg I and Mg II dayglow, *J. Geophys. Res.*, **76**, 3723, 1971.
- Anderson, R. R., D. A. Gurnett, and D. L. Odem, "CRRES Plasma Wave Experiment", *J. Spacecraft and Rockets*, **29**, No. 4, pp. 570-573, 1992.
- Ayer, S. M., J. N. Bass, K. H. Bhavnani, K. H. Bounar, R. G. Caton, J. M. Griffin, C. A. Hein, M. J. Kendra, A. G. Ling, A. R. Long, W. J. McNeil, D. S. Reynolds, G. P. Seeley, A. A. Setayesh, M. F. Tautz, R. P. Vancour, J. E. Wise, "Integrated Efforts for Analysis of Geophysical Measurements and Models", PL-TR-97-2137, Phillips Lab, Hanscom AFB, MA, 1997, ADA 346154.
- Bass, J. N., K. H. Bhavnani, B-Z-J Guz, R. R. Hayes, P. N. Houle, S. T. Lai, and L. A. Whelan, Analysis and Programming for Research in Physics of the Upper Atmosphere, AFGL-TR-76-0231, Air Force Geophysics Laboratory, Hanscom AFB, MA, 1976, ADA 034066.
- Basu, S. and Su. Basu, "Equatorial Scintillations: Advances Since ISEA-6", AFGL-TR-86-0027, 1985, ADA164801.
- Basu, S., Su. Basu, J. J. Sojka, R. W. Schunk, E. MacKenzie, "Macroscale modeling and Mesoscale observations of plasma density structures in the polar cap", *Geophys. Res. Lett.*, **22**, **8**, p 881-884, April 1995., 1995
- Basu, S., E. Kudeki, Su. Basu, C. E. Valladares, and E. J. Weber, "Scintillations, Plasma Drifts, and Neutral Winds in the Equatorial Ionosphere After Sunset", PL-TR-97-2035, Dec 1996, ADA323542.
- Bell, J. T. and M. S. Gussenhoven, "APEX RAD Documentation", PL-TR-97-2117, Phillips Lab, Hanscom AFB, MA, 1997, ADA 331633.
- Brautigam, D. H., M.S. Gussenhoven, and E.G. Mullen, Quasi-static model of outer zone electrons, *IEEE Trans. Nucl. Sci.*, **39**, 1797, 1992.

- Carter, L. N. and J. M Forbes, Global transport and localized layering of metallic ions in the upper atmosphere, *Ann. Geophysic.*, *submitted*, 1998.
- Chenette, D. L., J. D. Tobin, and S. P. Geller, "CRRES/SPACERAD Heavy Ion Model of the Environment, CHIME", PL-TR-95-2152, Phillips Lab, Hanscom AFB, MA, 1995, ADA 321996.
- Cianciolo, M. E., M. E. Raffensberger, E. O. Schmidt, and J. R. Stearns, "Atmospheric Scene Simulation Modeling and Visualization", PL-TR-96-2079, USAF Phillips Laboratory, Hanscom AFB, MA, 1996, ADA312179.
- Cook, C. U., L. E. Sexton, P. F. Fougère, and N. I. Miller, "APHB Version 4, Defense Meteorological Satellite Program Special Sensor Magnetometer Data Processing Software (SSM Telemetry to Parameters Converter), Volume 1 Software Design User's Guide", AFRL-VS-HA-TR-98-0017, Air Force Research Laboratory, Hanscom AFB, MA, 1998.
- Cornelius, J. R., A. J. Mazzella, J. Andrew, Jr., "User's Guide for the Topside Ionospheric Plasma Monitor (SSIES, SSIES-2, and SSIES-3) on the Spacecraft of the Defense Meteorological Satellite Program (DMSP) Volume II: Programmer's Guide for Software at AF SFC", PL-TR-94-2270, Phillips Lab, Hanscom AFB, MA, 11 Oct, 1994, ADA 290913; "Volume III: Program Maintenance Manual", PL-TR-94-2271, Phillips Lab, Hanscom AFB, MA, 11 Oct, 1994, ADA 290941.
- Daniell, R. E., Jr., L. D. Brown, "PRISM: A Parameterized Real-Time Ionospheric Specification Model, Version 1.5", PL-TR-95-2061, Phillips Lab, Hanscom AFB, MA, 1995, ADA 299664.
- Daniell, R. E. and D. N. Anderson, Realtime operational ionospheric specification and forecast models (WBMOD V.13), paper 95-0549 presented at AIAA Meeting, Reno NV, 1995.
- Falthammar, C.-G., Effects of time-dependent electric fields on geomagnetically trapped radiation, *J. Geophys. Res.*, **70**, P. 2503, 1965.
- Fegley, B., Jr. and A. G. W. Cameron, A vaporization model for iron/silicate fractionation in the Mercury protoplanet, *Earth Planet. Sci. Lett.*, **82**, 207, 1987.
- Gillespie, P., J. M. Rollins, and D. Tofsted, "Evaluation of WAVES using Image Statistics", Proceedings of the 1995 Battlefield Atmospherics Conference, Army Research Laboratory, Battlefield Environment Directorate, White Sands Missile Range, New Mexico, 1995.

- Ginet, G., R. Hilmer, K. Groves, D. Brautigam, K. Kadinsky-Cade, R. Gauthier, T. Hall, E. Holeman, M. Tautz, A. Ling, and G. Law, "AF-GEOSpace User's Manual, Version 1.4 and 1.4P", (1999), To be published as a Technical Report.
- Gussenhoven, M. S., E. G. Mullen, M. D. Violet, C. Hein, J. Bass, J., and D. Madden, CRRES high energy proton flux maps, *IEEE, Trans. Nucl. Sci.*, **40**, 1450-1457, 1993.
- Haerendel, G., "Theory of equatorial spread-F", preprint, Max-Planck-Institut für Extraterr. Phys., Garching bei München, Germany, 1973.
- Hardy, D. A., M. S. Gussenhoven, and E. Holeman, A statistical model of auroral electron precipitation, *J. Geophys. Res.*, **90**, No. A5, 4229-4248, 1985.
- Hardy, D. A., M. S. Gussenhoven, and D. Brautigam, A statistical model of auroral ion precipitation, *J. Geophys. Res.*, **94**, No. A1, 370-392, 1989.
- Hilmer, R. V., and G. H. Voigt, A magnetospheric magnetic field model with flexible current systems driven by independent physical parameters, *J. Geophys. Res.*, **100**, No. A4, 5613-5626, 1995.
- Höffner, J., U. von Zahn, W. J. McNeil and E. Murad, The 1996 Leonid meteor shower as studied with a potassium lidar: Observations and inferred meteoroid sizes, *J. Geophys. Res.*, *submitted*, 1998.
- Holt, B. J., *R and D Equipment Information Report, Volume I of II, SSIES-3 Plasma Monitor System and Related GSE (Serial No. 002 – Flight Unit No. 1)*, University of Texas at Dallas Report UTD-DIR-A04-01-25951, Contract No. F19628-91-C-0033, Line Item 0002, March, 1995.
- Holzworth, R. H., and F. S. Mozer, "Direct evaluation of the radial diffusion coefficient near $L=6$ due to electric field fluctuations", *J. Geophys. Res.*, **84A**, P. 2559, 1979.
- Hoots, F. R., and R. L. Roehrich, "SPACETRACK Report No. 3: Models for Propagation of NORAD Element Sets", Department of Commerce, National Technical Information Service, Springfield, VA, 1980, (also available from FTP site archive.afit.af.mil as /pub/space/spacetrk.doc (SPACETRK)).
- Kelley, M. C., "The Earth's Ionosphere", *Int. Geophys. Ser.*, **43**, p. 71, Academic, San Diego, Calif., 1989.
- Kerns, K. J. and M.S. Gussenhoven, "CRRESRAD Documentation", PL-TR-92-2201, Phillips Lab, Hanscom AFB, MA, 1992, ADA 256673.

- Kopp, E. and U. Herrmann, Ion composition of the lower ionosphere, *Annales Geophysicae*, **2**, 83, 1984.
- Langmuir, I., and H. M. Mott-Smith, "The Theory of Collectors in Gaseous Discharges", *Phys. Rev.*, **28**, P. 4, 1926 (Reprinted in *The Collected Works of Irving Langmuir*, ed. by G. Suits, Pergamon Press, New York, **IV**, p. 99, 1961.
- Love, S. G. and D. E. Brownlee, Heating and thermal transformation of micrometeoroids entering the Earth's atmosphere, *Icarus*, **89**, 26, 1991.
- Love, S. G. and D. E. Brownlee, A direct measurement of the terrestrial mass accretion rate of cosmic dust, *Science*, **262**, 550, 1993.
- Marshak, A., A. Davis, W. Wiscombe, R. Cahalan, "Scale invariance in liquid water distributions in marine stratocumulus, part I: spectral properties and stationarity issues", *Jour. of Atmos. Sci.*, **53**, Number 11, 1996.
- Marshak, A., A. Davis, W. Wiscombe, R. Cahalan, "Scale invariance in liquid water distributions in marine stratocumulus, part II: multifractal properties and intermittency issues", *Jour. of Atmos. Sci.*, **54**, Number 11, 1997.
- McClure, J. P., W. B. Hanson, and J. H. Hoffman, "Plasma bubbles and irregularities in the equatorial ionosphere", *J. Geophys. Res.*, **82**, p 2650, 1977.
- McNeil, W. J., E. Murad and S. T. Lai, Comprehensive modeling of the atmospheric sodium layer, *J. Geophys. Res.*, **100**, 16,847, 1995.
- McNeil, W. J., S. T. Lai and E. Murad, A model for meteoric magnesium in the ionosphere, *J. Geophys. Res.*, **101**, 5251, 1996.
- McNeil, W. J., E. Murad, S. T. Lai, J. A. Gardner, and A. L. Broadfoot, Analysis and modeling of the GLO-1 observations of meteoric metals in the thermosphere, *AGU Fall Meeting*, San Francisco, California, 23-27 December 1997.
- McNeil, W. J., S. T. Lai and E. Murad, Models of thermospheric sodium, calcium and magnesium at the magnetic equator, *Adv. Space Res.*, **21**, 6, 863, 1998a.
- McNeil, W. J., S. T. Lai and E. Murad, Differential ablation of cosmic dust and implications for the relative abundances of atmospheric metals, *J. Geophys. Res.*, **103**, 10,899, 1998b.
- Meffert, J. D. and M. S. Gussenhoven, CRRESPRO Documentation, PL-TR-94-2218, Phillips Lab, Hanscom AFB, MA, 1994, ADA 284578.

- Mullen, E. G., *Private communication*, 1996.
- Olsen, W. P. and K. A. Pfitzer, A qualitative model of the magnetospheric magnetic field, *J. Geophys. Res.*, **79**, 3739, 1974.
- Ossakow, S. L., "Spread F Theories - A Review", Naval Research Laboratory, Washington, DC, NRL-MR-4435, 30 Jan 81, ADA095033.
- Plane, J. M. C. and M. Helmer, Laboratory study of the reactions $\text{Mg} + \text{O}_3$ and $\text{MgO} + \text{O}_3$: Implications for the chemistry of magnesium in the upper atmosphere, *Faraday Discuss.*, **100**, 1234, 1995.
- Press, W. H., F. P. Flanders, S. A. Teukosky, and W. T. Vetterling, *Numerical Recipes: The Art of Scientific Computing*, Cambridge University Press, Cambridge, U. K., 1986.
- Press, W. H., S. A. Teukolsky, W. T. Vetterling, and B. P. Flannery, *Recipes in C, Second Edition*, Cambridge University Press, Cambridge/New York/Melbourne, 1992.
- Qian, J. and C. S. Gardner, Simultaneous lidar measurements of mesospheric Ca, Na and temperature profiles at Urbana, Illinois, *J. Geophys. Res.*, **100**, 7453, 1995.
- Rich, F. J., "User's Guide for the Topside Ionospheric Plasma Monitor (SSIES, SSIES-2, and SSIES-3) on the Spacecraft of the Defense Meteorological Satellite Program (DMSP). Volume I: Technical Description", PL-TR-94-2187, Phillips Lab, Hanscom AFB, MA, 1994, ADA 315731.
- Rino, C. L., "Some Ramifications of the Power-Law Spectral Index for Propagation Modeling", SRI International, Menlo Park, CA, October 1979, ADA085761.
- Scannapieco, A. J., and S. L. Ossakow, "Nonlinear Equatorial Spread F", Naval Research Laboratory, Washington, DC, NRL-MR-3280, May 1976, ADA024440.
- Schulz, M., and Lanzerotti, L. J., *Particle Diffusion in the Radiation Belts*, Springer-Verlag, Berlin/Heidelberg/New York, 1974.
- Secan, J. A. and R. M. Bussey, "An Improved Model of High-Altitude F-Region Scintillation (WBMOD Version 13)", PL-TR-94-2254, Phillips Lab, Hanscom AFB, MA, 1994, ADA 288558.
- Secan, J. A., R. M. Bussey, and E. J. Fremouw, "An improved model of equatorial scintillation", *Radio Sci.*, **30**, p. 607, 1995.

- Singer, H. J., W. P. Sullivan, P. Anderson, F. Mozer, P. Harvey, J. Wygant, and W. McNeil, "Fluxgate magnetometer instrument on the CRRES", *J. Spacecraft and Rockets*, **29**, No. 4, pp. 599-601, 1992.
- Smiddy, M., R. C. Sagalyn, W. P. Sullivan, P. J. L. Wildman, P. Anderson, and F. Rich, "The Topside Ionosphere Plasma Monitor (SSIE) for the Block 5D/Flight 2 DMSP Satellite", Technical Report AFGL-TR-78-0071, Air Force Geophysics Laboratory, Hanscom AFB, MA, 1978, ADA058503.
- Tsyganenko, N. A., A magnetospheric magnetic field model with a warped tail current sheet, *Planet. Space Sci.*, **37**, 5-20, 1989.
- Valladares, C. E., W. B. Hanson, J. P. McClure, and B. L. Cragin, "Bottomside sinusoidal irregularities in the equatorial F-region", *J. Geophys. Res.*, **88**, p. 8025, 1983.
- Wygant, J. R., P. R. Harvey, D. Pankow, N. Maynard, H. Singer, M. Smiddy, W. Sullivan, and P. Anderson, "CRRES electric field/Langmuir probes instrument", *J. Spacecraft and Rockets*, **29**, No. 4, pp. 601-604, 1992.